國立交通大學

物理研究所

博 士 論 文

鹼金屬鹵化物奈米薄膜在共價鍵半導體表面

成長模式和電子結構

Growth Mode and Electronic Structure of Alkali Halide Nano-Films on the Covalent Semiconductor Surfaces

研 究 生：鐘仁陽

指導教授：江進福　教授

林登松　教授

中華民國九十九年八月

鹼金屬鹵化物奈米薄膜在共價鍵半導體表面成長模式和電子結構

Growth Mode and Electronic Structure of Alkali Halide Nano-Films on the Covalent Semiconductor Surfaces

研 究 生：鐘仁陽　　Student：Jen-Yang Chung

指導教授：江進福　　Advisor：Tsin-Fu Jiang

林登松　　Deng-Sung Lin

國 立 交 通 大 學

物 理 研 究 所

博 士 論 文

A Thesis
Submitted to Institute of Physics
College of Science
National Chiao Tung University
in partial Fulfillment of the Requirements
for the Degree of
Doctor
in

Physics

August 2010

Hsinchu, Taiwan, Republic of China

中華民國九十九年八月

鹼金屬鹵化物奈米薄膜在共價鍵半導體表面
成長模式和電子結構

學生：鐘仁陽　　指導教授：江進福　教授
林登松　教授

國立交通大學物理研究所博士班

摘　　要

本論主要研究主題有鹼金屬鹵化物在共價鍵半導體表面和雙原子鹵素分子在半導體表面的吸附。其中，鹼金屬鹵化物包含了氯化鈉和氯化鉀，而雙原子鹵素分子包含了氯化碘和氯化溴氣體。所涵蓋課題包括薄膜成長的機制、原子的結構、電子特性、在介面間電子的轉移。而我們利用分子束磊晶沉積技術和化學氣相沉積技術薄膜。氣體-表面交互作用、吸附原子的擴散以及雙原子分子的化學吸附。實驗方法主要利用變溫掃瞄穿遂顯微術、核心層光電子激發術及第一原理計算。結合此兩種顯微術及光譜學的技術，便可更進一步解析表面的各種反應。

不同表面能量和晶格係數差異的大小都影響了原子結構的排列和成長模式。氯化鈉薄膜和矽(100)-2×1 的晶格係數差異約為 5 %，而核心層光電子激發術的結果說明了，在氯化鈉的覆蓋率小於 40 %時，部分的氯化鈉分子解離而另一部分的氯化鈉分子直接以分子的形式吸附在表面的矽原子上形成了矽－氯－鈉的結構。掃瞄穿遂顯微術的結果顯示，覆蓋率 65 %時，在矽表面上觀察到 c(2×2)、c(2×4)、p(2×2)等的排列結構圖形，而這些不同的結構，主要來自於解離的鈉原子、氯原子、矽原子懸鍵以及矽－氯－鈉的排列。當覆蓋率介於 0.65~2.25 個原子層時，在鈉、氯、氯化鈉所組成的層面上方有著島嶼狀的氯化鈉開始成長，這島嶼狀的氯化鈉是由單位晶格長度 3.82 埃的正方形晶格所組成的，且島嶼狀的氯化鈉高度為 3.8 埃。

氯化鉀薄膜和矽(100)-2×1 的晶格係數差異為 13 %，由核心層光電子激發術的結果說明了，在氯化鉀的覆蓋率小於一個原子層時，部分的氯化鉀分子解離。當覆蓋率超過一個原子層時，靠近費米面的價帶電子態密度有著類似氯化鉀塊材的特徵。掃瞄穿遂顯微術的結果顯示出，覆蓋率等於一個原子層時，表面出現了新穎的 c(4×4)結構

圖形。當覆蓋率大於一個原子層，會出現小部分群集的氯化鉀散落在 c(4×4)的區域介面，並且有著線條般的鏈狀。覆蓋率超過兩個原子層時，氯化鉀是一層接著一層模式成長。結合第一原理的計算，我們可以知道這新穎的 c(4×4)結構圖形是由金字塔幾何結構的原子所組成的。

Growth Mode and Electronic Structure of Alkali Halide Nano-Films on the Covalent Semiconductor Surfaces

Student: Jen-Yang Chung **Advisers: Dr. Tsin-Fu Jiang**

Dr. Deng-Sung Lin

Institute of Physics

National Chiao Tung University

Abstract

This thesis studies the growth mechanism, atomic structure, electronic property, and the charge transfer at the interface between ionic solid films and covalent bonded semiconductor surface for several alkali halides and inter-halogen including NaCl and KCl, ICl, and IBr. Adsorption mechanisms, surface species, chemical reactions, atomic compositions and orderings, and film morphology during the growth using molecular beam epitaxy (MBE) and chemical vapor deposition (CVD) at room temperature were thoroughly investigated. The measurements were carried out by synchrotron radiation core level photoemission and scanning tunneling microscopy. The combination of these complimentary techniques yields much new and detailed information and understanding on the growth mode, film characteristics, and interfacial property for ionic solids on the covalent semiconductor surfaces.

Different surface energies and the dissimilar lattice mismatch lead to the different atomic structures and growth modes. For the smaller lattice mismatch (~5%) of the growth ultra-thin film of NaCl on Si(100)-2×1, the Si 2*p*, Na 2*p*, and Cl 2*p* core level spectra together indicate that adsorbed NaCl molecules at submonolayer coverage ($\theta < 0.4$ ML) are partially dissociated and the rest adsorbed NaCl molecules bonded with Si to form Si-Cl-Na species. The STM results revealed that many dangling bonds are intact and form the c(2×4), c(2×2), and p(2×2) local ordered structures at the coverage of 0.65 ML. A simple model for the dangling bond ordering is presented: The different ordered structures were formed by the different arrangement of the Si-Cl-Na, dissociated Na and Cl, and dangling bonds. At 0.65 <

θ < 2.25 ML, double layer NaCl islands begin to grow on top of the Na, Cl, and NaCl mixed ad-layer. The apparent height of a NaCl double layer island is 3.8 Å and shows well-defined protrusions which are arranged into a square lattice of 3.82 Å.

The growth of KCl on the Si (100)-2×1 has a larger lattice mismatch (~13%). The Si 2*p*, K 3*p*, and Cl 2*p* core level spectra together indicate that adsorbed KCl molecules at submonolayer coverage also partially dissociate and that KCl nano-films above 1. 0 ML have similar features in the valance band density of states with those of the bulk KCl crystal. STM results reveal a novel c(4×4) structure at θ=1 ML. Over 1.0 ML, new clusters randomly disperse around the c(4×4) domain boundaries and often form linear chains. Further KCl deposition above 2 ML follows pseudo layer-by-layer growth. *Ab initio* calculations show that a model that comprises a periodic pyramidal geometry of the novel c(4×4) atomic structure is consistent with experimental results.

To my parents

Acknowledgement

非常感謝我的指導老師林登松教授在這六年來對我的指導和教誨，老師對科學的熱忱、態度，讓我看到身爲一個科學研究學者，真正所應該具備的專業和精神。學生對老師的感謝已經不是三言兩語可言盡，老師真的很謝謝您，辛苦您了。也非常感謝口試委員江進福教授、唐述中教授、潘扶民教授、林炯源教授對於博士論文研究方面的建議和幫助。

感謝凱銘學長、世鑫學長、明峰學長在我對實驗還懵懵懂懂的時候，認真有耐心的教導我，帶我走進這實驗的殿堂，一直到畢業的這一刻，我還是一直覺得有你們這些學長真好。感謝我的同學乾廷、閔光、依亭，跟你們當同窗同學，真的很開心，能夠一起分享生活中的點點滴滴，一起熱烈的討論物理。感謝學妹曉婷，在我熬夜做實驗的時候，會給我黑色的保肝丸。感謝學妹曉穎、欣樺、靈櫻在清大實驗室草創初期，因爲妳們的努力才有現在的實驗室。感謝我的戰友們宏道、中廷，記得在那年、這年夏天我們在同步輻射一起努力奮鬥的日子，有你們的義氣相挺，讓我的實驗能夠順利完成。感謝學妹盈秀在這最後的兩個月內，每天放著美麗的詩歌，抒解我緊張的情緒。感謝學弟展源，當我在低潮時，常常你一句話，打開我心中的那個死結，讓我能夠更有力氣的前進著。感謝學弟國威時常提供我新鮮的話題與趣事。學弟卓穎、鉦祐你們可是實驗室的生力軍喔！加油！加油！

感謝學妹琬珩在我論文的最後階段，常常熬夜幫我分析資料，還有對我的鼓勵和耐心，幫助我渡過這最難熬的階段，接下來新的一年，要好好加油喔，我會支持妳的。

感謝妹妹婉珍和我一起長大，有妳的陪伴，讓我學習如何當一個有責任感的好哥哥，而妳也是一個窩心的好妹妹，常常打電話關心我的近況，找我散散心，我要將這份喜悅跟妳分享。

最後，感激我的父親鐘富泉先生及母親郭淑惠女士，從小對我細心栽培和教導，無怨無悔的付出，讓我能夠健康成長，順利升學。自己一人隻身從澎湖來到台灣念書之後，仍然時時刻刻關心我和掛念著我。因爲有你們的全力支持，才能讓我無後顧之憂，專心做研究，完成博士學業，我要將這本畢業論文獻給我最親愛的父母。

一切榮耀都歸給主

Contents

摘　　要……...……..i

Abstract……iii

Acknowledgement vi

List of Figures x

Chapter 1 Introduction 1

1. 1 Motivation 2

1. 2 The Reconstructed Si(100) Surface 4

1. 3 Literature Review 10

Chapter 2 Experimental Apparatus and Methods 17

2. 1 The Vacuum System 17

2. 2 Scanning Tunneling Microscopy (STM) 20

2. 3 Core Level Photoemission 24

2. 4 Sample Preparation and Temperature Measurement 26

2. 5 The Tip of STM 28

2. 6 The evaporant of KCl and NaCl in EFM 3 31

2. 7 ICl and IBr 35

Chapter 3 Growth mode and novel structure of ultra-thin KCl layers on the Si(100)-2×1 surface 37

3. 1 Introduction 37

3. 2 Experiment Details 39

3. 3 Results and discussion 40

3. 3. 1 Photoemission results 40

3. 3. 2 STM results 45

3. 3. 3 Atomic model of c(4×4) surface structure 51

3. 4 Conclusion 53

Chapter 4 NaCl nanofilms on Si(100) grown by MBE 54

4. 1 Introduction 54

4. 2 Experimental details 56

4. 3 Results and discussion 57

4. 3. 1 Photoemission results 57

4. 3. 2 STM results 59

4. 4 Conclusions 63

Chapter 5 ICl and IBr on Si(100) surfaces 75

5. 1 Introduction 75

5. 2 Experimental details 76

5. 3 Results and discussion 77

5. 3. 1 Photoemission of ICl / Si(100) 77

5. 3. 2 STM images of ICl on Si(100)-2×1 79

5. 3. 3 STM simulation of ICl/Si(100) 81

5. 3. 4 Photoemission of IBr / Si (100) 82

5. 3. 5 STM images of IBr on Si(100)-2×1 84

5. 3. 6 STM simulation of IBr/Si(100) 85

5. 4 Conclusions 86

Chapter 6 Conclusions 100

Appendix A In-situ study of the catalytic oxidation of CO on a Pt(110) surface using ambient pressure X-ray photoelectron spectroscopy 102

A. 1 Introduction 102

A. 2 Experiment Details 104

A. 3 Results and discussion 105

A. 4 Conclusion 111

References……..112

Curriculum vitae 115

List of Figures

Figure 1. 1 (a) Tetrahedral bond arrangement of diamond structure. (b) The down view of diamond structure, the fractions denoted the height of the atoms in units of a cubic edge. 4

Figure 1. 2 The oblique view of the ideal Si(100) surface. Spheres are Si atoms and conoid sticks are dangling bonds. Each silicon atom has two valence bonds and two dangling bonds. 6

Figure 1. 3 (a) The top view and (b) the side view of the ideal Si(100)-1×1 surface. 7

Figure 1. 4 The oblique view of the Si (100)-2×1 first layer surface structure. 7

Figure 1. 5 Top view (a) and side view (b) of the Si(100)-2×1 structure 8

Figure 1. 6 Step structures on Si(100)-2×1 surface. (a) STM image of Si(100)-2×1 surface. The size is 15×10 nm^2 and V_S = 2 V. (b) Oblique, (c) top and (d) side views of step structures. S_A is the steps where the dimer rows direction on the upper terrace parallel the step edge. S_B is the steps where the dimer rows direction on the upper terrace perpendicular the step edge. 9

Figure 1. 7 STM images (a) Large-area STM scan (1130×1130 $Å^2$) of NaCl/Ge (100) (integral coverage about 0.15 DL). Nearly all NaCl islands have a height of one double layer (V_{TIP}=2.7 V, I_T=0.7 nA). (b) STM image (98×81 $Å^2$) with atomic resolution of a NaCl layer of one double layer. The square lattice has a lattice constant of 4.0 Å, and is oriented along the [110] and [-110] directions of the underlying Ge (100) surface (V_{TIP} =2.7 V, I_T=1.8 nA, 1/f filter used)[4]. 11

Figure 1. 8 (a) Close-up (200×200 $Å^2$) of an interesting area of Figure 1. 7(a), and (b) line scan from (a) extracted between the two arrows[4]. 11

Figure 1. 9 (a) An STM image after 0.4 ML LiBr deposition. 50×25 nm^2. V_S = +3.3 V, I_T=0.2 nA. (b) A section profile of the solid line A-A ' in (a). (c) Rigid spheres model of single and double layer growth of LiBr. (d) Top view of LiBr dimer on Si(001) in flat-lying configuration. Thick lines mean chemical bonds between Br and Si atoms[3]. 12

Figure 1. 10 STM images of KI on Si(111) surface. (a) The image (30×30 nm^2) obtained with V_S=3.0 V and I_T=0.08 nA at 0.1 ML of KI. (b) The image (20×20 nm^2) obtained with V_S=3.0 V and I_T=0.15 nA at 0.3 ML of KI[5]. 13

Figure 1. 11 STM images of KI adsorbates on Si(100) surface. (a) The image (25×25 nm^2) was obtained with V_S=2.0 V and I_T=0.15 nA at 0.4 ML of KI. (b) The image (167×167 nm^2) was obtained with V_S=3.5 V and I_T=0.15 nA at 0.8 ML[5]....13

Figure 1. 12 STM patterns of imaging size 20×20 nm^2. (a) The clean Si(100)- 2×1 surface. V_S=-2.2 V, I_T=0.1 nA. (b) The surface with 0.2 ML LiF. V_S=-2.8 V, I_T=0.2 nA. (c) The surface with 0.8 ML LiF. V_S=2.8 V, I_T=0.08 nA[6]. 14

Figure 1. 13 STM constant current topographs of Al(111) after adsorption of 0.35 ML Na and a dose of Cl_2 corresponding to 0.2 ML. (a) 50×50 nm^2, -1.2 V, 0.06 nA. (b) NaCl(111) island with atomic resolution (7×7 nm^2, -1.2 V, 0.3 nA). (c) Structure model of an NaCl(111) island[10]. 15

Figure 1. 14 (a) The Cl ions of a NaCl island (appearing as protrusions, right) are located above the intrinsic steps of the substrate surface (left) as indicated by the dashed line; image size 40×18 Å. (b) Electron bombardment creates single Cl vacancies (circle); size 38×18 Å. (c) A single layer of NaCl shows alternatingly a *c*(2×2) and a *p*(1×1) structure; size 88×27 Å. (d) Defects are observed (dotted lines), which consist of two neighboring Cl ions that appear darker due to a missing Cu atom underneath; size 62×19 Å[11]. 16

Figure 2. 1 The UHV system of VT-STM. 18

Figure 2. 2 The vacuum system for core-level-photoemission spectroscopy. 19

Figure 2. 3 Schematic diagram displays the essential elements of STM.....20

Figure 2. 4 Wave function Ψ(z) for an election with kinetic energy E = U/2 penetrating a potential barrier U. 21

Figure 2. 5 STM images of the Si-Si dimers, imaged with (a) V_s = -2.2 V and (b) V_s = +2.6 V. The filled and empty states of these highly ordered dimmers can be probed by biasing the surface in the opposite directions. The dimensions of the

figure are 2.3 nm × 2.3 nm. 23

Figure 2. 6 Schematic for the energy levels in the core-level photoemission. 25

Figure 2. 7 A chart of the sample current vs. corresponding temperature. 27

Figure 2. 8 The sketch of the etching procedure for the tungsten tip. The tungsten wire is electrochemically etched to produce atomic tips. A tungsten wire is vertically inserted in a solution of NaOH as the anode. A cylindrical stainless steel is also inserted in this solution as the cathode. A positive bias is placed on the tungsten wire. 29

Figure 2. 9 SEM images of tungsten tip. (a) Macrostructure of a 0.5 mm diameter wire after electrochemical etching with DC current. (b) A 0.5 mm diameter wire after electrochemical etching with AC current. 30

Figure 2. 10 Omicron STM tip holder. 30

Figure 2. 11 The evaporator EFM instrument of (a) outside view and (b) mounting a crucible. 33

Figure 2. 12 The dimension of crucibles. 34

Figure 2. 13 experimental setup for the ICl. 36

Figure 3. 1 (a) Si 2*p* and (b) Cl 2*p* core level photoemission spectra (circles) of Cl-Si(100)-2×1 surface and Si(100) surface with various amounts of deposited KCl, as labeled. The solid curves are fits to the spectra. The curves labeled B, S, I and Si^+ are the results of decomposition of the Si 2*p* spectra into contributions from the bulk, the clean surface, the interface layer and the Si-Cl species, respectively. The Cl 2*p* spectra at sub-monolayer coverage have two components Cl_1 and Cl_2. The energy zero in (a) refers to the $2p_{3/2}$ bulk position. To eliminate the band bending effect, the relative binding energy for the Cl 2*p* refers to the corresponding Si $2p_{3/2}$ line of the B component in (a). Dashed lines through the B, S, and Si^+ components are guides for the eye. ...42

Figure 3. 2 Integrated photoemission intensities of Si 2*p*, Cl 2*p* and K 3*p* as functions of KCl coverage. Data for Cl 2*p* and K 3*p* are normalized to the intensity

measured at KCl coverage of 1 ML. Si 2p is normalized to the clean surface before KCl deposition. 43

Figure 3. 3 Valence band region of Si(100) surface with various KCl coverage, as indicated. As in Figure 3. 1(b), the relative binding energy refers to the corresponding Si $2p_{3/2}$ line of the B component in Figure 3. 1(a). Vertical dashed lines are a guide to the eye to show the general trend in the binding energy shifts of K 2*p* and Cl 3*p*. 44

Figure 3. 4 STM images of coverage evolution with deposition of (a) 0.1, (b) 0.3, (c) 0.5, (d) 0.8 and (e) 1.2 ML KCl on Si(100)-2×1 surface. The sample bias was -2.4 V. The images cover an area of about 40×20 nm^2. The white arrows indicate the dimer-row direction in the top silicon layer. (f) Apparent topographic height profile along the green line in (e) from lower-left to upper-right. B: position of one Cluster B. 48

Figure 3. 5 Large-area STM images of coverage evolution with deposition of (a) 0.6, (b) 1.2, (c) 2.4 and (d) 3.6 ML KCl on the Si(100)-2×1 surface. The sample bias was -2.4 V. In (d), two substrate steps (0.14 nm in height) in the lower-left and upper-right corners remain discernible. (e) Schematic showing KCl films (orange) of several layers thick has a bulk-like structure on Si(100). Two atomic steps with heights of 0.315 and 0.14 nm show the interlayer spacings for KCl(100) and Si(100), respectively. (a), (b) and (c) cover an area of 200×100 nm^2 and (d) covers an area of 300×150 nm^2. 49

Figure 3. 6 Apparent topographic height profiles (a) and (b) (from left) along lines marked in Figure 3. 5 c and d, respectively. 50

Figure 3. 7 (a) Close-up image of c(4×4) structure extracted from Figure 3. 5b. Pink dashed rectangle denotes unit cell of ordered Cluster A. Bright protrusions on lower area are Cluster B. (b) Top view, (c) perspective view, and (d) (1,1,0) projection of atomic model of c(4×4) structures. Blue, green and purple circles represent Si, Cl and Na atoms, respectively.....52

Figure 4. 1 (a) Si 2*p*, (b) Cl 2*p*, and (c) Na 2*p* core level photoemission spectra (circles) of

Si (100) surface with various amounts of NaCl deposition, as specified. The solid curves are fits to the spectra. The curves labeled B, S, I and Si^+ are the results of the decomposition of the Si 2*p* spectra into contributions from the bulk, the clean surface, the interface layer and the Si-Cl species, respectively. The energy zero in (a) refers to the $2p_{3/2}$ bulk position. To eliminate the band bending effect, the relative binding energy of the Cl 2*p* and Na 2*p* corresponds to the Si the $2p_{3/2}$ bulk position in (a). Dashed lines through the B, S, and Si^+ components are guides for the eye.....64

Figure 4. 2 (a) Evolution of the components S, S^+, and I intensity of the Si 2*p* photoemission spectra of Figure 4. 1 (a). The intensity of S^+ is normalized to the component of S^+ of the Cl_2 terminated Si(100)-2×1. The intensity of S is normalized to the component of S of the clean Si(100)-2×1 surface. (b) Integrated photoemission intensities of Si 2*p*, Cl 2*p*, and Na 2*p* as functions of NaCl coverage. Data for Cl 2*p* and Na 2*p* are normalized to the intensity measured at NaCl coverage of 1 ML. Si 2*p* is normalized to the clean surface. The dashed and the solid lines are simple guides. 65

Figure 4. 3 (a) STM images of 0.1 ML NaCl on Si (100) with V*s* = -1.8 V. (b) the STM image roomed in from Figure 4.3 (a).....66

Figure 4. 4 Filled-state STM images showing coverage evolution with deposition of (a) 0.65, (b) 0.95, (c) 1.55, and (d) 2.25 ML NaCl on Si(100) surface as labeled. All images are obtained at room temperature with I_T = 0.23 nA and Vs = (a) -2.05, (b) -2.3, (c), and (d) -2.8. The images cover an area of about (a) 80×40 nm^2, and (b)-(d) 300×150 nm^2. Apparent topographic height profiles along the color line are shown in Figure 4. 5. 67

Figure 4. 5 shows the apparent topographic height profiles and corresponding schematic of NaCl films (large yellow rectangles) of one or two layers thick on Si(100) along the arrows in (a) Figure 4. 4 (a), (b) Figure 4. 4 (b), and (c) Figure 4. 4 (c) respectively. The apparent layer thickness of double- layer NaCl films are about 0.38 nm. The NaCl clusters and dissociated species dispersed on the Si(100) surface are represented by concave boxes of the top Si surfaces. 68

Figure 4. 6 (a) 20.0×10.0 nm^2 STM images of Si(100) after 0.6ML NaCl deposited on

Si(100) at sample temperatures of 300 K. Solid boxes enclose selected area with (b) p(2×3), (c) c(2×2), and (d) p(2×2). (e)-(g) Schematic diagram of the area: yellow circles indicated dangling bond, green circles indicated adsorbed Cl, and blue circles with green circles at the center indicated that Na-Cl or Na--Cl. Sample bias voltages used were -2.05 V (a,b,c,d). The distance between two dimer rows is 7.68 Å. The white arrows indicate the dimer row direction. 69

Figure 4. 7 Sphere model of the top view for fig. (b), (c), and (d). The pattern of (a) p(2×4), (b) c(2×2), and (d) p(2×2) correspond Figure 4. 6 (b), (c), and (d) respectively. The smallest (blue), middle (yellow), and largest (green) spheres in the topmost layer are Na, dangling bond, and Cl atoms, respectively. The woods notation is only considered the arrangement of the dangling bonds. ...70

Figure 4. 8 (a) 10×5 nm^2 STM image with atomic resolution on top of an isolated island on the same surface as Figure 4. 4(c). The sample voltage was -2.8V. Atomic structure (b) side view and (c) top view. 72

Figure 4. 9 Filled state STM topography (200×100 nm^2) with different sample bias of the 0.9 ML NaCl deposited on Si(100), I_T = 0.23 nA (a) V_s = -2.3 V and (b) V_s = -2.5 V. (c) Apparent topographic height profiles (from left) along lines marked in (a) and (b), respectively. 73

Figure 4. 10 STM images of NaCl deposited on Si(100) surface. (a) The image (200×100 nm^2) was obtained with I_T = 0.23 nA and V_s = -2.3 V at 0.9ML. (b) The zoomed-in image (80×40 nm^2) is obtained from the solid box enclose selected area in (a). In (b) beside the NaCl islands, the atomic pattern as described in Figure 4. 6 was observed. 74

Figure 5. 1 (a) Si 2*p* and (b) I 4*d* (c) Cl 2*p* core level photoemission spectra (circles) of ICl–Si(100)-2×1 surface and Si(100) surface with various amounts of exposed ICl, as labeled. The solid curves are fits to the spectra. The curves labeled B, S, S', and C are the results of decomposition of the Si 2*p* spectra into contributions from the bulk, the clean surface, and the Si–ICl species,

respectively. The apparent exposure in Langmuir (1 L=10^{-6} Torr • s) is used as the relative measurement of ICl dosage on the bare Si(100)-2×1 surface.....87

Figure 5. 2 Plot of the ratio between Cl 2*p*, Br 3*d*, and I 4*d* core-level peak intensities as a function of ICl and IBr dose. The dada of ICl/Si(111) is from [39], IBr/Si(111) is from [38], and HCl/Si(100) is from [40].....89

Figure 5. 3 The (20×10 nm^2) STM images of Si(100) after saturation dosage of ICl at room temperature. The image is obtained at room temperature with I_T = 0.2 nA and V_S = +2.1 V. The bright spots are I atoms, dim spots are Cl atoms, and darkest spots are defect. The white arrows indicate the dimer-row directions in the top Si layer. 90

Figure 5. 4 (a) Close-up image of c(2×2) structure extracted from Figure 5. 3 dash square denotes unit cell. (b) (-110) projection of atomic model of c(2×2) structure. (c) Top view. Orange, green, and purple circles represent Si, Cl, and I atoms, respectively. According the ab-initio calculation, the bonding lengths of Si-I, Si-Cl are 2.47 Å and 2.07 Å, respectively. The ab-initio radius of I and Cl are 1.27 Å and 0.89 Å. 92

Figure 5. 5 For c(2×2) the empty states of the simulation STM images for the saturation ICl on Si(100) surface above the top ICl overlayer by 1.5 Å with different sample bias at (a) +2.0 V, (b) +2.5 V, and (c) +3.0 V.....93

Figure 5. 6 IBr on Si(100) (a) Si 2*p* and (b) I 4*d* (c) Br 3*d* core level photoemission spectra (circles) of IBr–Si(100)-2×1 surface and Si(100) surface with various amounts of exposed IBr, as labeled. The solid curves are fits to the spectra. The curves labeled B, S, S', and C are the results of decomposition of the Si 2*p* spectra into contributions from the bulk, the clean surface, and the Si–IBr species, respectively. 94

Figure 5. 7 (a) 20.0 × 10.0 nm^2 STM images of Si(100) after saturation dosage of IBr at sample temperatures of 300 K. Solid boxes enclose selected area with (b) p(4×1)-m, p(2×1)-m, (c) c(4×2)-p, c(4×2)-m, and (d) c(2×2)-m. (e)-(g) Schematic diagram of the area: Large yellow circles indicated adsorbed Br, small red circles indicated adsorbed I, and white circles indicated dangling

bonds. Sample bias voltages used were + 2.4 V (a,b,c,d). The distance between two dimer row is 7.68 Å. 96

Figure 5. 8 Sphere model for the Figure 5. 7 (d). (a) Side view. (b)Depiction of mixed Iodide- and Bromide-bonded Si(100)-c(2×2) where pairs of IBr alternate along and across the dimer rows. The rhombus shows the periodic boundary of the primitive cell. According the ab-initio calculation, the bonding lengths of Si-I, Si-Br are 2.47 Å and 2.24 Å, respectively. The ab-initio radius of I and Br are 1.27 Å and 1.06 Å. 97

Figure 5. 9 Sphere model for the Figure 5. 7 (c). (a) Side view. (b)Depiction of mixed Iodide- and Bromide-bonded Si(100)-c(4×2) where pairs of IBr alternate along and across the dimer rows. The rhombus shows the periodic boundary of the primitive cell. 98

Figure 5. 10 For c(2×2) of the empty states of the simulation STM images for the saturation IBr on Si(100) surface above the top IBr overlayer by 1.5 Å with different sample bias at (a) +2.0 V, (b) +2.5 V, and (c) +3.0 V. 99

Figure A. 1 The C1*s*, O1*s* and Pt4*f* core level spectra of the Pt(110) surface under different conditions. A: 200 mTorr CO at room temperature; B: 200 mTorr CO+200 mTorr O_2 at room temperature; C: 200 mTorr CO+200 mTorr O_2 at 100 ℃; D: 200 mTorr CO+200 mTorr O_2 at 150 ℃ 108

Figure A. 2 Partial pressures of CO, O_2, and CO_2 at a constant temperature of 150 ℃. We controlled the CO pressure to switch the reaction from a CO rich to oxygen rich environment and vise versa. Region A: 180 mTorr O_2; Region B: 140 mTorr O_2+230 mTorr CO; Region C: 150 mTorr O_2+14 mTorr -28 mTorr CO; Region D: 140 mTorr O_2+200 mTorr CO. These regions correspond to XPS spectra in Figure A. 3. 109

Figure A. 3 XPS spectra at each region in Figure A. 2 (A-D): (a) C1*s* spectra taken at 540 eV; (b) O1*s* spectra taken at 800 eV; (c) Pt4*f* taken at 340 eV. 110

Chapter 1 Introduction

This dissertation is organized into six chapters. In Chapter 1, the background and motivations of this research and a review of literatures are introduced. Chapter 2 describes the sample preparation procedures and the principles and operations of the experimental apparatus. The following three chapters are presented the three major experiments with detailed results and included two major systems to discuss–ionic crystals/covalent crystal and inter-molecule/semiconductor.

For the ionic/covalent systems, chapter 3 studied heterostructure of ultra-thin KCl films on Si (100)-2 × 1. Chapter 4 studied NaCl on Si(100)-2×1 surfaces. For inter-molecule/semiconductor, in chapter 5 the major study is to understand that the adsorption of prototypical diatomic molecule, ICl (or IBr) gas is excellent framework for the gas-surface reaction of ICl (or IBr) and semiconductor surface.

Finally, in Chapter 6 research results are summarized and the conclusions are made. Appended at the end of this dissertation is the study of the catalytic oxidation of CO on a Pt(110) surface. This research was conducted when the author was supported by Advanced Light Source of Lawrence Berkeley National Laboratory in USA in 2007. The experiments were carried out by the *in-situ* ambient pressure X-ray photoelectron spectroscopy at beam-line 9.3.2 in Advanced Light Source of Lawrence Berkeley National Laboratory and the author was instructed by the beam-line scientists of Zhi Lui and Bongjin Simon Mun in 2007.

1. 1 Motivation

The thin films of insulation material with wide band gap oxides and alkali halide on semiconductor or metal surfaces play an important role in microelectronic devices such as field-effect transistors, tunnel junctions, etc. With the coming miniaturization in these fields, it is not only the lateral extension of a device to be made progress, but also the thickness of insulating layer to be made smaller. As device dimensions are further reduced, the more homogeneous epitaxial system with enhanced insulation properties becomes flat necessary and crucial. The thin films of insulation material also serve well as prototypical systems for research in nano-science and nano-technology. Because the non-vanishing electron density extends through the ultrathin (thickness below 1 nm) insulating films, the scanning tunneling microscopy is a powerful tool like eyes for the investigation of the electric property and heteroepitaxial growth processes of wide-gap materials on metals or semiconductors[1, 2].

Alkali halides, such as NaCl, KI, LiF, LiBr, or CaF_2, are pure ionic materials and are found to grow epitaxially on the Ge(100), Si(100), and Si(111) surfaces using STM and other techniques[3-6]. However, from previous studies that showed no atomic resolution images, we only can obtain a rough idea about their growth morphology. In my proposed research, I plan not only to obtain the growth morphology but also to grow stable and atomically thin insulating films on semiconductor surfaces with an ordered geometric structure. To achieve these goals, I need to undertake and think about what factors affect the growth mechanism.

From the basic surface science textbook, we learn that the relative energy between substrates and film and lattice mismatch are two key factors to generate three different major growth mode, namely, (a) Layer-by-Layer growth (Frank-van der Merve Mode, FM), (b) Layer-plus-Island growth (Stranski-Krastanov Mode, SK), and (c) Island growth (Volmer-Weber Mode, VW). These two factors affect each other. Therefore, in my current research I plan to vary the lattice mismatch systematically in hope to figure out the complete growth modes and mechanism of pure ionic molecule to grow epitaxially on pure covalent crystal.

An STM measurement from Glöckler *et al*. suggests that the growth of NaCl on Ge(100) (mismatch = 0.5%) begins with a carpet-like double-layer NaCl film[4]. For LiBr, LiF and KI on Si (100), the lattice mismatch of ionic crystals/covalent crystal are 1.3%, 29%, and 25% respectively[3, 5, 6]. The STM images showed that well ordered LiBr, LiF and KI films on Si

(100) could not be obtained at 1ML coverage. LiBr, LiF, and KI are adsorbed randomly onto Si(100), and the further growth mode follows the Volmer-Weber mechanism of island growth on Si(100) and Si(111). However, we lack the information of lattice mismatch in the midway between 1 % and 30 %. So, as the first trial, I chose the potassium chloride (KCl) and sodium chloride (NaCl) as the evaporated source. Because the heterostructure of KCl/Si(100) and NaCl/Si(100) have 15% and 5% lattice mismatch respectively, this work could help us to understand the growth mechanism of alkali halide on the group IV semiconductor surfaces.

1. 2 The Reconstructed Si(100) Surface

The Si(100) surface is used to be the substrates for my follows experiment, and its atomic structure of surface introduced as follows. Silicon is a group in IV element with four electrons in its outer orbit and crystallize in the diamond structure with lattice constant a = 5.43 Å, as shown in Fig. 1.5. In a silicon crystal, each silicon atom has four valance bonds bonded to four neighboring silicon atoms in tetrahedral form.

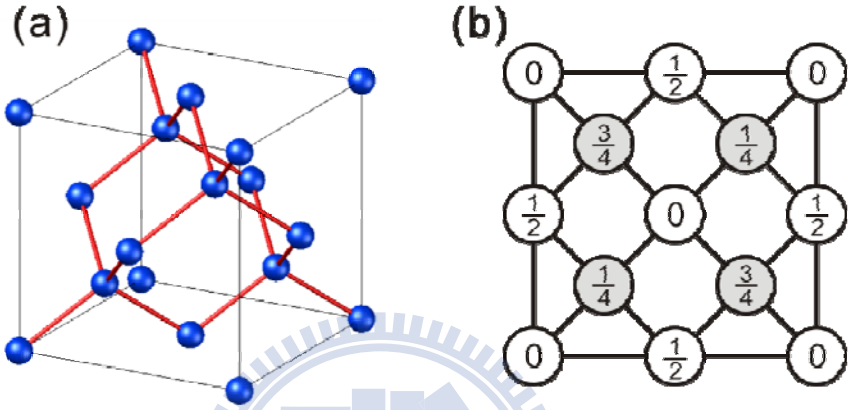

Figure 1. 1 (a) Tetrahedral bond arrangement of diamond structure. (b) The down view of diamond structure, the fractions denoted the height of the atoms in units of a cubic edge.

As the Si crystal is cleaved along a different crystal orientation, the surface of Silicon reconstruct into new different surface atomic structure. For example, if the crystal is cleaved along the (100) direction, the exposure surfaces reconstruct into 2×1 structure to form a Si(100)- 2×1 structure. If the crystal is cleaved along the direction normal (111) direction, the new surface reconstruct into 7×7 structure to be called Si(111)- 7×7 surfaces. In this section, the detail of the Si(100)-2×1 structure is discussed.

If the silicon crystal is cleaved along the (100) direction, two valence bonds of each Si atom on the exposed surface is broken and transform into dangling bonds. Therefore, every silicon atom in the surface has two dangling bonds and two valence bonds, as shown in Fig. 1.6. Figure 1.7 displays the top view of this unreconstructed Si(100) surface with 1×1 structure. In this 1×1 structure, the surface energy is high since the density of the dangling bonds is high (two dangling bonds per atoms), and then the 1×1 structure is unstable. To reduce the numbers of the dangling bonds, the first layer atoms in the surface will reconstruct. By this way, the surface energy will be lower and the surface structure will be more stable.

Upon reconstruction, two neighboring atoms form a strong sigma (σ) bond by combined one of the two dangling bonds. The top-layer atoms of the Si(100) surface dimerize (as two surface atoms binding together to form a dimer) to reduce the number of dangling bonds. These bonded pairs of Si atoms are called dimers. The amount of dangling bonds is reduced by 50 %. This establishes two characteristic directions on the surface, along the dimer row and perpendicular to the dimer. The parallel rows of the dimer bonds also reduce the overall surface energy. These remaining dangling bonds can further form a weak pi (π) bond, as shown in Fig. 1.8. Then the 1×1 structure of the surface have transformed into 2×1 structure, as shown in Fig. 1.9, to be a stable surface.

When preparing the Si(100) surface, the step structure formed by the cleavage along the (100) direction, as shown in Fig. 1.10. The height of the step is about 1.36 Å. The dimer rows on the neighboring terraces are perpendicular, so steps of the terraces divide into two types. S_A is the steps where the dimer rows direction on the upper terrace parallel the step edge. S_B is the steps where the dimer rows direction on the upper terrace perpendicular the step edge.

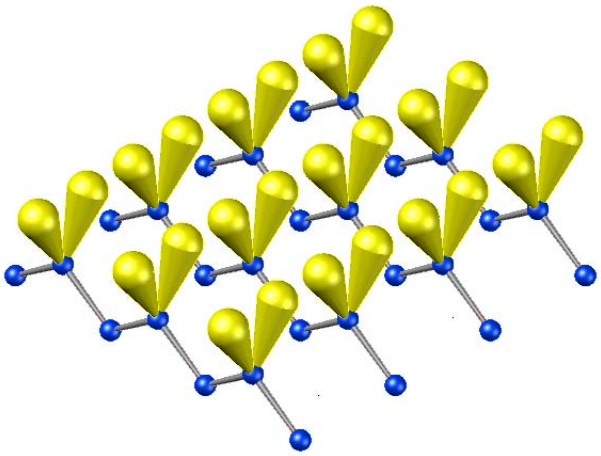

Figure 1. 2 The oblique view of the ideal Si(100) surface. Spheres are Si atoms and conoid sticks are dangling bonds. Each silicon atom has two valence bonds and two dangling bonds.

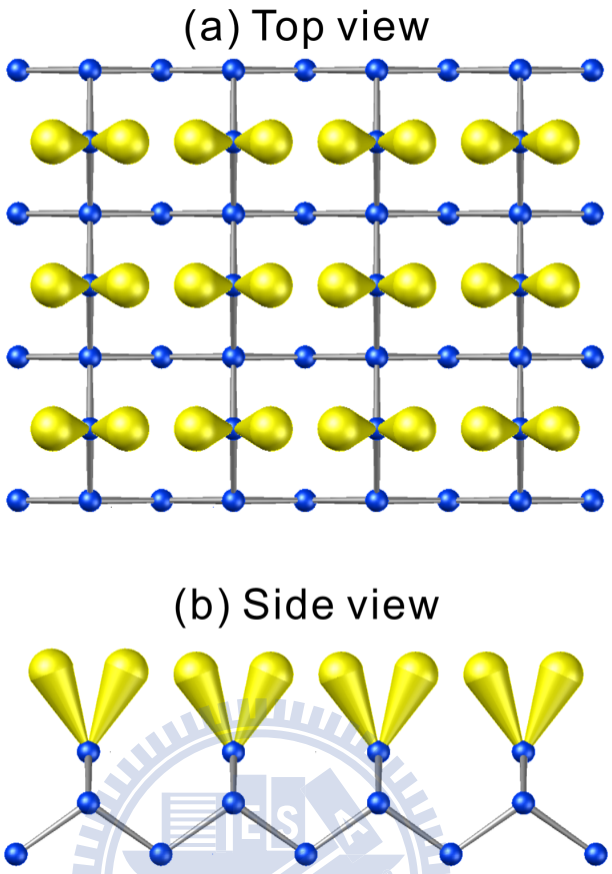

Figure 1. 3 (a) The top view and (b) the side view of the ideal Si(100)-1×1 surface.

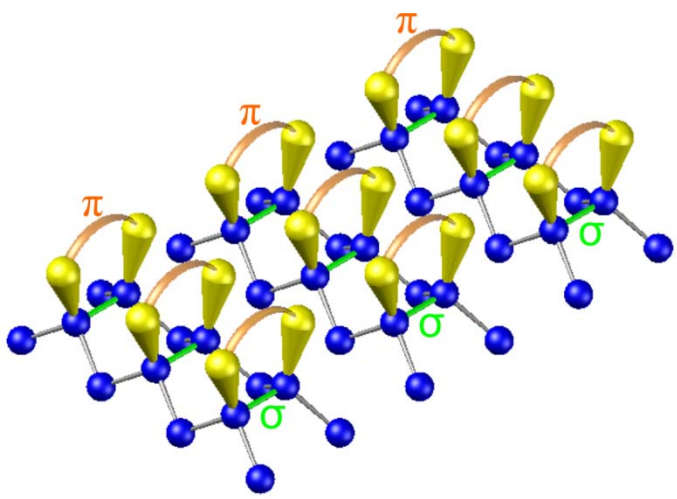

Figure 1. 4 The oblique view of the Si (100)-2×1 first layer surface structure.

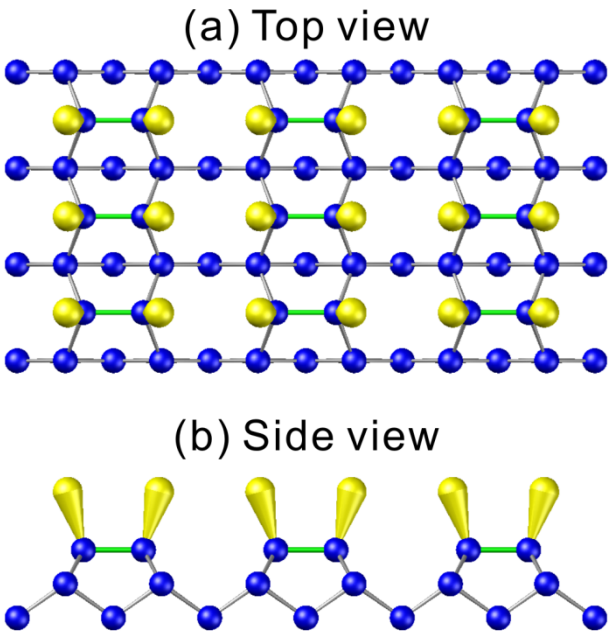

Figure 1. 5 Top view (a) and side view (b) of the Si(100)-2×1 structure .

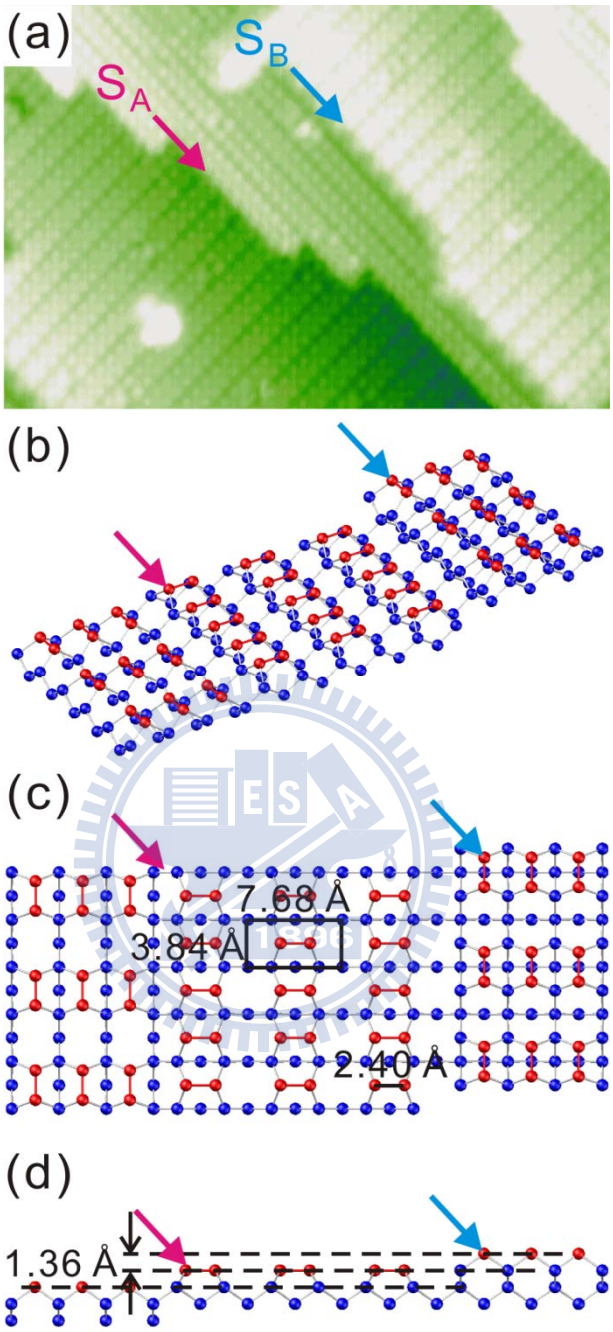

Figure 1. 6 Step structures on Si(100)-2×1 surface. (a) STM image of Si(100)-2×1 surface. The size is 15×10 nm^2 and V*s* = 2 V. (b) Oblique, (c) top and (d) side views of step structures. S_A is the steps where the dimer rows direction on the upper terrace parallel the step edge. S_B is the steps where the dimer rows direction on the upper terrace perpendicular the step edge.

1. 3 Literature Review

Ultrathin well ordered alkali halide layers have been grown successfully and subsequently studied by STM on various substrates, including germanium, aluminium, copper and silver surfaces.

NaCl islands have indeed been successfully grown on numerous crystalline metal surfaces, such as Cu(111), Cu(110), Cu(311), Ag(111), Ag(100), Al(111), and Al(100)[1, 7-10].

STM studies of alkali halide thin films grown on semiconducting substrates have been carried out for the systems; NaCl/Ge(001), LiBr/Si(001), LiF/Si(001), and KI/ Si(001)[3, 4, 6].

In a study on the initial growth of NaCl overlayers on Ge(100), Glöckler *et al* reported STM images for NaCl films up to a thickness of three atomic layers in Figure 1. 7, giving evidence for the earlier proposed carpet-like growthmode of the NaCl layer overmonatomic Ge steps, even for small NaCl islands at submonolayer coverage. The authors report that they were only able to perform STM images by imaging occupied sample states using tip voltages of U=1.5–2.7 V. The authors discuss their observation of lateral atomic resolution for the initial double layer[4].

As UPS data indicate that the band structure of the NaCl double layer, at least for **k** parallel to the surface, is similar to that of the bulk, with the valence band maximum at about 4.2 eV, Glöckler *et al* concluded that the tunnelling current is most likely predominantly due to emission from Ge states through the NaCl layer. They suggest therefore that the lateral contrast, showing protrusions at either the Na^+ or the Cl^- positions, is due to a perturbation and interaction of the Ge wavefunction(s) by the NaCl layer causing a lateral variation of the tunnelling barrier. In Figure 1. 8, the reported apparent heights of the NaCl layers on Ge(001) are positive, but smaller than the corresponding geometric heights (3.8±0.3 Å versus 5.6 Å for the first (double) layer and 2.0±0.3 Å for the second (single) versus 2.8 Å NaCl layer)[4].

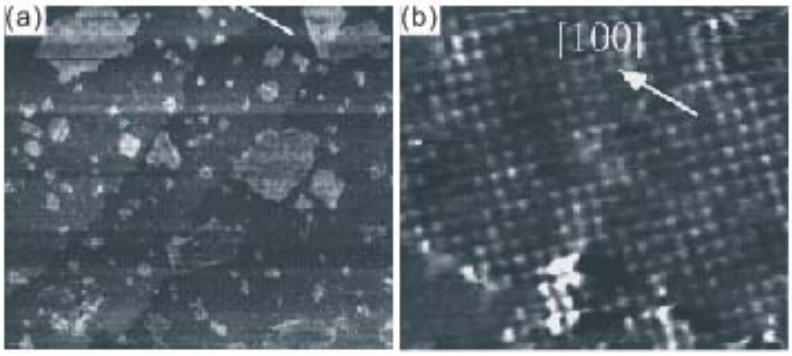

Figure 1. 7 STM images (a) Large-area STM scan (1130×1130 Å^2) of NaCl/Ge (100) (integral coverage about 0.15 DL). Nearly all NaCl islands have a height of one double layer (V_{TIP}=2.7 V, I_T=0.7 nA). (b) STM image (98×81 Å^2) with atomic resolution of a NaCl layer of one double layer. The square lattice has a lattice constant of 4.0 Å, and is oriented along the [110] and [-110] directions of the underlying Ge (100) surface (V_{TIP} =2.7 V, I_T=1.8 nA, 1/f filter used)[4].

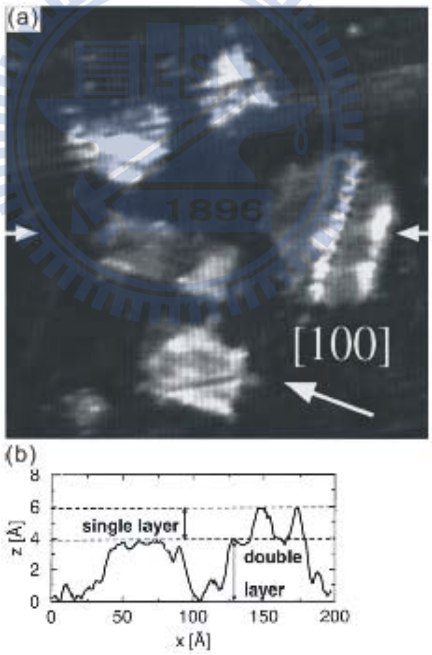

Figure 1. 8 (a) Close-up (200×200 Å^2) of an interesting area of Figure 1. 7(a), and (b) line scan from (a) extracted between the two arrows[4].

LiBr/Si(001) heterostructure has been investigated by scanning tunneling microscopy and spectroscopy (STM and STS). In the initial stage of LiBr growth, rectangular islands are observed consisting of accumulation of about 0.2 nm-thick unit layers. The STM results

indicate that LiBr grows on Si(001) in a single layer fashion. The STS measurement shows a wide band gap region in I-V curve and the energy gap of the LiBr film shows no thickness dependence down to a nominal thickness of 1.2 monolayer (ML)[3].

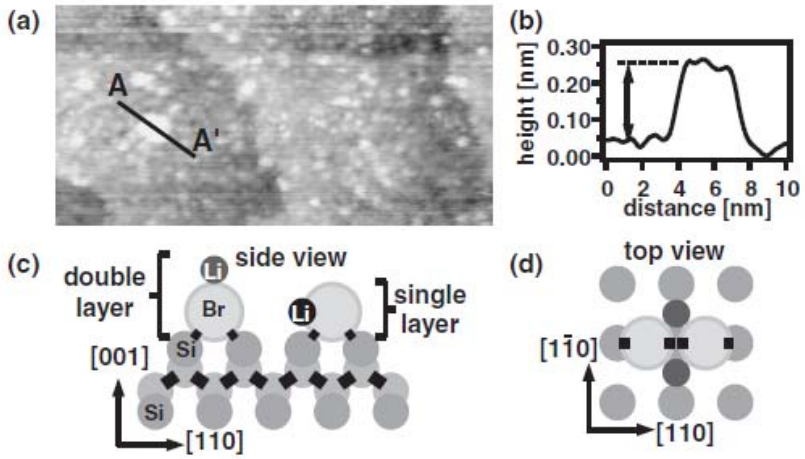

Figure 1. 9 (a) An STM image after 0.4 ML LiBr deposition. 50×25 nm^2. V*s* = +3.3 V, I_T=0.2 nA. (b) A section profile of the solid line A-A ' in (a). (c) Rigid spheres model of single and double layer growth of LiBr. (d) Top view of LiBr dimer on Si(001) in flat-lying configuration. Thick lines mean chemical bonds between Br and Si atoms[3].

The growth of submonolayer KI on Si(111) and Si(100) surfaces at room temperature has been studied with ultrahigh vacuum scanning tunneling microscopy (STM). The STM results show that KI on these surfaces essentially follows island-growth with a reactive interface, and that the morphology of the KI adsorbates at submonolayer coverage critically depends on the atomic structure of the surfaces. On the Si(111) surface, KI initially (coverage below 0.4 monolayer) Tends to coalesce into clusters of size smaller than the 7×7 unit-cell. With further deposition the clusters grow into well-defined islands. On the Si(100) surface, the KI initially shows dissociative adsorption; distinctive islands appear with coverages above 0.4 monolayer, preferentially clustering at the steps and growing into islands with less regularity of size and shape. This comparative study enables us to evaluate the effects of the adsorbate–substrate and adsorbate–adsorbate interactions on the adsorbing behavior and the morphological evolution of the KI/silicon systems[5].

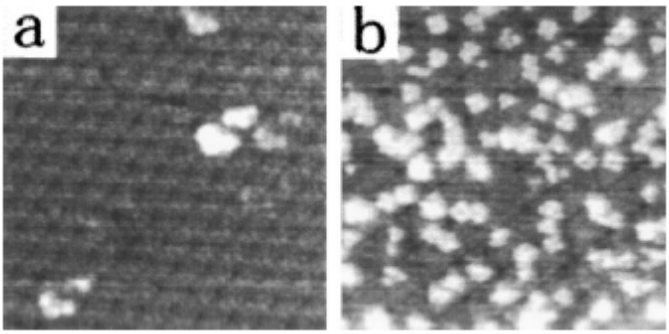

Figure 1. 10 STM images of KI on Si(111) surface. (a) The image (30×30 nm^2) obtained with V_S=3.0 V and I_T=0.08 nA at 0.1 ML of KI. (b) The image (20×20 nm^2) obtained with V_S=3.0 V and I_T=0.15 nA at 0.3 ML of KI[5].

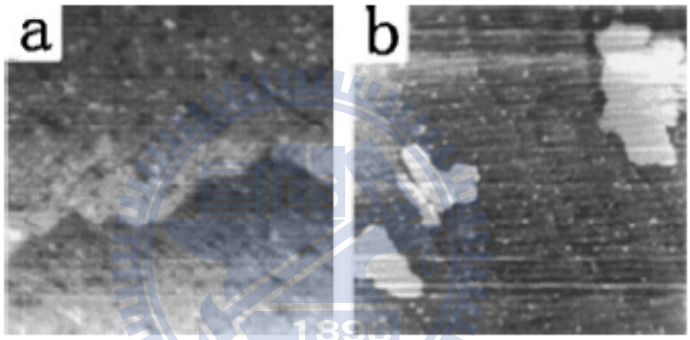

Figure 1. 11 STM images of KI adsorbates on Si(100) surface. (a) The image (25×25 nm^2) was obtained with V_S=2.0 V and I_T=0.15 nA at 0.4 ML of KI. (b) The image (167× 167 nm^2) was obtained with V_S=3.5 V and I_T=0.15 nA at 0.8 ML[5].

The surface morphology of Si(100)- 2×1 with submonolayers of LiF adsorbate and its annealing behavior are studied using scanning tunneling microscopy. LiF adsorbs randomly on the Si(100)-2×1 surface at room temperature (RT), and the 2×1 structure disappears when the coverage of LiF is close to 1 monolayer. Interaction of the Si surface and the LiF adsorbate is enhanced by specimen annealing, which causes dissociation of the LiF and fluorination of the Si surface. Desorption of SiF_x (x=1, 2, 3, 4) results in surface etching. After annealing at 700℃ for 5 min, fluorine on the surface $_x$ decreased below the limit of the detection by X-ray photoelectron spectroscopy, and the Si surface is reconstructed to 2× 1 at about 800℃[6].

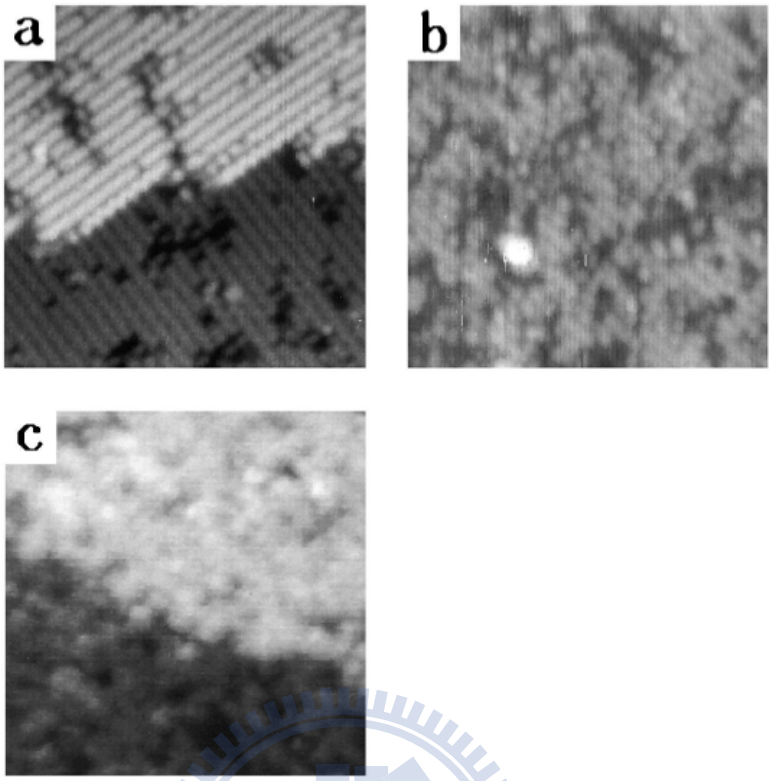

Figure 1. 12 STM patterns of imaging size 20×20 nm^2. (a) The clean Si(100)- 2×1 surface. V_S=-2.2 V, I_T=0.1 nA. (b) The surface with 0.2 ML LiF. V_S=-2.8 V, I_T=0.2 nA. (c) The surface with 0.8 ML LiF. V_S=2.8 V, I_T=0.08 nA[6].

A carpet-like growth mode of NaCl at submonolayer coverage is also found on the aluminium, copper and silver substrates. Atomic resolution images of the NaCl(001) layers on all of these substrates also show a periodicity that corresponds to the positions of one type of ion. The NaCl islands appear for all of these substrates, also with positive apparent height in the STM images. For ultrathin insulating NaCl layers on Al(111) and Al(100), atomic resolution has been obtained at negative sample bias voltages (−0.5 to −3.0 V), imaging the Cl anions as confirmed by spatially resolved *ab initio* calculations of the local density of states. Decreasing NaCl–NaCl step heights were observed with increasing layer thickness and a maximum thickness of three layers for successful imaging was inferred. However, the gap width of the NaCl films has not been investigated. Apart from the energetically favoured (001) orientation of the NaCl layers, Hebenstreit *et al* reported recently on the growth of polar NaCl islands on Al(111)[10].

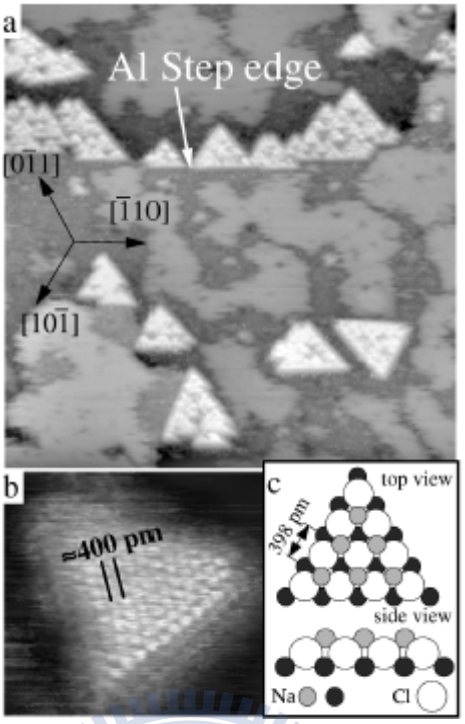

Figure 1. 13 STM constant current topographs of Al(111) after adsorption of 0.35 ML Na and a dose of Cl_2 corresponding to 0.2 ML. (a) 50×50 nm^2, -1.2 V, 0.06 nA. (b) NaCl(111) island with atomic resolution (7×7 nm^2, -1.2 V, 0.3 nA). (c) Structure model of an NaCl(111) island[10].

NaCl on Cu(111) has been studied by Repp *et al*. Similar to the observations on Ge and Al substrates, the islands are imaged with bright contrast in STM images. Atomic resolution images show, even for bias voltages within the band gap of bulk NaCl, the square lattice corresponding to one type of ion of NaCl(001). dI/dU measurements on the NaCl films show a shift of the prior Cu(111) surface state onset towards higher energies upon adsorption of NaCl which is interpreted as an interface state due to NaCl adsorption[11, 12].

In a recent paper, the adsorption properties of NaCl monolayers and bilayers adsorbed on Cu(311) and Cu(100) have been also investigated theoretically by Olsson *et al* using density functional calculations. These investigations include the calculation of adsorption energies and workfunctions for adsorbed NaCl monolayers and bilayers and are compared to the experimental observations of NaCl layers on copper surfaces. For the Cu(311) surface a direct covalent interaction between Cl 3*p* and Cu 3*d* states has been identified.

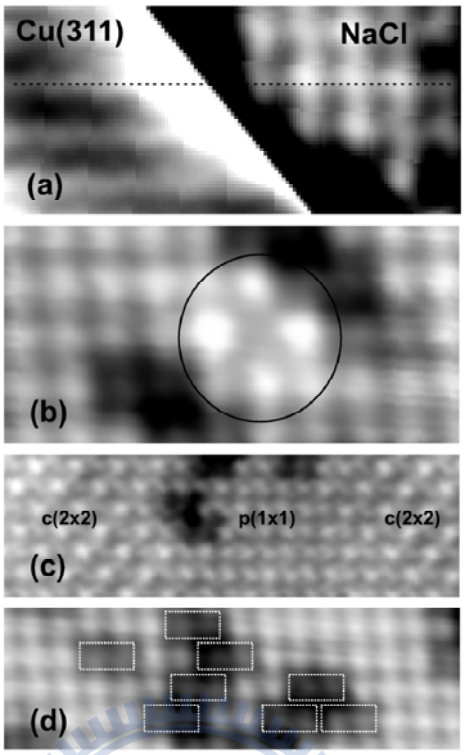

Figure 1. 14 (a) The Cl ions of a NaCl island (appearing as protrusions, right) are located above the intrinsic steps of the substrate surface (left) as indicated by the dashed line; image size 40×18 Å. (b) Electron bombardment creates single Cl vacancies (circle); size 38×18 Å. (c) A single layer of NaCl shows alternatingly a *c*(2×2) and a *p*(1×1) structure; size 88×27 Å. (d) Defects are observed (dotted lines), which consist of two neighboring Cl ions that appear darker due to a missing Cu atom underneath; size 62×19 Å[11].

Chapter 2 Experimental Apparatus and Methods

2. 1 The Vacuum System

The STM experiment was conducted in an ultrahigh-vacuum (UHV) system. The main chamber is equipped with a variable-temperature scanning tunneling microscopy (VT-STM, Omicron), a manipulator, a pumping system, gas sources including H_2, Cl_2 and HCl, as shown in Fig. 2.1. The pumping system is consisting of a dry pump, a turbo pump, a titanium sublimation pump (TSP), and an ion pump. The base pressure of this vacuum system is 1×10^{-10} torr.

The dry pump is used first to lower pressure in the vacuum chamber to ~10^{-3} torr. Then the turbo pump automatically starts to lower the pressure to the 10^{-6} torr range. At this lower pressure, the ion pump turns on. As the pressure drops to ~10^{-7}, we start to bake the chamber at about 120 °C for over 24 hours. After the chamber cools down to RT, we gain the ultra-high vacuum about 1×10^{-10} torr.

The core-level-photoemission experiment is carried out at the National Synchrotron Radiation Research Center (NSRRC) located in the Hsin-chu Science-based Industrial Park, Taiwan. Light from the 1.5-GeV storage ring was dispersed by a Dragon-type 6-m wide range spherical grating monochromator (SGM). This beamline has two energy range, *i.e.* 10-175 eV from a low energy branch and 120-1500 eV from a high energy branch. In our experiment, we use the high energy branch since the main photon energies used are 140, and 240 eV. All the adsorptions of H, Cl and HCl were prepared *in situ* in the ultra-high vacuum system, as shown in Fig. 2.2. In the photoemission experiment, the procedure to obtain the ultra-high vacuum is the same as the STM experiment.

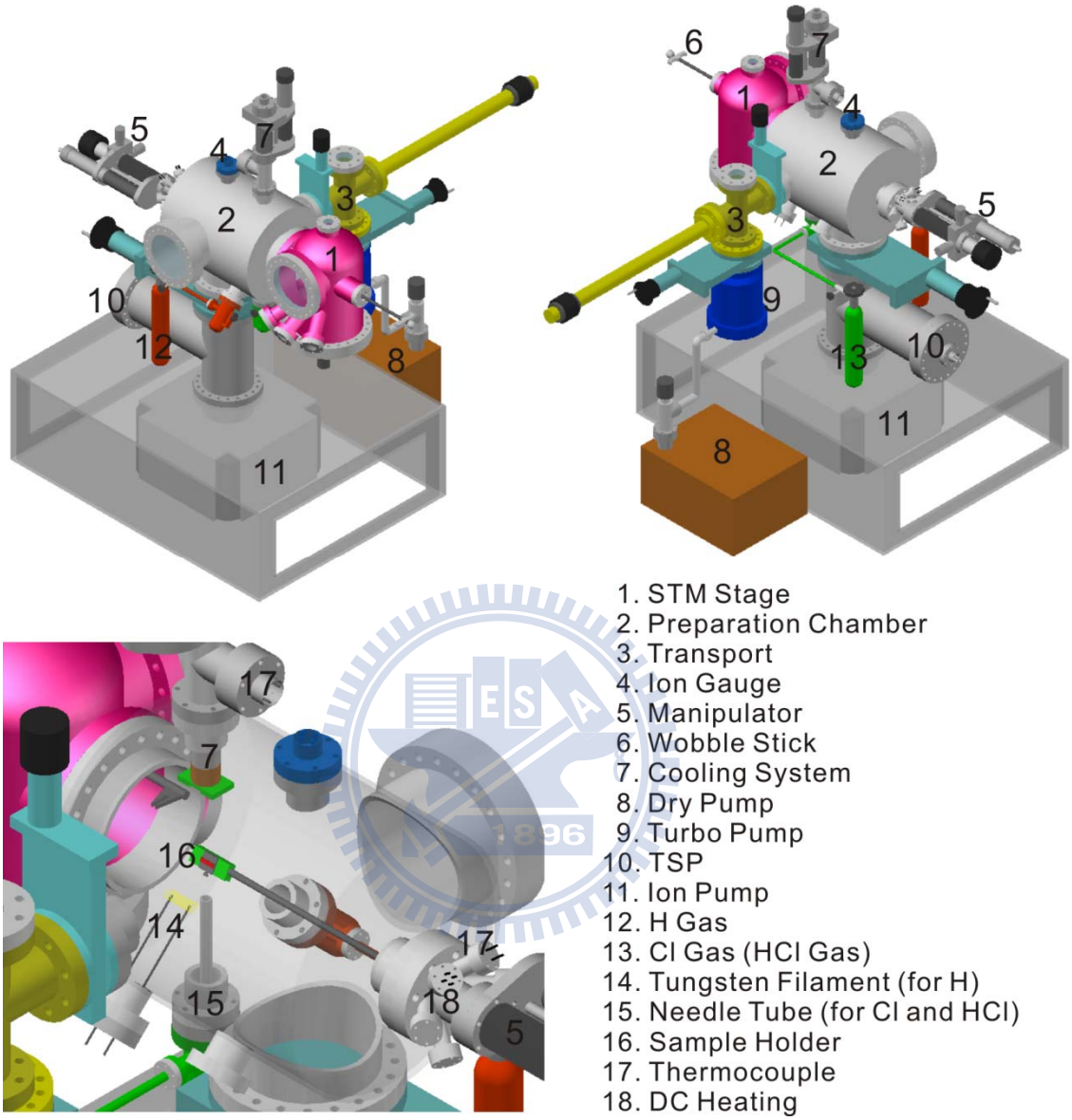

Figure 2. 1 The UHV system of VT-STM.

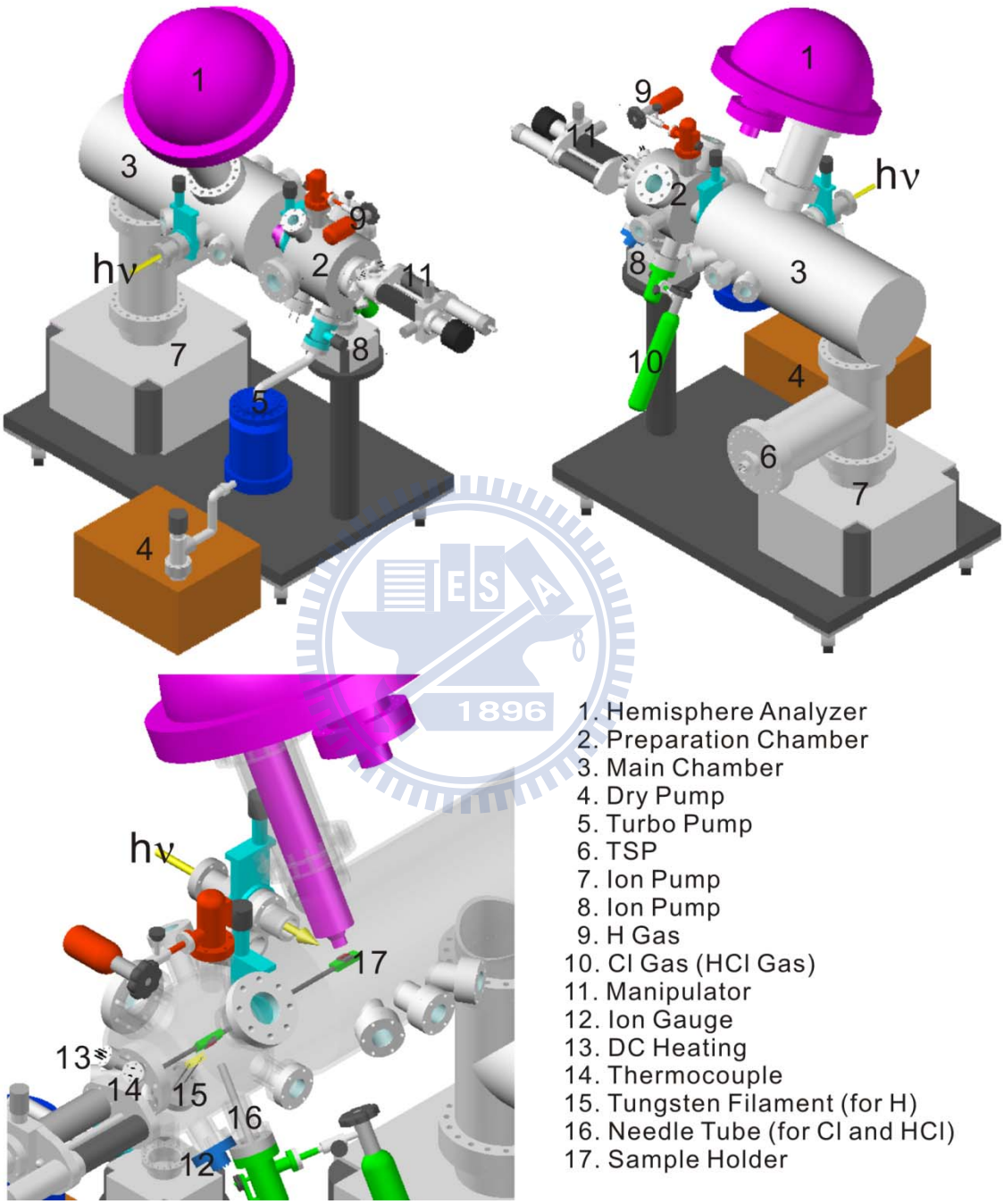

Figure 2. 2 The vacuum system for core-level-photoemission spectroscopy.

2. 2 Scanning Tunneling Microscopy (STM)

Since Binnig *et al.* invented the Scanning Tunneling Microscopy (STM) and obtain the atomic resolution in 1982, the STM technique has been widely used in various fields, like condensed-matter physics, chemical, biology physics and etc. Especially, after resolving the structure of the Si(111)-7×7 in real space using STM , this instrument has proved to be an extremely powerful tool.

Figure 2.3. displays its essential elements. A probe tip, usually made of tungsten (W) or Pt-Ir alloy, is attached to a piezoelectric scanner. Using the coarse positioner and the z piezo, the tip and the sample are brought to within a few angstroms of each other. A bias voltage, applied between the tip and the sample, causes an electrical current to flow. This is a quantum-mechanical phenomenon, tunneling, which is the principle theory of the scanning tunneling microscopy. To achieve atomic resolution, vibration isolation is essential. A commonly used vibration isolation system consists of a set of suspension springs and a damping mechanism.

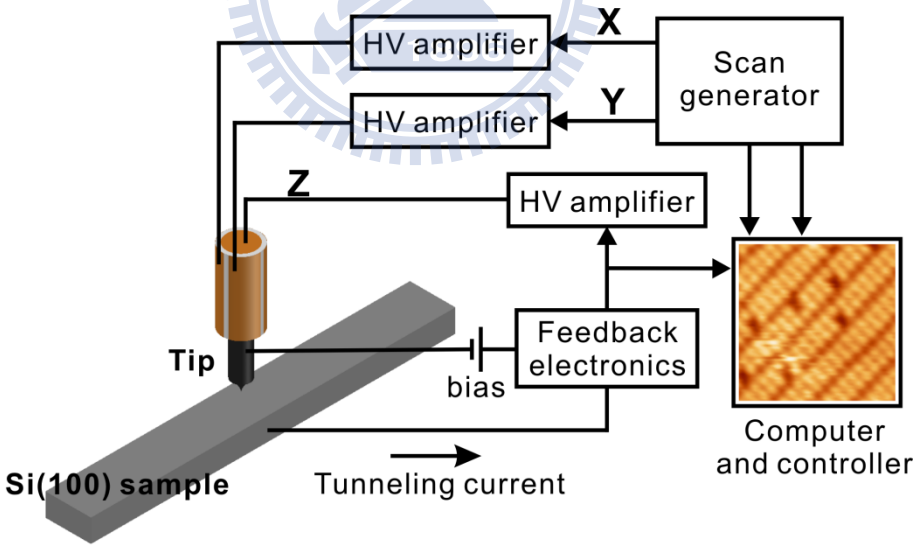

Figure 2. 3 Schematic diagram displays the essential elements of STM

The operating principle of the STM is based on the quantum mechanical phenomenon of tunneling. In this section, we discuss the concept of the tunneling through one-dimensional model. First we consider the classical situation. In the classical mechanics, an electron with energy E moving in a potential U(z) is described by

$$\frac{p_z^{\ 2}}{2m} + U(z) = E \qquad \text{.....(2.1)}$$

In the regions where E > U(z), the electron has a nonzero momentum P_z. It means that the electron has the ability to be in those regions. Otherwise, in the regions where E < U(z), the electron can not penetrate into those regions. In other words, the electron with energy E has no possibility to be find in the regions with U(z) >E. Now we discuss the quantum effect. In the quantum mechanics, the motion of the same electron is described by the Schrödinger's equation,

$$-\frac{h^2}{2m}\frac{d^2}{dz^2}\Psi(z) + U(z)\Psi(z) = E\Psi(z) \qquad \text{.....(2.2)}$$

Ψ(z) is the wavefunction of the electron.

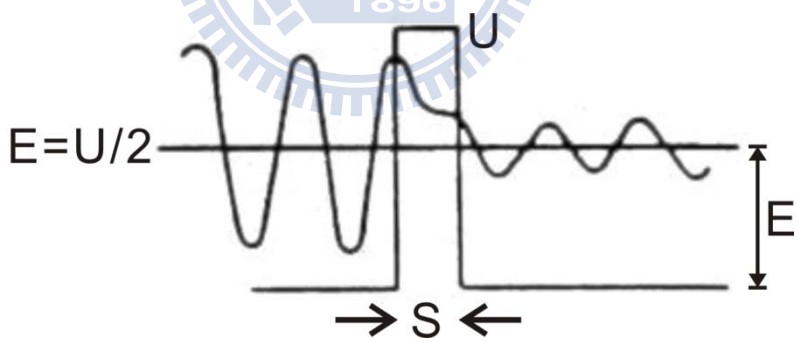

Figure 2. 4 Wave function Ψ(z) for an election with kinetic energy E = U/2 penetrating a potential barrier U.

For a electron with E = U/2 incident on a square barrier from the left, as shown in Fig. 2.4. The Schrödinger's equation of this electron

$$-\frac{\hbar^2}{2m}\frac{d^2}{dz^2}\Psi(z)+\frac{1}{2}U\Psi(z)=0 \qquad \text{.....(2.3)}$$

has the solution:

$$\begin{aligned}\Psi(z) &= Ae^{ikz}+Be^{-ikz} \text{.....}(z<0)\\ \Psi(z) &= Ce^{Kz}+De^{-Kz} \text{.....}(0<z<s)\\ \Psi(z) &= Fe^{ikz} \text{.....}(z>s)\end{aligned} \qquad \text{.....(2.4)}$$

where $k=\frac{(2mU)^{1/2}}{\hbar}$; $K=\frac{(mU)^{1/2}}{\hbar}$

Eq. (2.4) can be solved for the transmission coefficient T = |F/A|2 by matching of the boundary conditions on Ψ and dΨ/dz at x = 0 and x = s. That is

$$T=\frac{1}{1+(\frac{k^2+K^2}{2Kk})^2\sinh^2 Ks} \qquad \text{.....(2.5)}$$

Because a barrier of width s that is much thicker than the wave function decay length of 1/K, K_S >> 1, the transmission coefficient can be approximated as

$$T\approx\frac{16k^2K^2}{(k^2+K^2)}e^{-2ks} \qquad \text{.....(2.6)}$$

It is this exponential dependence of the transmission coefficient T on the barrier width s that enables atomic resolution images in tunneling microscopy. It provides a sufficient signal, the tunneling current, for atomic scale feedback control of the gap width s along the z direction.

Interestingly, use of 1° miscut Si(100) single-crystal wafers allows for highly rotationally oriented samples in which all the Si-Si dimers are pointed in the same direction, yielding anisotropic surfaces on a centimeter length scale. The high ordering of the dimers, showing both the filled and empty states, is shown in the stunning STM images of Fig. 2.5; the filled and empty states were imaged by changing the tip bias.

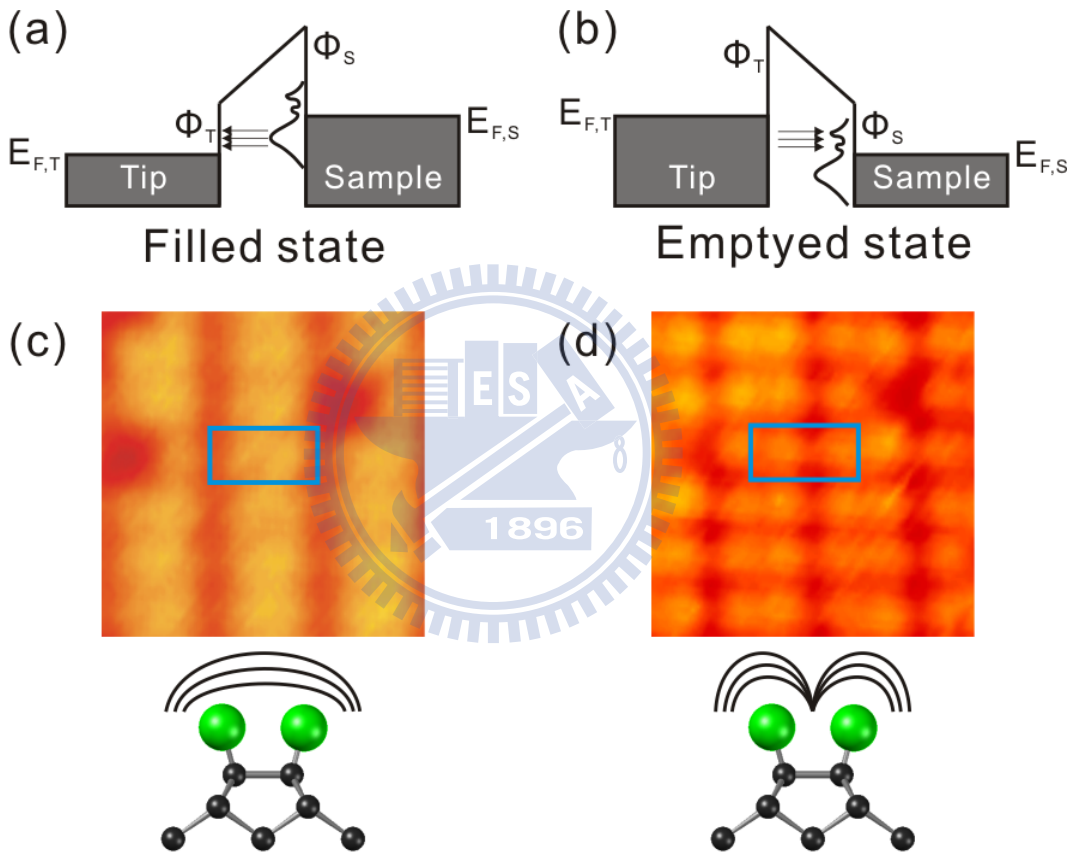

Figure 2. 5 STM images of the Si-Si dimers, imaged with (a) V_s = -2.2 V and (b) V_s = +2.6 V. The filled and empty states of these highly ordered dimmers can be probed by biasing the surface in the opposite directions. The dimensions of the figure are 2.3 nm × 2.3 nm.

2. 3 Core Level Photoemission

The core level photoemission experiment is to collect the photoelectrons excited from core level near nucleus. Photoelectrons were collected and analyzed by a large hemispherical analyzer. By measuring the variation of the photoelectron kinetic energy, we can observe the species of the passivated atoms and chemical bonding etc.

The photoelectrons are excited from inner energy levels (binding energy >20 eV), of which the orbital radius is less than 0.3 Å. In solid state, the core level wave functions are independent such that the binding energies of the atoms in bulk are the same. However, the potential of the atoms near surface becomes different because the local atomic environment changes. The potential difference of surface atoms results in chemical shift of the core level binding energy.

We can explain the relationship between the kinetic energy (KE) of excited photoelectrons and energy of incident photons by the energy conservation law as Eq. 2.7. The relation of the energies is shown in Fig. 2.6.

$$KE = h\nu - B - \Phi \qquad (2.7)$$

KE : kinetic energy of excited photoelectron

$h\nu$: photon energy

B: binding energy

Φ: work function.

In this formula, the binding energy B is the difference between the core level and Fermi level. The work function Φ is the difference between the Fermi level and vacuum level. This formula is based on the ideal situations; however, we have to consider other factors like secondary electrons and escape depth etc. The escape depth of the excited photoelectron is dependent on the kinetic energy, in other word, the higher kinetic energy, the larger escape depth. Therefore, the escape depth of photoelectrons of kinetic energy 20 eV ~ 110 eV is less than 10 Å. The spectra obtained by analyzing these photoelectrons provide us the message of the surface.

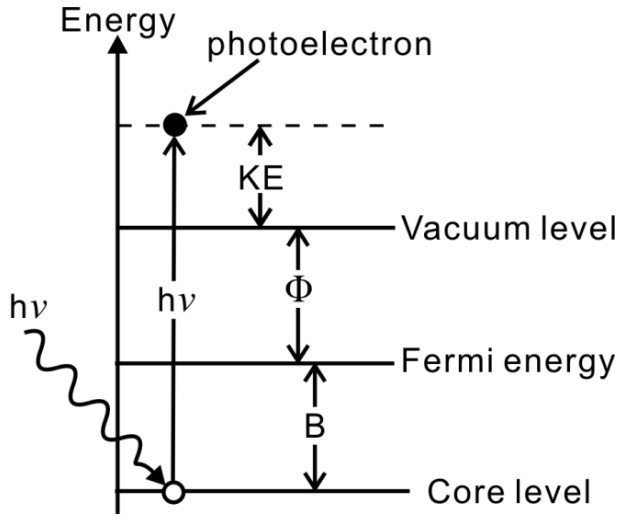

Figure 2. 6 Schematic for the energy levels in the core-level photoemission.

After electrons excited from core level, left holes will be occupied by other electrons. The reaction of occupation can occur in two processes. First, the electrons in the higher energy level occupy the left holes and release the photons of energy equivalent to the difference between two levels. Next, the electrons in the higher energy level occupy the electron holes and release energy. The released energy is not carried by photons but directly excites electrons to leave surface. The excited electrons in the second process are so-called Auger electrons. The Si 2*p* and Ge 3*d* core level photoemission is mainly contributed from Auger electrons.

The lifetime of the electron holes yields Lorentzian broadening. The other factor to result in broadening spectra is the resolution of the analyzer, which produces a Gaussian width of the spectra. The convolution of the Lorentzian width and Gaussian width yields a Voigt lineshape for the spectra.

2. 4 Sample Preparation and Temperature Measurement

Various sample treatments will be conducted depending upon the type of the sample that will be required for the experiment. The Si(100) samples used in our experiment were sliced up into pieces of size 1×8 mm^2 from a antimony (Sb) doped wafers with a dopant concentration of approximately 1.5×10^{15} cm^{-3}. The misalignment of the wafer is about 0.1 degrees. Before loading the samples into the vacuum chamber, we blow off the dust on the surface of the samples with pure nitrogen gas so we don't have unwanted particles on the surface of the samples which could affect our measurements. After loading the samples to the UHV chamber, the samples are then being degassed for over 12 hours at ~900 K using a small AC current. After degassing, the sample was flashed at ~1450 K for a few seconds in order to remove the oxide layer on the surface and form a dimerized clean Si(100)-2×1 surface.

The substrate was heated by passing a controlled dc current directly through the sample. The sample temperature that corresponds to each current was obtained using an infrared optical pyrometer and calibrated by gluing a tiny type-K thermocouple to the center of the sample following the final last STM run, as shown in Fig. 2.7. The uncertainty in the temperature measurement was estimated to be approximately ±5 K.

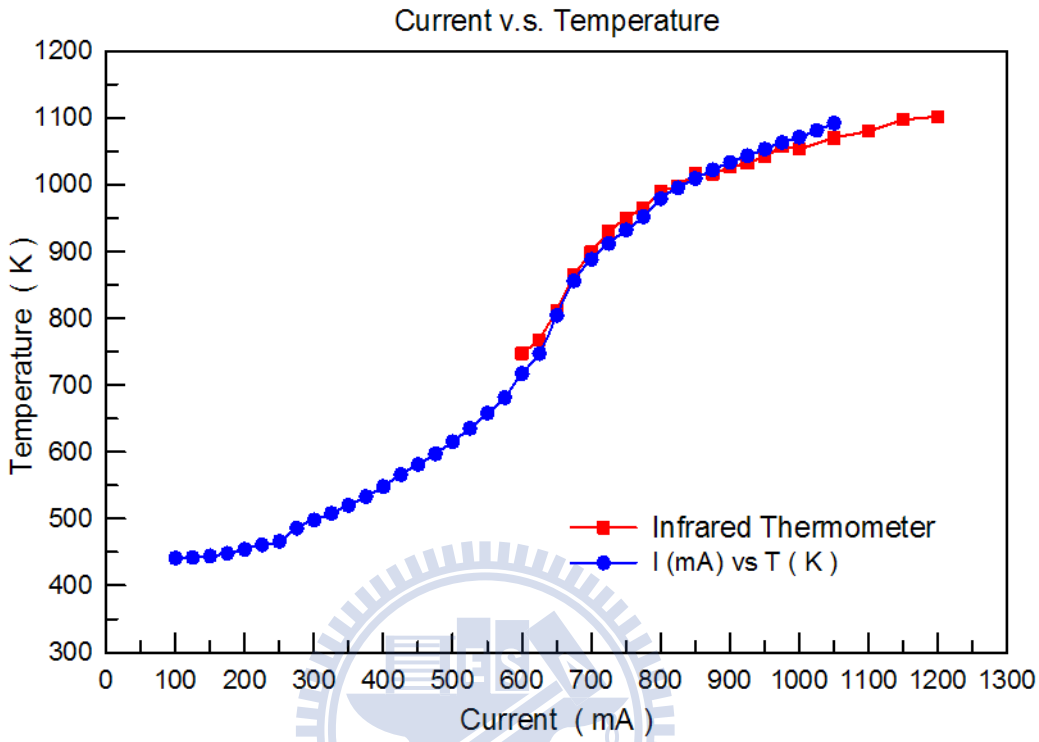

Figure 2. 7 A chart of the sample current vs. corresponding temperature.

2. 5 The Tip of STM

The size, shape and cleanliness of a scanning tunneling microscope (STM) tip are very important for the resolution of a STM. In the UHV system, the W tip is often used. A W tip has to be prepared by electrochemical etching.

For etching we used a tungsten wire as the anode electrode in a special design screw, a circle stainless steel was taken as the cathode, and a 2 M NaOH solution is used as the electrolyte, as shown in Fig.2. The following reactions take place.

$$\begin{array}{rl} \text{Cathode}: & 6H_2O + 4e^- \rightarrow 3H_{2(g)} + 6OH^- \\ \text{Anode}: & W_{(s)} + 8OH^- \rightarrow WO_4^{2-} + 4H_2O + 6e^- \\ \hline \text{Total reaction}: & W_{(s)} + 2OH^- + 2H_2O \rightarrow WO_4^{2-} + 3H_{2(g)} \end{array} \quad \text{.....(2.8)}$$

The tip was cut from straight W (purity is 99.99%) wire of 0.5mm diameter and the 6mm length (Goodfellow Ltd, England) because the diameter of the tip holder is also 0.5mm.

In order to remove the oxide layer of the surface W wires, the wires has to be slightly (about 5 seconds) electropolished over a large part of the wire in the NaOH solution with constant voltage of 15V.

The depth of wire under the surface of NaOH is about 2mm.When the tip start to etch, etching reaction is happened at the interface of the air and the solution. The power supply has constant voltage with an automatic switch-off control. During etching the current through the tip will decrease linearly with time, because the tip below the solution surface decrease and the resistance of the tip (anode) increase. After a long time, the tip forms a neck shape and become thinner and thinner. Eventually the part of the neck is cut down by the weight of the wire under the solution surface dropped down. To remove the residual NaOH solution from the tip surface the tip are then been soaked in de-ioned water for 30 minutes and cleaned by pure methanol. Finally, the tip is set in the tip holder, and backing with 120℃ in the transport chamber at $P=10^{-8}$ torr, after 16 hours the tip is complete.

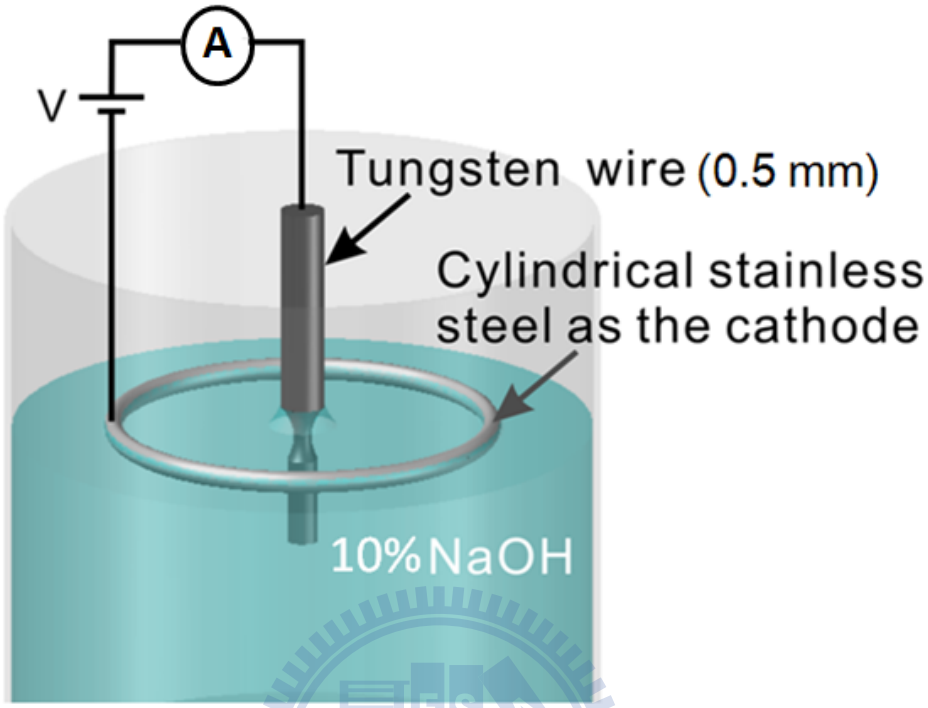

Figure 2. 8 The sketch of the etching procedure for the tungsten tip. The tungsten wire is electrochemically etched to produce atomic tips. A tungsten wire is vertically inserted in a solution of NaOH as the anode. A cylindrical stainless steel is also inserted in this solution as the cathode. A positive bias is placed on the tungsten wire.

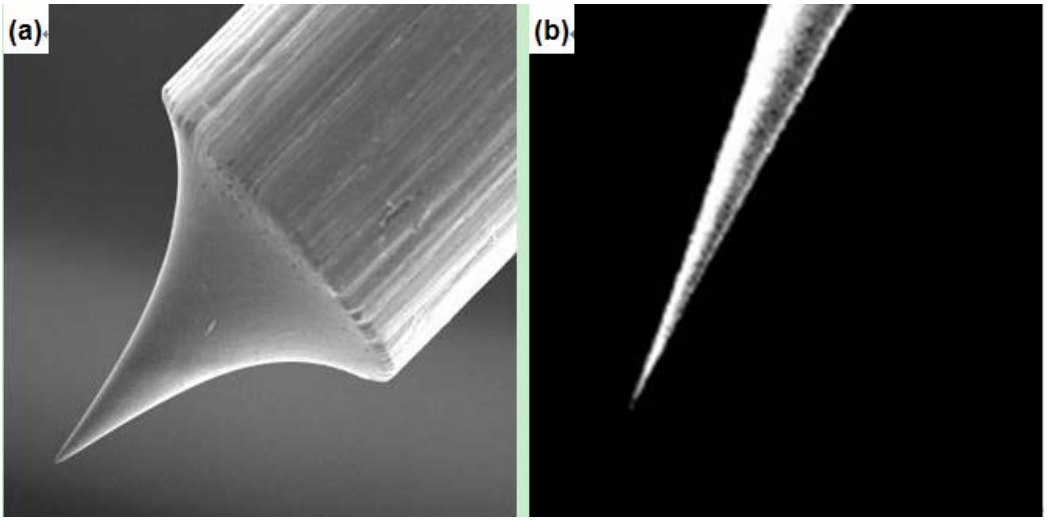

Figure 2. 9 SEM images of tungsten tip. (a) Macrostructure of a 0.5 mm diameter wire after electrochemical etching with DC current. (b) A 0.5 mm diameter wire after electrochemical etching with AC current.

Figure 2. 10 Omicron STM tip holder.

2. 6 The evaporant of KCl and NaCl in EFM 3

In the UHV evaporator EFM3 (Evaporator with integral flux Monitor) is made from Omicron Vakuumphysik GMBH. The NaCl evaporate is evaporated from a crucible which is made of Al_2O_3 (see Fig 2.). This is achieved by electron bombardment heating. The bombarding electron beam induces a temperature rise at the top of the evaporant, causing evaporation.

From appreciate crucibles low melting point, low vapor pressure or reactive material can be evaporated. The appreciate material of crucible can be made of Al_2O_3, pyrolytic boron nitride (pBN), grapite, tantalum, and etc. In my experiment the Al_2O_3 crucible is chosen for setting the NaCl of evaporant. The instrument is designed for high precision sub-mono-layer up to multi-layer deposition of a wide variety of evaporants including highly refractory materials. The fig 2. is the dimensions of Al_2O_3 crucibles.

An important feature of the EFM3 is the integrated flux monitor. In order to obtain the precise rate, once calibrated the flux monitor replaces the necessity of a quartz thickness monitor by continuously monitoring the evaporation rate. Flux is measured directly, which allows a much more precise rate adjustment and much faster rate control than an indirect. The beam exit column contains an ion collector which serves as a flux monitor. At a given electron emission current (IEM) and e-beam voltage the ion flux measured there is directly proportional to the flux of evaporated atoms. The ion flux is displayed on the left indicator of the electronics unit. The flux monitor also operates with the shutter closed thus allowing to preset the evaporation rate.

The EFM3 comes with an shutter at its outlet which can be opened and closed by a rotary drive. This allows precise flux adjustment prior to exposure, and exact control of the evaporation time.

The evaporation cell is contained in a water-cooled copper cylinder (cooling shroud). When NaCl is evaporated, the filament is heating and causing the background pressure increased. So the cooling shroud usefully prevents the background pressure increase too high. But this also depends on the material of evaporant and the pumping speed of the vacuum system.

In my experiment of KCl/Si(100) and NaCl/Si(100), the HV = 800 V, flux = 200 nA ,

I_{EM} = 6 mA, and I_{fil} = 2A, was used. Eventually the molecular bean was giving about 1ML/minute. The ML is referred to the surface density of the unreconstructed Si(100) surface, i.e. 1ML = $6.8\times10^{14}/cm^2$.

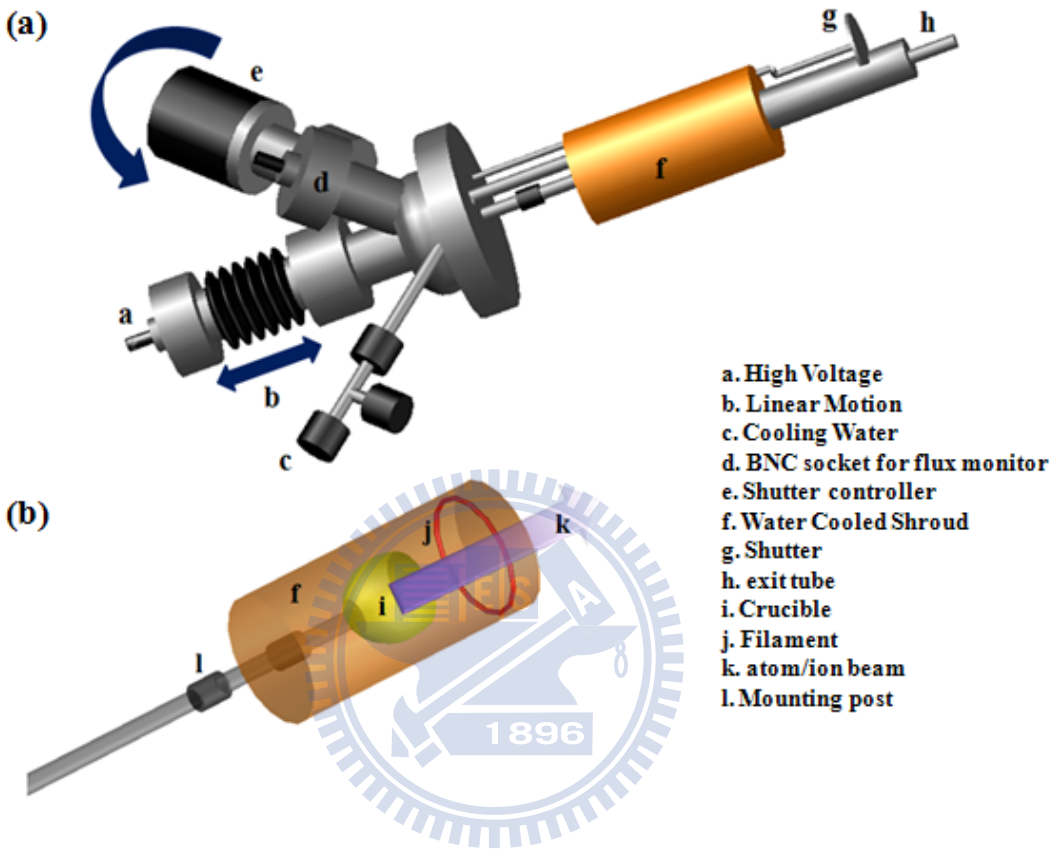

Figure 2. 11 The evaporator EFM instrument of (a) outside view and (b) mounting a crucible.

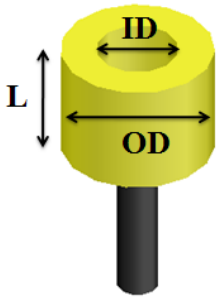

Material Measure	Ta/Mo mm	pBN mm	C mm	Al_2O_3 mm	SSteel mm
ID	4	4.5	5.3	6	5
OD	5 or 8	8	10	10	7
L	6	7	10	14	15
T_{max} (℃)	2000	1600	1400	1400	800

Figure 2. 12 The dimension of crucibles.

2. 7 ICl and IBr

Vapors of ICl were introduced into the vacuum chamber through a precision leak valve and a tube facing the sample while tips were retracted for hundreds of nanometers.

The process of Freeze-Pump-Thaw Degassing for ICl(or IBr)

(1) Place the solution of ICl(99.999%) in a glass tube shown in Figure 2. 13. Make sure the leak valve is closed. Be careful not to use more than 50% of the volume of the glass tube because overfilled the glass tube frequently shatter during this process.

(2) Hook it up to the oil pump and freeze the liquid of ICl. Liquid nitrogen is usually best for this. Before freezing make sure that the environment in the glass tube is free of oxygen to prevent condensing liquid oxygen upon freezing.

(3) When the solution is frozen, only open the valve B to vacuum and pump off the atmosphere for 10-30 minutes.

(4) Close the valve B.

(5) Thaw the solution until it just melts using a tepid water bath. You will see gas bubbles evolve from the solution of ICl. Try not to disturb the liquid. Note: Letting the frozen solution thaw by itself, or using a container of water that melts only the bottom of the frozen solution of ICl may cause the vessel to break.

(6) Replace the water bath with the cooling bath and refreeze the solution of ICl.

(7) Repeat steps (3) – (7) until you no longer see the evolution of gas as the solution thaws. The solution should be put through a minimum of three cycles.

(8) The solution of ICl is ready to use.

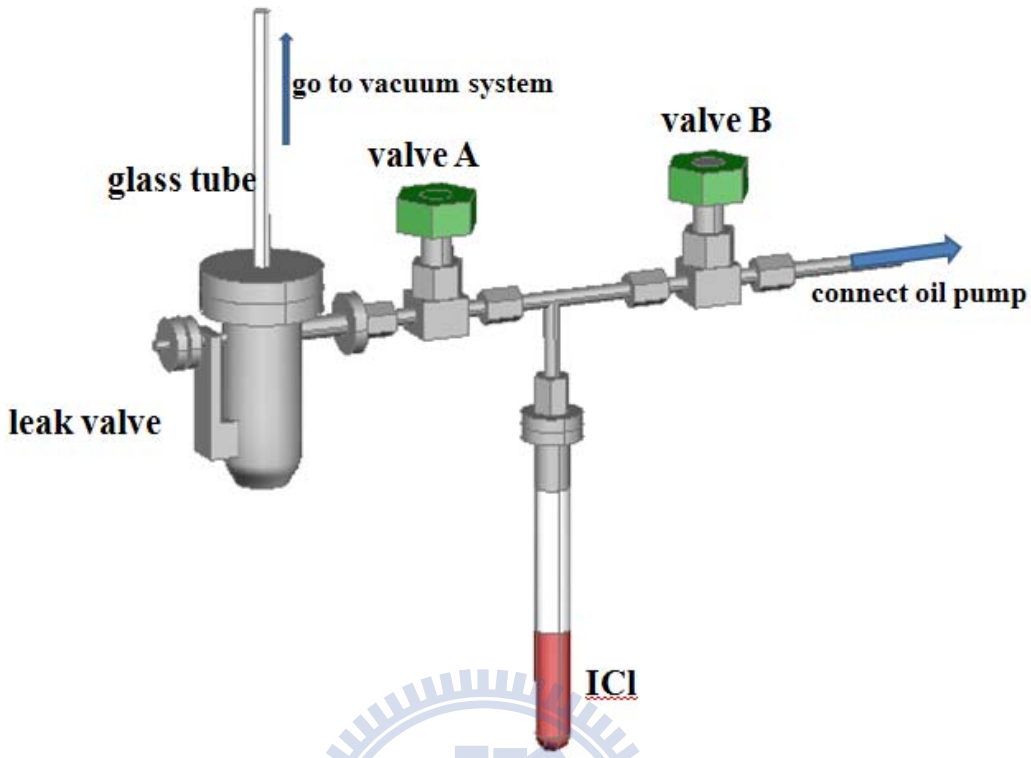

Figure 2. 13 experimental setup for the ICl.

Chapter 3 Growth mode and novel structure of ultra-thin KCl layers on the Si(100)-2×1 surface

This study investigates ultra-thin potassium chloride (KCl) films on the Si(100)-2×1 surfaces at near room temperature. The atomic structure and growth mode of this ionic solid film on the covalent bonded semiconductor surface is examined by synchrotron radiation core level photoemission, scanning tunneling microscopy and *ab initio* calculations. The Si 2*p*, K 3*p* and Cl 2*p* core level spectra together indicate that adsorbed KCl molecules at submonolayer coverage partially dissociate and that KCl overlayers above one monolayer (ML) have similar features in the valance band density of states as those of the bulk KCl crystal. STM results reveal a novel *c*(4×4)structure at 1 ML coverage. *Ab initio* calculations show that a model that comprises a periodic pyramidal geometry is consistent with experimental results.

3. 1 Introduction

Heteroepitaxy is frequently used to develop new synthetic materials-especially semiconductors-for fundamental research and novel devices. Heterostructures that combine very dissimilar materials, such as pure ionic compounds on pure covalent crystals [4, 13], have generated much interest recently owing to the realization of a variety of possible novel properties. Ionic crystals and covalent crystals are held together by attractive forces of very different nature. Understanding the growth mechanism of thin ionic crystals on covalently bonded group IV semiconductors and their interfacial property can broaden our knowledge of principles that govern heteroepitaxy and surface science.

NaCl/Ge(100) is a prototypical system for the heteroepitaxy of small-lattice mismatch ionic crystals/covalent crystal. The second nearest-neighbor separation R_1 for an NaCl crystal is 3.98 Å. The surface lattice constant a, or the period of unreconstructed Ge(100)-1×1, is 4.00 Å. The lattice mismatch at the heterostructure of NaCl/Ge(100) is close to 0.5%. Previous studies have established that NaCl can grow epitaxially on Ge(100) with a high degree of quality under suitable conditions [4, 14-16]. An STM measurement suggests that the growth of NaCl begins with a carpetlike double-layer NaCl film [4]. In an electron energy loss scattering (EELS) measurement Zielasek, Hildebrandt and Henzler found

electronic states at the NaCl/Ge interface and suggested that the dimerization of the Ge(100) surface is not eliminated at the NaCl/interface-even if the thickness of NaCl rises to 20 ML [13].

For large lattice mismatch systems, the growth of alkali halide on the Si and Ge surfaces at around one monolayer coverage does not yield an ordered surface structure. For example, sub-monolayer LiBr (R_1 = 3.89 Å) and LiF (R_2 = 2.85 Å) are adsorbed randomly onto Si(100) (a = 3.84 Å) at room temperature [3, 6]. Guo and Souda observed that KI (nearest–neighbor separation R_0= 3.53 Å) dissociatively adsorbs on the Si(100) surface at a coverage of less than 0.5 ML [5]. Although thick flat films can be obtained, the growth of KI, LiF and LiBr on Si(100) and Si(111) surfaces proceeds by the Volmer-Weber (VW) mechanism of island growth as a result of the interfacial lattice mismatch.

Potassium chloride (KCl) has the sodium chloride structure with R_1= 4.32 Å. The heterostructure of KCl/Si(100) has a very large (13%) lattice mismatch. This study establishes that a single monolayer of KCl forms ordered superstructure on the Si(100) surface and the KCl film can be grown epitaxially. Based on *ab initio* calculations, this study demonstrates that regular arrays of four-facet pyramid-like wrinkles reduce the excess energy associated with a large lattice mismatch. In addition to its uniqueness, this new superstructure also demonstrates the interaction between a pure ionic monolayer and the surface of pure covalent crystals.

3. 2 Experiment Details

The Si(100) samples were antimony doped with a resistance of 0.01 Ω cm. After thorough outgassing at ~900 K, a dimerized clean Si(100) surface was obtained by a few seconds of heating to ~1450 K. 99.99% pure KCl was sublimated from an alumina crucible by a feedback-controlled electron bombardment beam. To minimize contamination at submonolayer coverage, the photoemission was measured immediately after KCl was deposited on clean surfaces. Above one monolayer, the deposition was often performed additively. The deposition rate was determined using an integral flux monitor that was calibrated by a quartz-crystal thickness monitor. The coverage of KCl adsorbate in ML (denoted by h), was estimated from the exposure time, assuming the sticking coefficient is 1. The ML is referred to the surface density of the unreconstructed Si(100) surface, i.e. 1 ML = $6.8\times10^{14}/cm^2$. The substrate temperature during growth was approximately 330 K.

The photoemission spectra were recorded at the Taiwan Light Source laboratory in Hsinchu, Taiwan. Synchrotron radiation from a 1.5 GeV storage ring was dispersed by a wide-range spherical grating monochromator (SGM). The photocurrent from a gold mesh placed in the synchrotron beam path was monitored to determine the relative incident photon beam flux. Photoelectrons were collected from 60° off normal emission and analyzed by a 125 mm hemispherical analyzer in a μ-metal-shielded UHV system with a based pressure of ~3×10^{-10} torr. The overall energy resolution was better than 120 meV. The STM measurement was taken in a separated UHV chamber with a base pressure of 8×10^{-11} torr. The tunneling current was about 0.1 nA. The topographic height measurement did not strongly depend on the sample bias around -2.4 V typically used.

3. 3 Results and discussion

3. 3. 1 Photoemission results

High-resolution core level photoemission spectroscopy can be performed to distinguish between atoms at nonequivalent sites and in different chemical bonding configurations, based on shifts in their binding energy. Identical Voigt line shapes that consist of spin-orbit split doublets individually were used to decompose each of the Si and Cl 2*p* core level spectra into overlapping components [17]. All fitting was performed using the least-squares method. The solid curves represent the fitting results that overlap the data points. Fig. 1a and b present the respective surface-sensitive Si 2*p* and Cl 2*p* core level spectra (dots) of the Si(100) covered with various amounts of KCl. Spectra of the chlorine terminated Si(100)-2×1 (Cl/Si(100)) surface are also presented for reference. The Cl 2*p* spectrum for Cl/Si(100) (Fig. 1b, bottom) can be analyzed in terms of only a single component that has a pair of split doublets separated by 1.60 eV, implying that all Cl has the same Si-Cl monochloride bonding configuration [18, 19]. The corresponding Si 2*p* core level spectrum (Fig. 1a, bottom) has two components, B and Si^+, that are separated by 0.90 eV. The B component was responsible for the emission from the bulk and the Si^+ component from the surface Si-Cl species [20, 21].

Before KCl deposition, the Si 2*p* spectrum (Figure 3. 1a, second from bottom) has a prominent peak S at the lower (-0.52 eV) binding energy side and a visually indiscernible peak S' at the higher (+0.26 eV) binding energy side. These two components are attributed to emissions from the up atoms of asymmetric dimers and atoms in the second layer, respectively [22]. According to Figure 3. 1a and b, the integrated intensities of Cl 2*p* peak (Fig. 2) increase monotonically with the amount of KCl deposited on Si(100) at the expense of that of the Si 2*p* peak. At 5.5 ML coverage, the Si 2*p* peak is mostly attenuated, implying that KCl grows two dimensionally.

At submonolayer coverage of KCl, the intensity of the S component in the Si 2*p* spectra declines during growth. As mentioned earlier, the S component corresponds to the negatively-charged up atoms in the dimerized layer. If the dimerized layer persists under the KCl overlayers as the atomic model suggests in Section 3. 3. 3, the disappearance of the S component suggests a reduced charge transfer between the up- and down-atoms in a

dimer. Tails on the higher binding energy side for Si 2*p* with h = 0.25 and 0.5 ML can be located near the position of the Si^+ component. Also the corresponding Cl 2*p* spectrum appears to consist of two components Cl_1 and Cl_2. These signatures together suggest that a portion of deposited KCl molecules decomposes and Si-Cl bonds are presented on the surface. The KI/Si(100) system exhibited similar decomposition of adsorbed alkali halide. Cl_2 has a larger intensity and its binding energy is close to that of thicker films. It is likelythat Cl_2 is responsible for emission from KCl clusters (as discussed in Section 3. 3. 2). Assuming that Cl_2 corresponds Cl from decomposed KCl, its lower binding energy position may originate from the effect of nearby adsorbed K. The Si 2*p* spectrum for h = 1.0 is broad and can be described by an additional second component (denoted as *I*) on the higher binding energy side of B. The intensity ratio of *I* and *B* (*I*/*B* = 0.49) is about twice that of S and *B* for Si(100). Since S is responsible for 1/2-ML up atoms, the atomic population for *I* is about 1.0 ML. Thus, we believe that component *I* corresponds to emission from the top Si layer under the KCl film.

Figure 3. 3 presents corresponding photoemission spectra in the valence band region of the same Si(100) surface with various KCl coverage. Figure 3. 2 plots the integrated intensities of the K 3*p* peaks, i.e. indicative of surface potassium population. The potassium population similarly increases with the amount of KCl deposited. The peak labeled KCl 3*p* is present above 0.25 ML, indicating that the peak is characteristic of ionic KCl clusters or films. At high coverage, the photoemission spectra are similar to those of thick KCl films [5]. During growth, the valence band emission (Cl 3*p*) from the KCl films slowly dominates while that from the Si(100) substrate is attenuated. According to Figure 3. 3, features of the KCl valence band begin to develop between 0.25 and 0.5 ML. As discussed above, this finding correlates with the decomposition of KCl at low coverage. When h = 1.0 ML, the silicon valence band remains detectable and the valence band offset (ΔE_v) of -4.4 eV is directly determined from the difference between the onsets of Si and KCl valence band photoemission (VBM). Although Si VBM varies only slightly, KCl VBM shifts substantially downwards. ΔE_v gradually decreases to -5.2 eV at 5.5 ML. The trend in the VBM shift resembles that of the LiF/Ge(100) system [23].

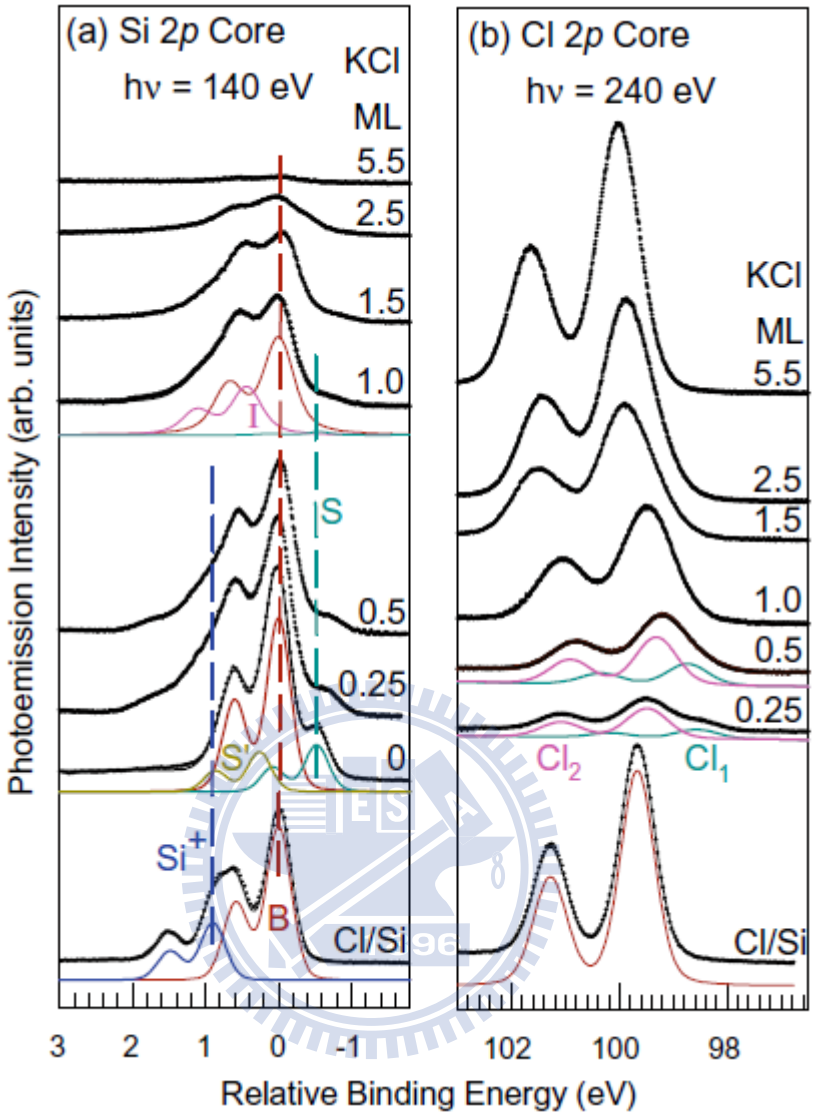

Figure 3. 1 (a) Si 2*p* and (b) Cl 2*p* core level photoemission spectra (circles) of Cl-Si(100)-2×1 surface and Si(100) surface with various amounts of deposited KCl, as labeled. The solid curves are fits to the spectra. The curves labeled B, S, I and Si^+ are the results of decomposition of the Si 2*p* spectra into contributions from the bulk, the clean surface, the interface layer and the Si-Cl species, respectively. The Cl 2*p* spectra at sub-monolayer coverage have two components Cl_1 and Cl_2. The energy zero in (a) refers to the $2p_{3/2}$ bulk position. To eliminate the band bending effect, the relative binding energy for the Cl 2*p* refers to the corresponding Si $2p_{3/2}$ line of the B component in (a). Dashed lines through the B, S, and Si^+ components are guides for the eye.

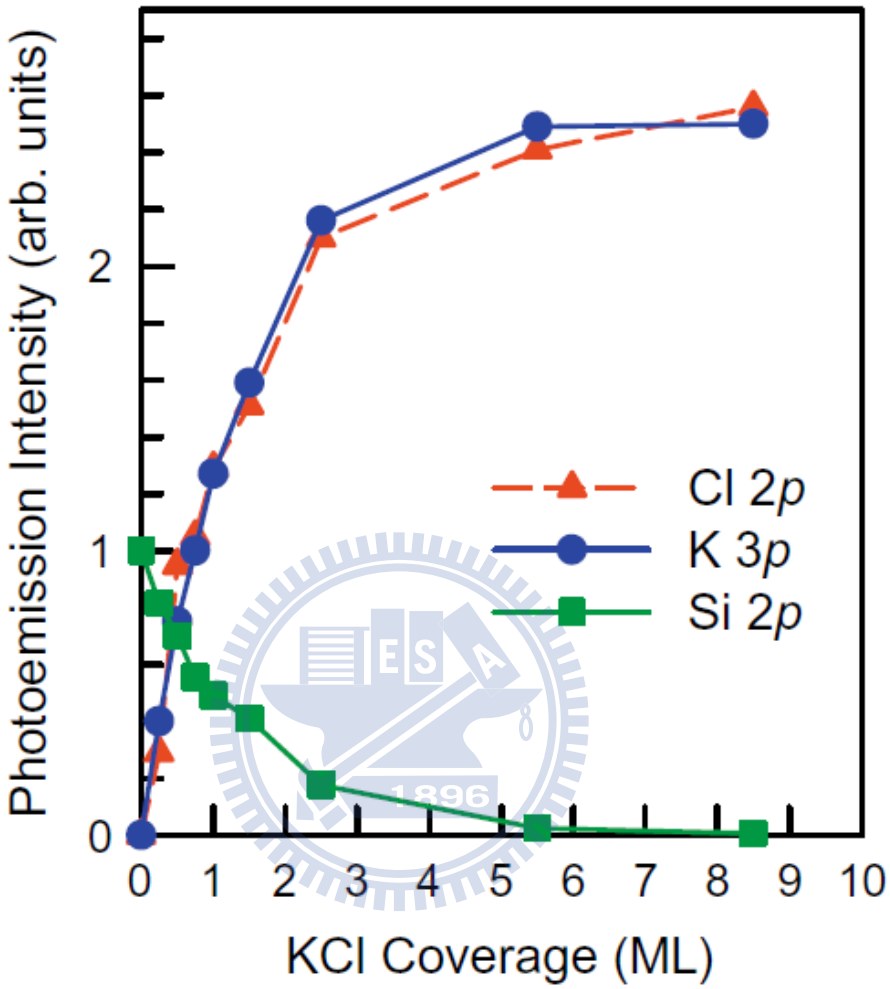

Figure 3. 2 Integrated photoemission intensities of Si 2*p*, Cl 2*p* and K 3*p* as functions of KCl coverage. Data for Cl 2*p* and K 3*p* are normalized to the intensity measured at KCl coverage of 1 ML. Si 2p is normalized to the clean surface before KCl deposition.

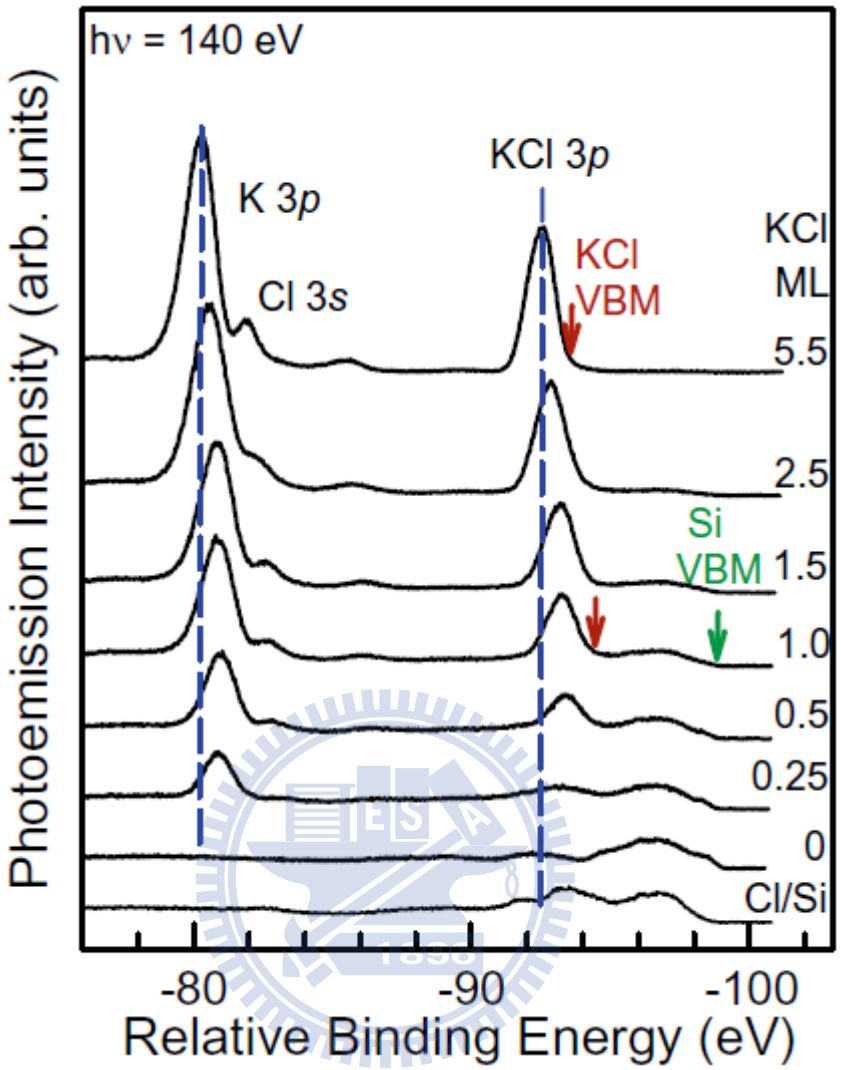

Figure 3. 3 Valence band region of Si(100) surface with various KCl coverage, as indicated. As in Figure 3. 1(b), the relative binding energy refers to the corresponding Si $2p_{3/2}$ line of the B component in Figure 3. 1(a). Vertical dashed lines are a guide to the eye to show the general trend in the binding energy shifts of K 2*p* and Cl 3*p*.

3. 3. 2 STM results

The clean double-domain Si(100) surface comprises rows of dimers [24]. Figure 3. 4 and Figure 3. 5 present the evolution of the Si(100) surface following KCl deposition at 330 K. In Figure 3. 4 white arrows indicate the dimer-row directions in the top Si layer before deposition. When a small amount of KCl is adsorbed, noisy images produced by the unstable feedback loop are commonly observed. Apart from a few dark sites on the dimerized surface as shown in the clearer images, such as that in Figure 3. 4a, no distinctive KCl adsorption speciesor cluster is observed at h < 0.2 ML. The dark sites have a similar appearance to those found in Cl adsorption on Si(100) [19]. The unstable scans and fewer-than-expected apparent absorption species together indicate that the deposited KCl molecules at low coverage, if not decomposed, are not strongly chemisorbed and are probably quite mobile on the clean Si surface. This finding agrees with the results of photoemission described earlier. As discussed in the preceding section, the valence band and core level spectra show no KCl characteristics until above 0.25 ML and that some of the adsorbed KCl molecules decompose. The dissociated Cl atoms easily generate Si-Cl bonds, which are likely responsible for the many dark sites in the image other than the original defects on the surface.

As KCl adsorption accumulates above 0.3 ML, many random bright protrusions develop and grow, as presented in Figure 3. 4b and c. Between these protrusions, the dimer rows remain clearly visible. At 0.5 ML, these protrusions have a more uniform size than at 0.3 ML and their apparent height is determined to be 1.6 Å. Their absence below 0.2 ML and their areal size suggest that these protrusions are probably nucleated clusters of KCl that are formed following critical super saturation of mobile KCl surface species. Above 0.6 ML, well-ordered c(4×4) arrays of protrusions appear and grow in size amid the disordered clusters, as displayed in Figure 3. 5a and Figure 3. 4d. Each c(4×4) cell has a single elongated elliptical protrusion, whose semi-major axis is perpendicular to the row of dimers in the substrate. Although the atomic features are not resolved, the size of these protrusions suggests that each protrusion is a KCl cluster. Such clusters are denoted Clusters A. At 1.0 ML the c(4×4) domains expand to fill the terraces (Figure 3. 5b). According to Figure 3. 4d and e, the c(4×4) areas are separated by domain boundaries with no apparent atomic ordering. At a coverage of over 1 ML, new clusters (Cluster B) appear as even brighter protrusions than Clusters A in Figure 3. 4e and Figure 3. 5b. The STM measurement does

not resolve details of the atomic structure of Clusters B. Clusters B randomly disperse in the area of c(4×4) domain boundaries and often form linear chains. Figure 3. 4f presents the line profile across Clusters A and B. The plot shows that the typical apparent corrugation in the c(4×4) regions is around 0.7 Å. The apparent height difference between Clusters A and B is approximately 1.0 Å.

The STM image such as that in Figure 3. 5c reveals that two dimensional islands emerge and grow as KCl grow above 2 ML. The carpet-like growth that is observed in the NaCl/Ge(100) system is not observed here. The apparent height of these islands (Figure 3. 6a) extracted from line scans is about 2.2 Å above Clusters B, which cover much of the surface. The apparent height of these islands above the top silicon layer is thus estimated to be about 4.8 Å. This measurement notably exceeds the value of 3.15 Å, which is expected for a single KCl monolayer, but is less than that for a double-layer. A previous study indicated that the increase in the effective tunneling barrier over the insulating thin films leads to the underestimation of the apparent height [4]. Another study demonstrated that the growth of a second alkali halide monolayer flattens the corrugated first monolayer on a similar covalent bonded Ge(100) surface [25]. Above observations indicate that these flat-top islands are either KCl double layers or triple layers.

Figure 3. 5d presents the surface morphology after 3.6 ML of KCl deposition. The main features in the image are large-area islands on flat terraces or on even larger islands. The step height (Figure 3. 6b) of these islands measures about 3.0 Å, i.e. close to the height of a single KCl monolayer. The step structure with steps of alternative types A and B found in the clean Si(100) before KCl deposition remains clearly discernible in the large area image. Again, islands do not extend across the monoatomic steps because of the mismatch between the lattice spacings of the Si(100) substrate and the KCl films. These findings indicate that further KCl deposition above 2 ML follows pseudo layer-by-layer growth and that KCl films with a thickness of more than two (or three) layers no longer have a commensurate KCl/Si(100) interface as schematically shown in Figure 3. 5e. In heteroepitaxy small lateral lattice mismatches generally produce layer-by-layer growth while large mismatches result in three-dimensional growth. Local-density approximation (LDA) calculations have demonstrated that the adsorption energy of the first NaCl layer on the Ge(100) surface is 0.2654 eV/(1×1) unit cell [25]. The adsorption energy increases to 0.3844 eV and 0.4069 eV per unit cell for the second and third layer, respectively, because

of the presence of more bulk-like ionic solids and reduction in the non-planar arranged cations and anions in the first layer. The adsorption energy of the first NaCl layer on Ge(100) is compatible to that found on Ag(100) [7]. These considerations support our postulation that thick KCl films on Si(100) have a structure similar to the bulk crystal. Therefore, the KCl growth proceeds in a layer-by layer fashion as in alkali halide/ metal systems.

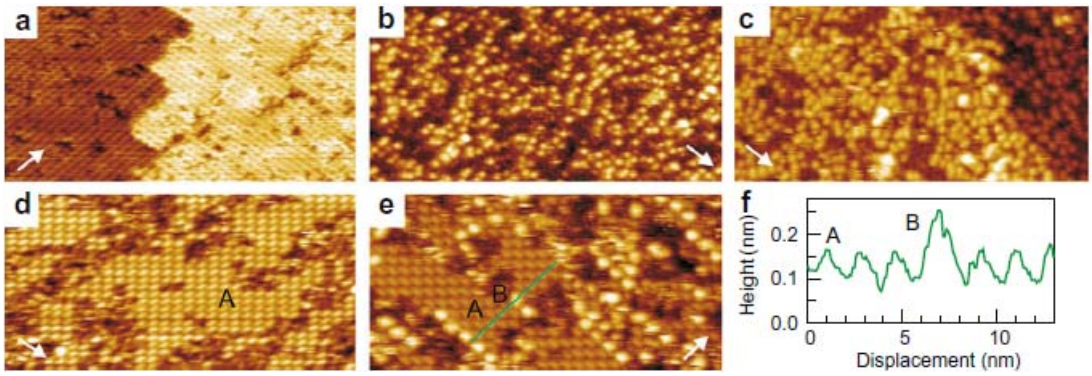

Figure 3. 4 STM images of coverage evolution with deposition of (a) 0.1, (b) 0.3, (c) 0.5, (d) 0.8 and (e) 1.2 ML KCl on Si(100)-2×1 surface. The sample bias was -2.4 V. The images cover an area of about 40×20 nm^2. The white arrows indicate the dimer-row direction in the top silicon layer. (f) Apparent topographic height profile along the green line in (e) from lower-left to upper-right. B: position of one Cluster B.

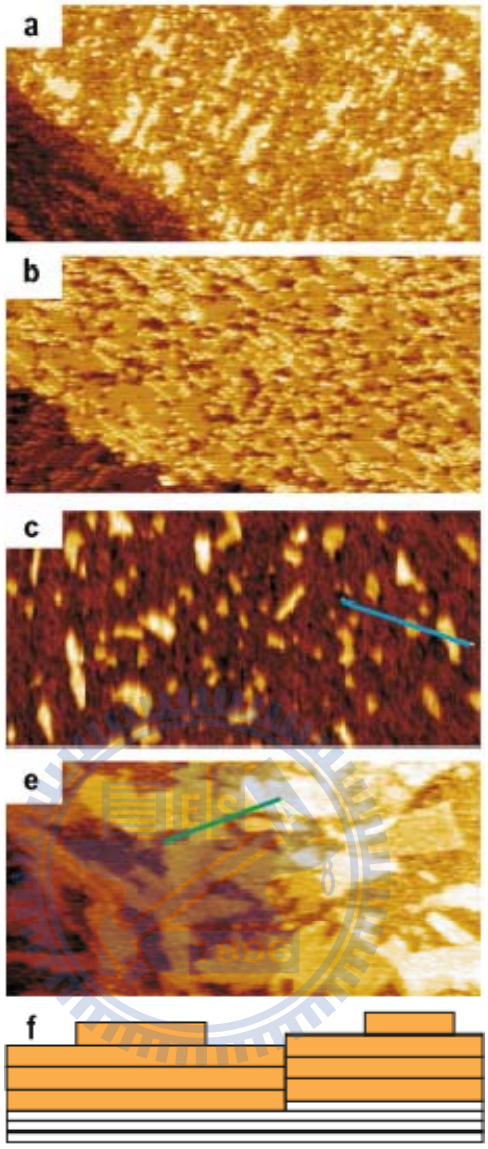

Figure 3. 5 Large-area STM images of coverage evolution with deposition of (a) 0.6, (b) 1.2, (c) 2.4 and (d) 3.6 ML KCl on the Si(100)-2×1 surface. The sample bias was -2.4 V. In (d), two substrate steps (0.14 nm in height) in the lower-left and upper-right corners remain discernible. (e) Schematic showing KCl films (orange) of several layers thick has a bulk-like structure on Si(100). Two atomic steps with heights of 0.315 and 0.14 nm show the interlayer spacings for KCl(100) and Si(100), respectively. (a), (b) and (c) cover an area of 200×100 nm^2 and (d) covers an area of 300×150 nm^2.

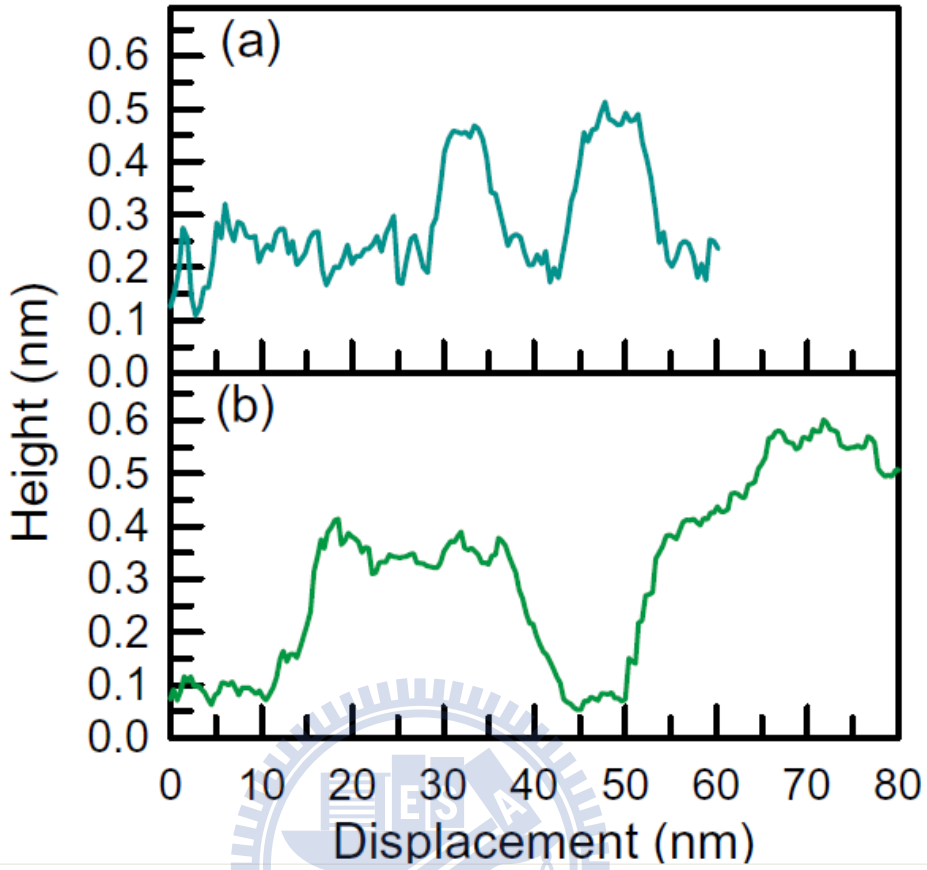

Figure 3. 6 Apparent topographic height profiles (a) and (b) (from left) along lines marked in Figure 3. 5 c and d, respectively.

3. 3. 3 Atomic model of c(4×4) surface structure

As described in Section 3. 3, the c(4×4) domains cover most of the surface at 1 ML KCl coverage. The STM image, such as that in Figure 3. 7 a, shows only one protrusion in one c(4×4) unit cell. Details on the atomic scale are not resolved. To determine the atomic structure of the grown KCl layer, we used the Vienna *ab initio* Simulation Package (VASP) code within density-functional theory of LDA. The Ceperley-Alder exchange-correlation function, as parameterized by Perdew and Zunger, was adopted. Following the standard procedure, a 4×4 repeated-slab supercell model was adopted. Each slab has ten atomic layers of Si and the adlayers of K and Cl; H atoms are bound to the bottom-layer Si atoms to saturate their dangling bonds. The heights of the supercell in the [001] direction were fixed at 6 nm, which sufficed to prevent coupling between the slabs. By fixing the bottom double Si and H layers, the structure was optimized until the residual force acting on each atom was less than 0.01 eV/Å.

Figure 3. 7 b, c and d present the top view, the perspective view and the projections of ion positions of the relaxed structure for 1 ML KCl/Si(100), obtained by VASP calculations. Figure 3. 7 b indicates that the projection of Cl ions on the (100) plane remains roughly a two-dimensional square lattice. A sodium cation is located near the center of each square of anions. This arrangement of ions of alternating charge reduces the Madelung energy, as in all ionic crystals. However, the second nearest-neighboring (Cl-Cl) separation of KCl crystal is 4.32 Å, almost 13% greater than the lattice constant (3.83 Å) of the unreconstructed Si(100) surface. Figure 3. 7c and d show that the ions increase their separations by forming four micro-facets, or a square pyramid-like shape, to reduce the excess energy associated with overlapping in atomic orbits. The angle of inclination of the pyramid is about 33°, yielding a nearest-neighboring K-Cl separation that is similar to that of a KCl crystal. The alternative layer structure of the pyramidal-arranged cations and anions also helps to reduce the flat-lying dipoles. Structural details and its electronic properties of this c(4×4) model can be found elsewhere [26].

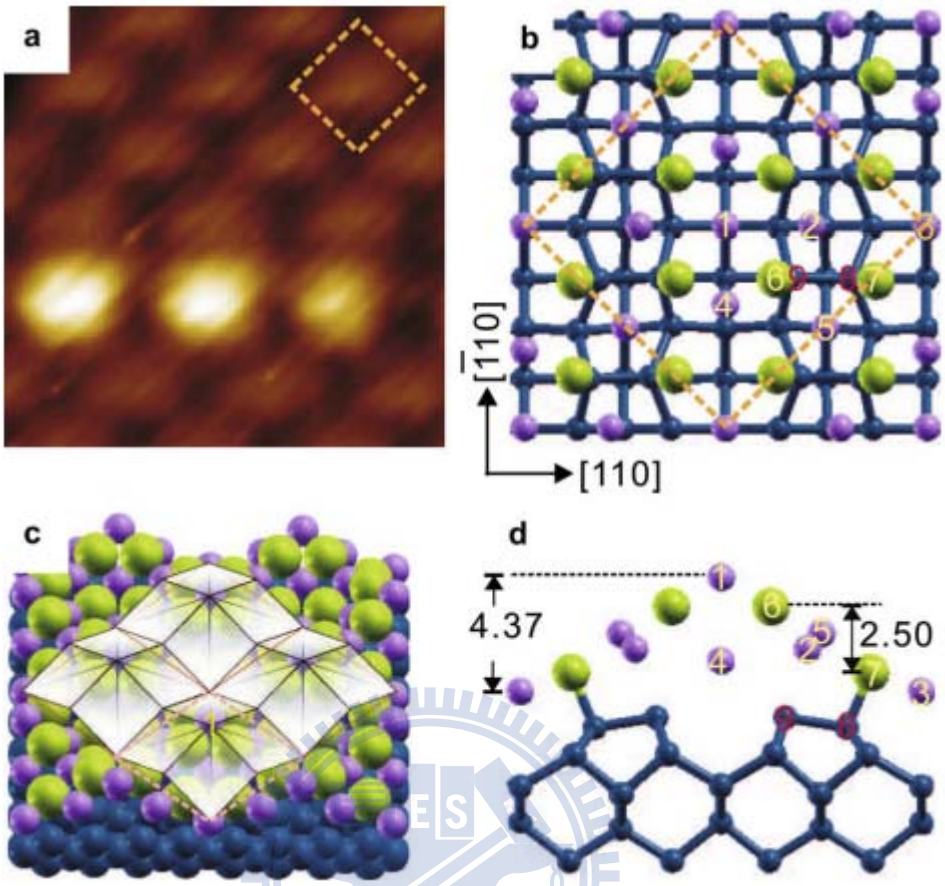

Figure 3. 7 (a) Close-up image of c(4×4) structure extracted from Figure 3. 5b. Pink dashed rectangle denotes unit cell of ordered Cluster A. Bright protrusions on lower area are Cluster B. (b) Top view, (c) perspective view, and (d) (1,1,0) projection of atomic model of c(4×4) structures. Blue, green and purple circles represent Si, Cl and Na atoms, respectively.

3. 4 Conclusion

The growth and morphology of KCl thin films deposited on a Si(100) surface at 330 K in the coverage range of 0-5.5 ML were observed by combined photoemission spectroscopy and scanning tunneling microscopy (STM). At low coverage, some KCl molecules dissociate. Above 0.3 ML, adsorbed KCl precipitates in clusters. At about 1 ML coverage, most surface area is covered by regular clusters (Cluster A) that produce a c(4×4) ordered surface structure. *Ab initio* calculations support a novel four-sided pyramidal model for the first KCl monolayer. Between 1 and 2 ML, further adsorbed KCl coalesces into regular clusters of the second kind (Cluster B). The atomic structure of Clusters B was not resolved. Above 2 ML, pseudo-two-dimensional growth occurs, while the monoatomic steps on the Si(100) substrate advance through the growing films.

Chapter 4 NaCl nanofilms on Si(100) grown by MBE

4. 1 Introduction

The epitaxial growth of halides on semiconductor surfaces has attracted much attention because of potential applications in microelectronic and optoelectronic devices, as well we scientific interest in the basic principle of epitaxial growth and heterostructure physics[27, 28]. Halide chlorides are a class of ionic solids with high fractions of ionic character. NaCl/Si(100) is a prototypical system for the heteroepitaxy of small-lattice-mismatch ionic crystals/covalent crystal. The second nearest-neighbor separation R_1 for an NaCl crystal is 3.98 Å. The surfac lattice constant *a*, or the period of unreconstructed Si(100)-1×1, is 3.84 Å. The lattice mismatch at the heterostructure of NaCl/Si(100) is close to 4%. Previous studies have established that NaCl can grow epitaxially on Ge(100) with a high degree of quality under suitable conditions[4, 14-16]. An STM measurement suggests that the growth of NaCl begins with a carpet-like double-layer NaCl film. In an electron energy loss scattering (EELS) measurement Zielasek, Hildebrandt and Henzler found electronic states at the NaCl/Ge interface and suggested that the dimerization of the Ge(100) surface is not eliminated at the NaCl/interface - even if the thickness of NaCl rises to 20 ML[13]. Scanning tunneling microscopy (STM) is powerful tools to investigate surface local atomic structure. Up to know, STM studies of alkali halide thin films grown on semiconducting substrates have been carried out for the systems KCl/Si(100), NaCl/Ge(100), KBr/InSb(100), LiF/Si(100), and KI/Si(100)[4-6, 29, 30].

For large lattice mismatch systems, the growth of alkali halide on the Si and Ge surfaces at around one monolayer coverage does not yield an ordered surface structure. For example, sub-monolayer LiBr (R_1=3.89 Å) and LiF (R_1 = 2.85Å) are adsorbed randomly onto Si(100) (a=3.84 Å) at room temperature[3, 6]. Guo and Souda observed that KI (nearest-neighbor separation R_0 =3.53 Å) dissociative adsorbs on the Si(100) surface at a coverage of less than 0.5 ML. Although thick flat films can be obtained, the growth of KI, LiF and LiBr on Si(100) and Si(111) surfaces proceeds by the Volmer-Weber (VW) mechanism of island growth as a result of the interfacial lattice mismatch.

In the present work, we report on XPS spectra and STM images of NaCl films,

which were grown on clean Si(100)- 2×1 surfaces. The lattice misfit of this system is 4%, and we have already achieved epitaxial growth of NaCl films, and study the growth mode of NaCl on Si(100)-2×1 by STM and XPS.

4. 2 Experimental details

The single crystal Si(100) with size of 1×10 or 3×10 mm^2 was sliced from an Antimony doped wafer with the resistance of 0.01 Ω • cm. The clean Si(100) surface was obtained *in situ* by direct heating to 1450 K for a few seconds after degassing at 900 K for several hours. NaCl powder of 99.99% purity was evaporated from an alumina crucible by a feedback current flux controlled electron bombardment beam. The deposition rate was measured by a quartz-crystal thickness monitor. The coverage of NCl adsorbated in ML (denoted by θ), was estimated from the exposure time, assuming the sticking coefficient is 1. The ML is referred to the surface density of the unreconstructed Si(100) surface, i.e. 1 ML=6.8×10^{14} cm^{-2}. The substrate temperature during growth was approximately 330 K.

The photoemission spectra were recorded in a separated μ-metal-shielded chamber with a based pressure of ~ 3×10^{-10} torr at the Taiwan Light Source laboratory in Hsinchu, Taiwan. Synchrotron radiation from a 1.5 GeV storage ring was dispersed by a wide-range spherical grating monochromator (SGM). The photocurrent from a gold mesh placed in the synchrotron beam path was monitored to determine the relative incident photon beam flux. Photoelectrons were collected from 45° off normal emission and analyzed by a 125-mm hemispherical analyzer. The overall energy resolution was better than 120 meV. The STM measurement was taken in a separated UHV chamber with a base pressure of 8×10^{-11} torr. The tunneling current was about 0.1 nA. The topographic height measurement did not strongly depend on the sample bias around -2.4 V typically used.

4. 3 Results and discussion

4. 3. 1 Photoemission results

High-resolution X-ray photoemission spectroscopy can be performed to distinguish between atoms at nonequivalent sites and in different chemical bonding configurations, base on shifts in their binding energy [31]. Figure 4. 1 (a), 1(b), and 1(c) respectively presents a series of surface-sensitive Si 2*p*, Cl 2*p*, and Na 2*p* core level spectra (dot) for the Si(100)-2×1 surface with various amounts of NaCl. All fitting was least-squares fitting. Identical Voigt line shapes that each consists of a pair of spin-orbit split doublets were used to decompose the Si 2*p* and Cl 2*p* core level spectra into overlapping components (curves) [17]. The solid curves represent the fitting results that overlap the data points. Spectra of the chlorine terminated Si(100)-2×1 (Cl/Si(100)) are also presented for reference. The Si 2*p* core level spectrum (Figure 4. 1 (a), bottom) has two components, B and Si^+, that are separated by 0.90 eV. The B component was responsible for the emission from the bulk and the Si^+ component from the surface Si-Cl species[21, 31]. The corresponding Cl 2*p* spectrum for Cl/Si(100) (Figure 4. 1 (b), bottom) can be analyzed in terms of only a single component that has a pair of split doublets separated by 1.60 eV, implying that all Cl has the same Si-Cl monochloride bonding configuration[18, 19].

Before NaCl deposition, the Si 2*p* spectrum (Figure 4. 1(a), second from bottom), which was obtained from the clean Si(100)-2×1 surface, has a bulk component (B) and surface-shifted (-0.52 eV) components (S). The surface related components of S peak has been attributed to emission from the top atoms of symmetric dimers. The B component was responsible for the emission from the bulk. All core level binding energies are referenced to the bulk Si $2p_{3/2}$ position (99.5 eV) relative to the valence band maximum.

At submonolayer coverage of NaCl deposition, the intensity of the *S* component declines with increasing coverage, suggesting a much reduced charge transfer between the up- and down-atoms in a dimer. Tails on the higher binding energy side for Si 2*p* with $\theta > 0.4$ ML can be located near the position of the Si^+ component. These signatures suggest that a portion of deposited NaCl molecules decomposes and Si-Cl bonds are presented on the surface. Noticeably, at θ=0.4 ML the Si 2*p* spectra become broader on the higher binding energy side. Thus two additional components, Si^+ and *I*, are included in our fitting. The

component of Si^+ peak, shifted by +0.9 eV from B, is apparently responsible from the Si-Cl surface species [21, 32, 33]. Accordingly, a fraction of the adsorbed NaCl dissociate, and the peak of *I* appears after the NaCl on the Si(100) surface. Thus, we can regard the peak of *I* as the emission from the top Si layer under the NaCl film. The shift of +0.42eV to the higher binding energy side also could be explained that it is positively charged for the top Si layer under the NaCl film.

Figure 4. 2 (a) plots the intensities of S, *I*, Si^+ components in Si 2*p* associated with the coverage of deposited NaCl. At θ=0.4ML, the coverage of the Si^+ (0.23ML) is larger than *I* (0.11ML), indicating that a more portion of deposited NaCl (0.23ML) molecules decomposes and Si-Cl bonds and ionized Na are present on the surfaces, and a fewer portion of deposited NaCl to adsorption on the Si atom (Si-Cl-Na) by a form of a dipole molecule of Na-Cl (0.11ML). Because the component of *I* of Si 2*p* in Figure 4. 1(a) spectrum, the *I* shifts to the higher binding energy side by +0.42eV which is less than the Si^+ components shifts to the higher binding energy side by +0.9eV, indicating that the adsorbed the Na-Cl dipole molecule has fewer charge transfers from the Si to Na-Cl (Si-Cl-Na) than the covalent bonds of Si-Cl. So Na-Cl does not completely bond with Si to form a covalent bond to be Si-Cl; instead, Na-Cl bond with Si by Si-Cl-Na. In Figure 4. 2 (a), above the θ=0.6ML the coverage of *I* (~0.38 ML), S^+(~0.23 ML), and S(~0.39 ML) do not change with the furthering deposition of the NaCl. However,Figure 4. 2 (b) plots the integrated intensities of the Si 2*p*, Cl2*p*, and Na 2*p* peaks. Above θ=0.6ML the Cl and Na increases with the amount of NaCl deposited. Therefore, above θ=0.6ML the second NaCl layer begins to grows on the first NaCl layer, and first NaCl layer has residual dangling bonds (S~0.39ML), Si-Cl-Na (~0.38ML), and Si-Cl (~0.23ML).

4. 3. 2 STM results

The initial clean Si(100) surface (not shown) forms a (2×1) reconstruction consisting of parallel rows of dimers. Each surface Si atom has one dangling bond. On the vicinal Si(100) surface, two different types of single-height steps, S_A and S_B, of height 0.15 nm separates perpendicular domains of (2×1) reconstruction [34].

Figure 4. 3 (a) shows a STM topographic image scanned at a sample bias of -1.8 V and a tunneling current of 0.23 nA for a Si(100)-2×1 surface predosed with 0.1 ML NaCl molecules at room temperature. The unreacted dangling bonds of Si atoms appear as bright dimer rows and the reacted dangling bonds of Si atoms appear as dim color. The XPS revealed that below θ< 0.4ML the adsorbed NaCl to form a Si-Cl and Si-Cl-Na, so in Figure 4. 3 (a) the Si atoms dangling bonds have been eliminated by the newly formed Si-Cl and Si-Cl-Na to be a dim color [19]. In Figure 4. 3 (b) the small area pattern in the solid boxes enclose can be found on the surface, and the bright spots in the small area pattern have the same bright as the unreacted dimer rows of Si. Therefore we suggest that the bright spots in the small area pattern are the dangling bonds, and the dim color is Si-Cl or Si-Cl-Na.

Figure 4. 4 shows the evolution of the Si(100) surface after the various amounts of NaCl deposition at room temperature. At the S_A step edges, the direction of the dimer bonds on the upper terrace is oriented perpendicular to the step edge, whereas it is oriented parallel to the step edge at S_B steps. In Figure 4. 4 (a), at θ= 0.65ML the dimer rows of Si(100)-2×1 cannot be observed, and the bright spots (0.35ML) are scattered on the Si surface. Because Figure 4. 4 presented that dimer colors of the Si(100)-2×1 surface is due to the adsorption of the molecule NaCl, the bright spots in Figure 4. 4 (a) are the dangling bonds of the Si and these dangling bonds have the c(2×4), c(2×2), and p(2×2) structure due to the arrangements of Si-Cl and Si-Cl-Na as shown in Figure 4. 4. The growth first layer of NaCl/Si(100) and KCl/Si(100) (c(4×4) structure) can be observed the ordered structure, but the an STM measurement suggests that the growth of NaCl/Ge(100) begins with a carpet like double-layer NaCl films [4, 30]. It is well known that the growth mode in heteroepitaxy is dependent upon the surface free energy and on the lattice mismatch. The lattice mismatch of NaCl/Si(100) (~4%), KCl/Si(100) (~13%) are larger than NaCl/Ge(100) (~0.5%). So at submonolayer of NaCl molecules adsorbed on Si(100)-2×1 surface, the NaCl molecules cannot be combined with other NaCl molecules to be a double layer islands on Si(100)-2×1.

The larger lattice mismatch of NaCl/Si(100) (4%) results in partial of the dissociated NaCl (Si-Cl) and partial of the Si-Cl-Na.

The STM image such as that in Figure 4. 4 (b) reveals that two dimensions islands emerge and grow as NaCl grow above 0.65ML. The carpet-like growth that is observed in the NaCl/Ge(100) system is not observed here. The apparent height of these islands Figure 4. 5(b)) extracted from line scans is above 3.8 Å above the first NaCl layer, which cover much of the surface. The first layer NaCl on Si(100) reduced the dangling bonds of Si at θ=0.65ML and also reduce the reactive interface between the dangling bonds and NaCl molecules; moreover, the XPS indicated that $\theta > 0.6$ ML the dangling bonds are still under the second NaCl films. Therefore, the second layer of NaCl can grow to double layer islands without the effect from the dangling bonds of Si. Another notably study in Figure 4. 4 (b) is that these small islands much prefer to grow close the step A edge on the lower terraces. Figure 4. 4 (c) presents the surface morphology after 1.55 ML of NaCl deposition. The main features in the image are large area islands on flat terraces or cross two step (step A and step B). Figure 4. 5 shows the apparent topographic height profiles and corresponding schematic of NaCl films (large yellow rectangles) of one or two layers thick on Si(100) along the arrows in (a) Figure 4. 4 (a), (b) Figure 4. 4(b), and (c) Figure 4. 4 (c) respectively. The apparent layer thickness of double- layer NaCl films are about 0.38 nm. The NaCl clusters and dissociated species dispersed on the Si(100) surface are represented by concave boxes of the top Si surafecs.

Figure 4. 7 shows the sphere model of the first layer at 0.65ML NaCl on Si(100). Figure 4. 7 (a) p(2×4), (b) c(2×2), and (c) p(2×2) correspond to Figure 4. 6 (b), (c), and (d), respectively. NaCl crystal which evaporated from the EFM3 is a diatom molecules of NaCl (Na-Cl), so the bond length 2.3 Å of the NaCl diatom molecule is considered and the NaCl diatom molecule is a dipole molecule. According the previous study for the Na/Si(100)-2×1, the Na atoms sit on the hollow sites or the valley sides of the Si(100)-2×1 surface[35, 36]. So in our model for first NaCl layer on Si(100), Na atoms is only on the hollow and valley sites of the Si(100)- 2×1 surface to be considered. As shown in Figure 4. 7 (a) p(2×4) and (c) p(2×2), if the Na-Cl molecules are adsorbed at the same dimer (Si-Cl-Na) and the orientations of the two dipole Na-Cl are anti-parallel and the Na is at the hollow sites of the Si(100), above or below the Si-Cl-Na dimer only has a pair of Si-Cl and dangling bond at the same dimer and the Na atome sites at the nearest valley sites position between the two dimer

rows. The distance between the top Si atom and the nearest hollow side is about 2.3 Å which close the bond length of Na-Cl (2.3 Å), so the Na-Cl can bond with Si atom by the Si-Cl-Na. Because the distance between the Si-Cl and the valley sites of Si(100) (~ 3Å) is larger than the bond length of Na-Cl (2.3Å), the ion bond of the Na-Cl molecule breaks. Therefore Cl forms chemical bond with Si (Si-Cl) and left Na on the surface. The left Na has no nearest hollow sites of Si(100) surface to occupy, so the Na is onto the nearest valley sites between the two dimer rows. For the Figure 4. 7 (b), the dangling bond and Na-Cl form a zigzag-structure, and a sigzag-structured chain is an ordered array of DB-Si-Si-(Cl-Na) dimers, in which DB sites and (Cl-Na) sites in neighboring dimers are anti-phase with each other. The c(2×2) structure can be regarded as a combination of more than two neighboring zigzag DB-Si-Si-(Cl-Na) chain.

Table 4. 1 shows the calculated results of the STM images. In calculation of the NaCl coverage, more than 3600 Si sites were counted from a 50×50 nm^2 image. The calculation for boundary (Si-Cl-Na) indicated that the Na-Cl must to be in the boundary, ex. the boundary between c(2×4) and p(2×2). The XPS results revealed that *I* component is ~40% and "Si^+"is ~23% for the NaCl coverage over 0.6ML. For the STM results, the *I* (~40%) can be regarded as the contribution of pattern (Si-Cl-Na = 33%) and boundary (Si-Cl-Na = 5%) and the Si^+ (~23%) can be regarded as the contribution of pattern (Si-Cl--Na=14%) and Si-Cl =10%. The Si-Cl is the calculation from the darkest color in the STM images. The darkest color in the STM image cannot be distinguished, but from XPS results the darkest color can be suggested as Cl-Si-Si-Cl without Na atoms around the Cl atoms.

Figure 4. 8 (a) shows the atomic resolution for the second layer of NaCl on Si (100) surface and the well-defined protrusion which has a lattice constant of the square lattice of 3.82 Å is observed. As the previous study of the NaCl layers, only one and two ions (Na^+ or Cl^-) is observed in STM images[1, 37]. The First principles calculations performed for NaCl/Al [1] and STM images of NaCl/Cu(311)[9] indicated that the species is the Cl ion of the NaCl is imaged as white protrusion. So the well-defined protrusion is the Cl ion of NaCl(100) plane on Si(100) surface as shown in Figure 4. 8 (a).

Figure 4. 9 shows an filled state STM images of the 0.95ML NaCl with different voltage (a) -2.3 V (b) -2.5 V. In Figure 4. 9 (a) and (b), the section height profiles in Figure 4. 9 (c) indicates that the height of the islands are both about 3.8 Å, suggesting that the second NaCl

layer grew on Si(100) in a double-layer fashion, and proving that the height profile measurement of the second NaCl was voltage independent for STM image between V_s = -2.3V to -2.5V. The thickness value of 3.8 nm is larger than 2.8 Å which expected for a single NaCl monolayer. However, it is clearly below the idea double layer height of 5.6 Å. This is certainly due to the fact that the tunneling barrier is not only determined by the vacuum between tip and NaCl layer, but also by the NaCl itself, which does not provide the density of states between the Fermi energies of the tip and Si substrate.

Figure 4. 10 (a) shows the 200×100 nm^2 morphology of the Si(100) surface with 0.95ML of NaCl. Figure 4. 10 (b) is the roomed-in STM image from the solid box enclosed selected area in Figure 4. 10 (a). In Figure 4. 10 (b) beside the second of double layer NaCl, the first NaCl layer which had the local pattern of the residual dangling bond was observed as discussed in Figure 4. 10. So Figure 4. 10 (b) indicated the second layer of the double layer NaCl really grew on the fist NaCl. The second layer of NaCl which grows on the first layer of NaCl islands is appear at the coverage over 0.65 ML.

4. 4 Conclusions

We have studied the adsorption of NaCl on the Si(100)-2×1 surface at room temperature from low coverage (0.1 ML) up to high coverage (2.25ML) with synchrotron x-ray core level photoelectron spectroscopy and scanning tunneling microscopy. As $\theta < 0.6$ ML, the XPS and STM results together indicated that the partial NaCl dissociated to form Si-Cl and left Na on the surface, and partial NaCl bonded with Si atoms to form Si-Cl-Na. At $\theta = 0.65$ ML (the first NaCl layer on the Si (100)-2×1), the residual dangling bonds of the Si have c(2×4), c(2×2), p(2×2) ordered structure due to the arrangement of Si-Cl-Na and Si-Cl. Between 0.65 and 2.25 ML, the double layer islands of NaCl grew on the first NaCl layer and the XPS results indicated that the residual dangling bonds of the first layer is still under the second NaCl layer and the amount of the residual dangling bonds are not decreased above $\theta > 0.6$ML. The atomic resolution of STM images revealed that the doubled layer islands of NaCl on Si (100) surface have the well-defined protrusion which has a lattice constant of the square lattice of 3.82 Å.

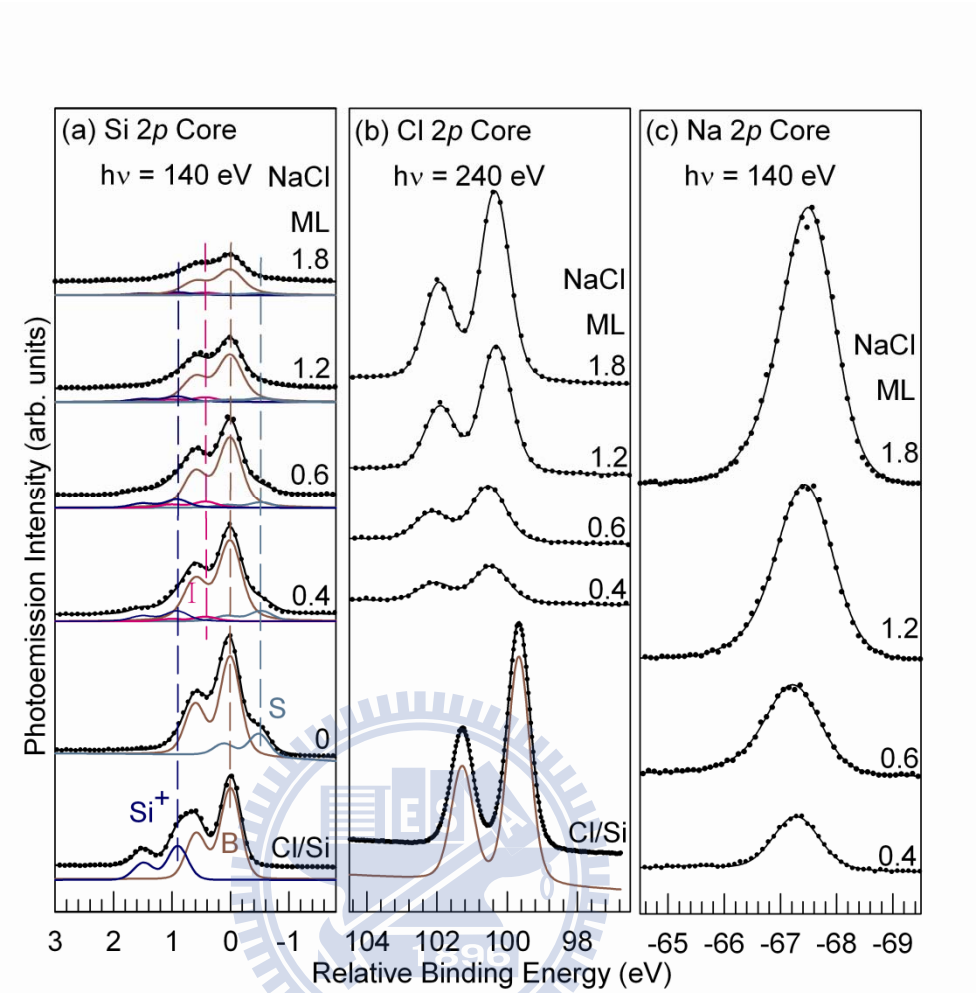

Figure 4. 1 (a) Si 2*p*, (b) Cl 2*p*, and (c) Na 2*p* core level photoemission spectra (circles) of Si (100) surface with various amounts of NaCl deposition, as specified. The solid curves are fits to the spectra. The curves labeled B, S, I and Si^+ are the results of the decomposition of the Si 2*p* spectra into contributions from the bulk, the clean surface, the interface layer and the Si-Cl species, respectively. The energy zero in (a) refers to the $2p_{3/2}$ bulk position. To eliminate the band bending effect, the relative binding energy of the Cl 2*p* and Na 2*p* corresponds to the Si the $2p_{3/2}$ bulk position in (a). Dashed lines through the B, S, and Si^+ components are guides for the eye.

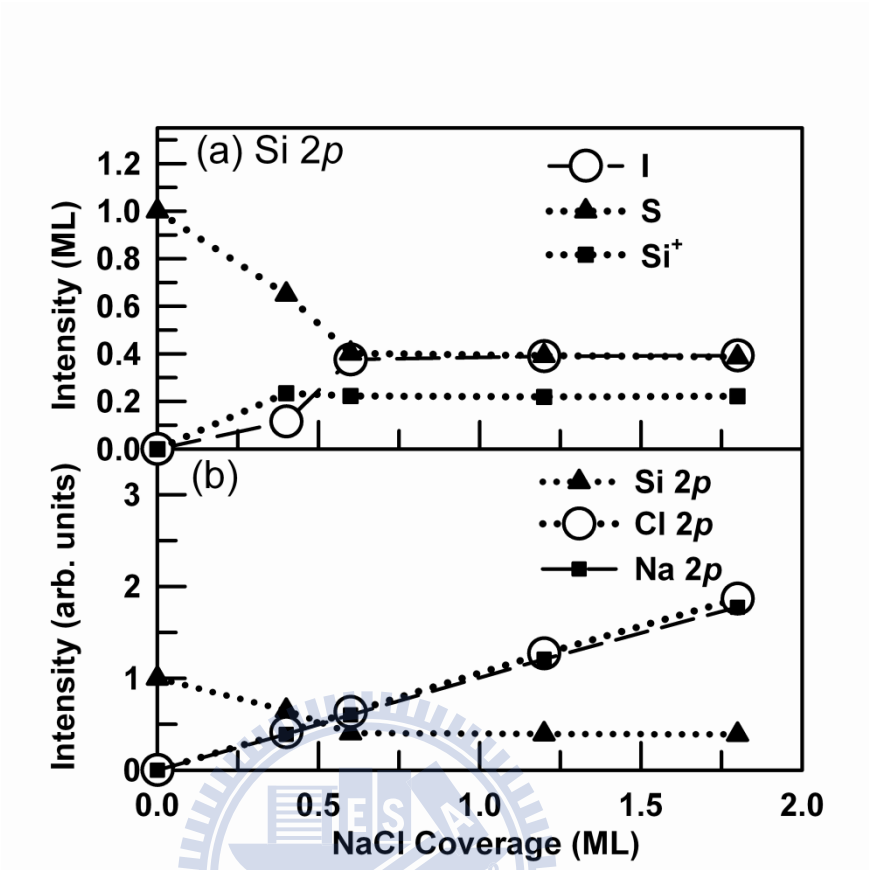

Figure 4. 2 (a) Evolution of the components S, S^+, and I intensity of the Si 2*p* photoemission spectra of Figure 4. 1 (a). The intensity of S^+ is normalized to the component of S^+ of the Cl_2 terminated Si(100)-2×1. The intensity of S is normalized to the component of S of the clean Si(100)-2×1 surface. (b) Integrated photoemission intensities of Si 2*p*, Cl 2*p*, and Na 2*p* as functions of NaCl coverage. Data for Cl 2*p* and Na 2*p* are normalized to the intensity measured at NaCl coverage of 1 ML. Si 2*p* is normalized to the clean surface. The dashed and the solid lines are simple guides.

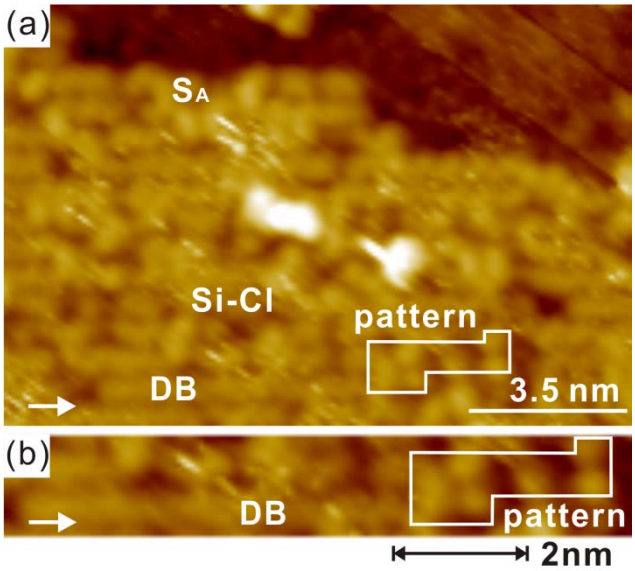

Figure 4. 3 (a) STM images of 0.1 ML NaCl on Si (100) with V*s* = -1.8 V. (b) the STM image roomed in from Figure 4.3 (a).

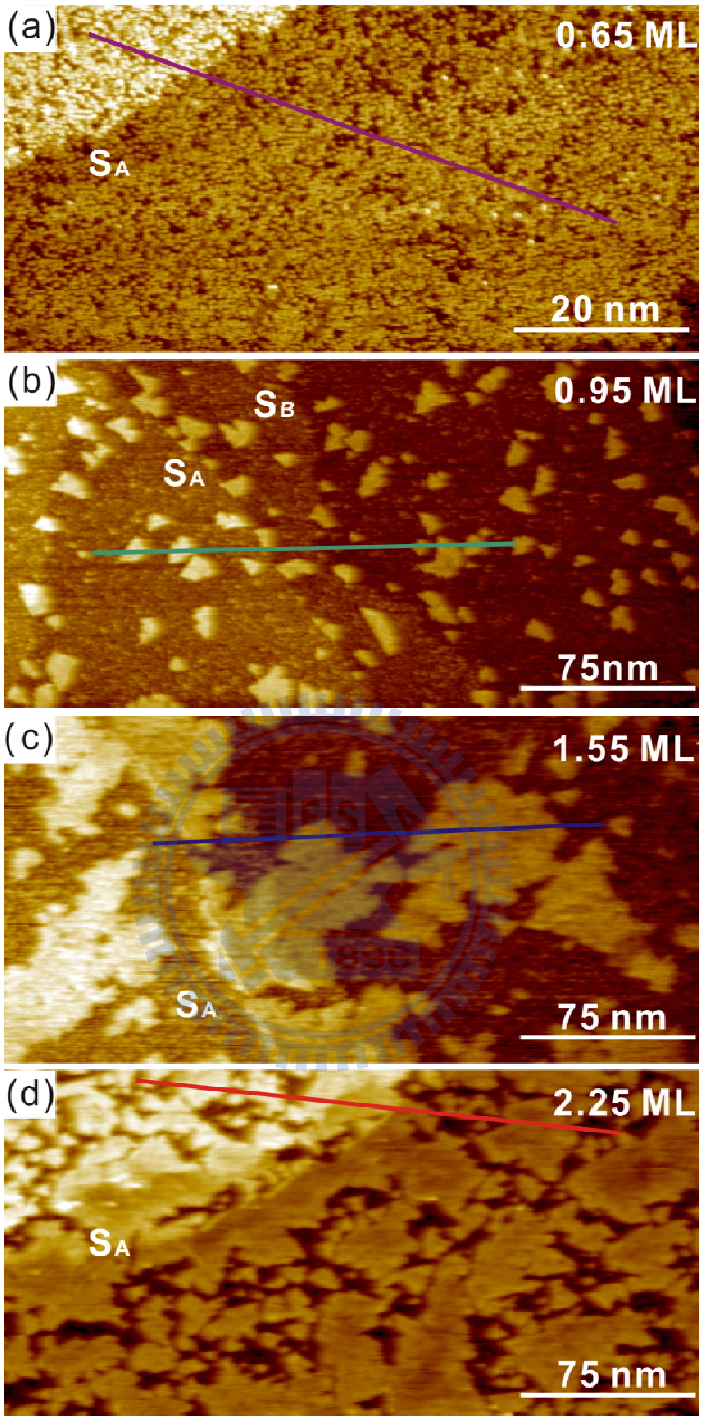

Figure 4. 4 Filled-state STM images showing coverage evolution with deposition of (a) 0.65, (b) 0.95, (c) 1.55, and (d) 2.25 ML NaCl on Si(100) surface as labeled. All images are obtained at room temperature with $I_T = 0.23$ nA and Vs = (a) -2.05, (b) -2.3, (c), and (d) -2.8. The images cover an area of about (a) 80×40 nm^2, and (b)-(d) 300×150 nm^2. Apparent topographic height profiles along the color line are shown in Figure 4. 5.

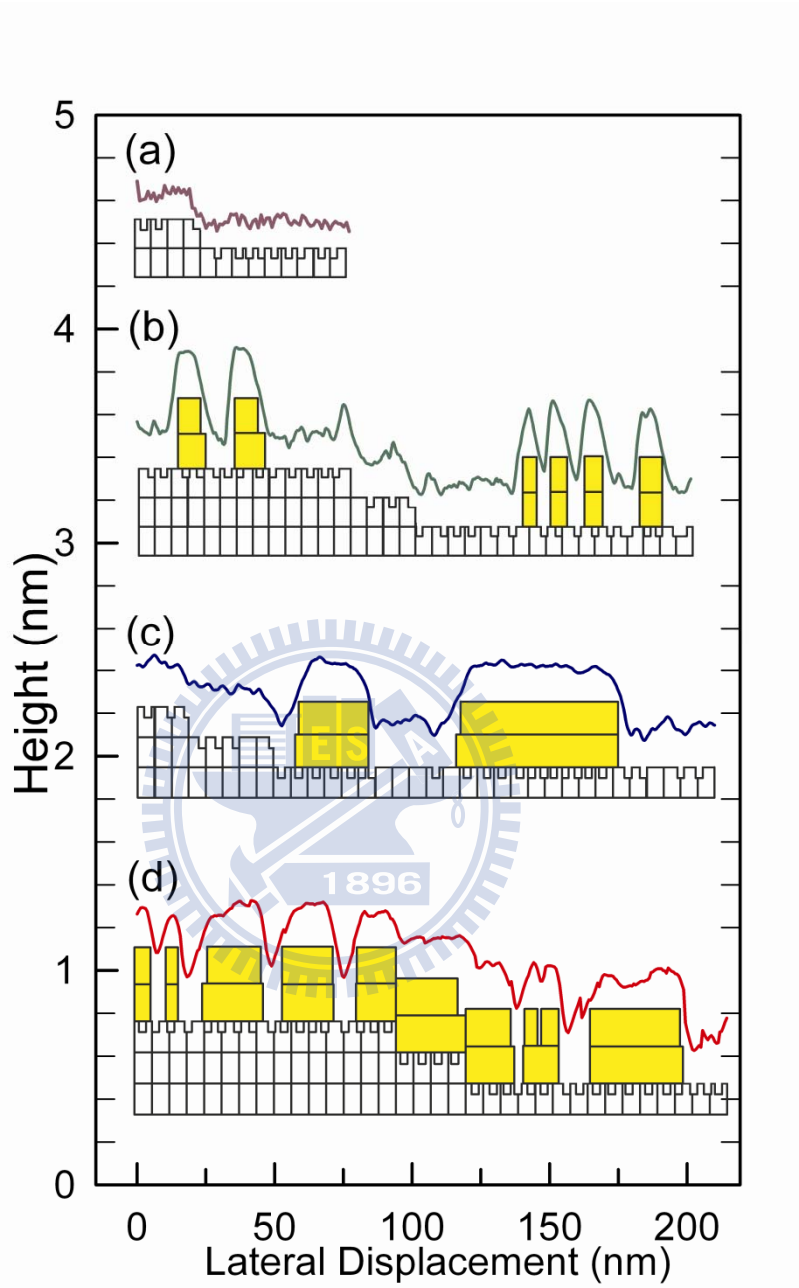

Figure 4. 5 shows the apparent topographic height profiles and corresponding schematic of NaCl films (large yellow rectangles) of one or two layers thick on Si(100) along the arrows in (a) Figure 4. 4 (a), (b) Figure 4. 4 (b), and (c) Figure 4. 4 (c) respectively. The apparent layer thickness of double- layer NaCl films are about 0.38 nm. The NaCl clusters and dissociated species dispersed on the Si(100) surface are represented by concave boxes of the top Si surfaces.

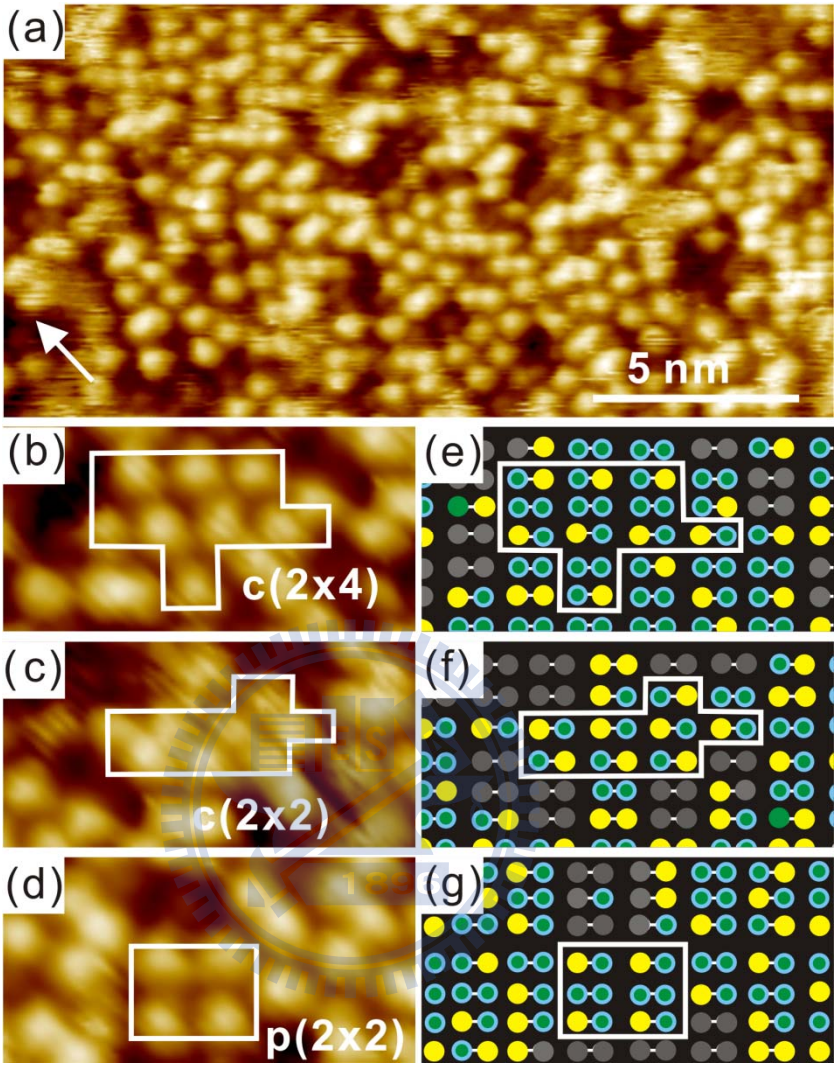

Figure 4. 6 (a) 20.0×10.0 nm^2 STM images of Si(100) after 0.6ML NaCl deposited on Si(100) at sample temperatures of 300 K. Solid boxes enclose selected area with (b) p(2×3), (c) c(2×2), and (d) p(2×2). (e)-(g) Schematic diagram of the area: yellow circles indicated dangling bond, green circles indicated adsorbed Cl, and blue circles with green circles at the center indicated that Na-Cl or Na--Cl. Sample bias voltages used were -2.05 V (a,b,c,d). The distance between two dimer rows is 7.68 Å. The white arrows indicate the dimer row direction.

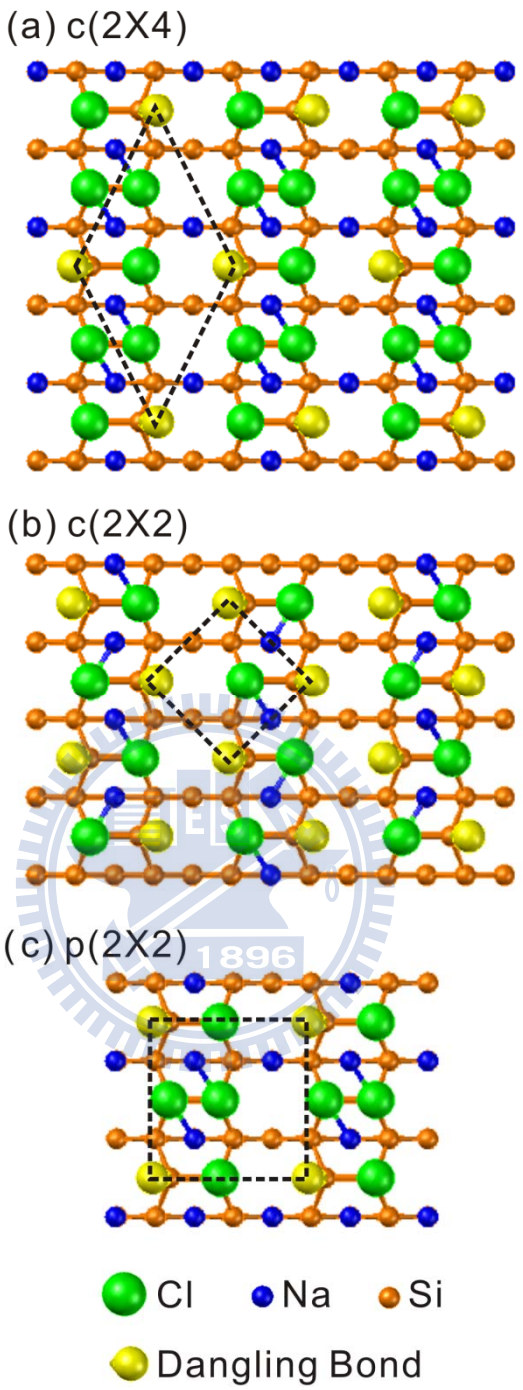

Figure 4. 7 Sphere model of the top view for fig. (b), (c), and (d). The pattern of (a) p(2×4), (b) c(2×2), and (d) p(2×2) correspond Figure 4. 6 (b), (c), and (d) respectively. The smallest (blue), middle (yellow), and largest (green) spheres in the topmost layer are Na, dangling bond, and Cl atoms, respectively. The woods notation is only considered the arrangement of the dangling bonds.

	P(2×4)	C(2×2)	P(2×2)	DB-Si-Si-Cl	DB-DB	total
DB	4%	13%	3%	13%	2%	35%
Si-Cl-Na	8%	13%	6%	6%		33%
Si-Cl--Na	4%	0%	3%	7%		14%
Pattern	16%	26%	12%	26%	2%	
Si-Cl						10%
Boundary(Si-Cl-Na)						5%
Others (Si-Cl--Na)						3%
Total						100%

Table 4. 1 the calculation of 0.65ML NaCl of the STM images.

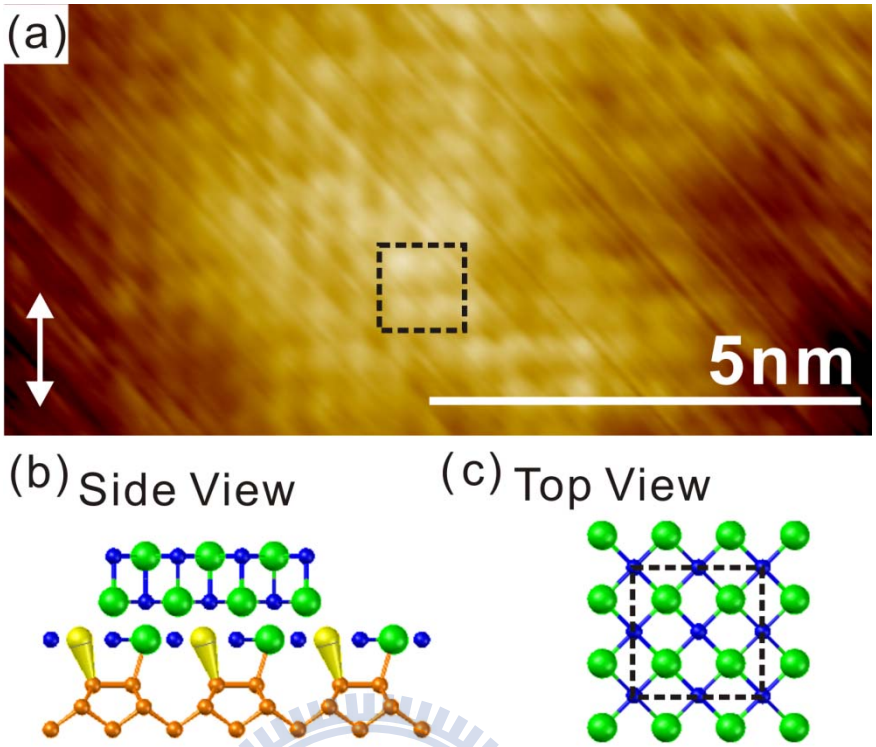

Figure 4. 8 (a) 10×5 nm^2 STM image with atomic resolution on top of an isolated island on the same surface as Figure 4. 4(c). The sample voltage was -2.8V. Atomic structure (b) side view and (c) top view.

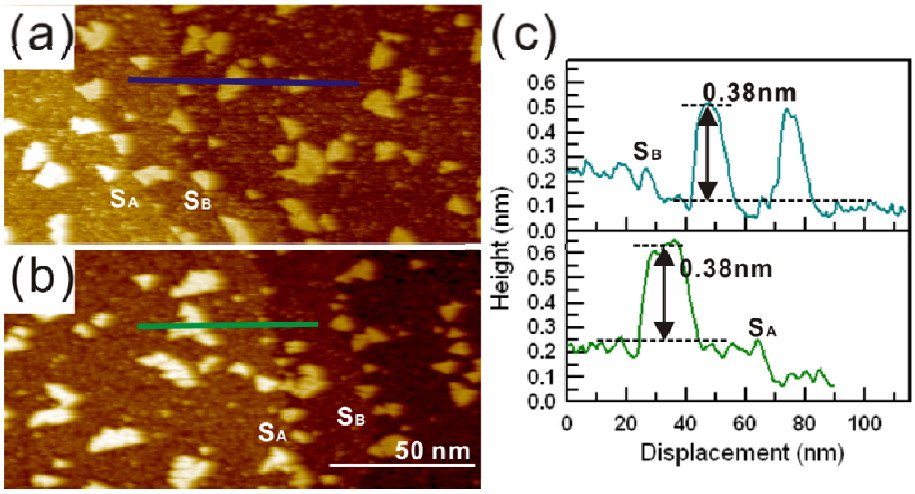

Figure 4. 9 Filled state STM topography (200×100 nm^2) with different sample bias of the 0.9 ML NaCl deposited on Si(100), I_T = 0.23 nA (a) V_s = -2.3 V and (b) V_s = -2.5 V. (c) Apparent topographic height profiles (from left) along lines marked in (a) and (b), respectively.

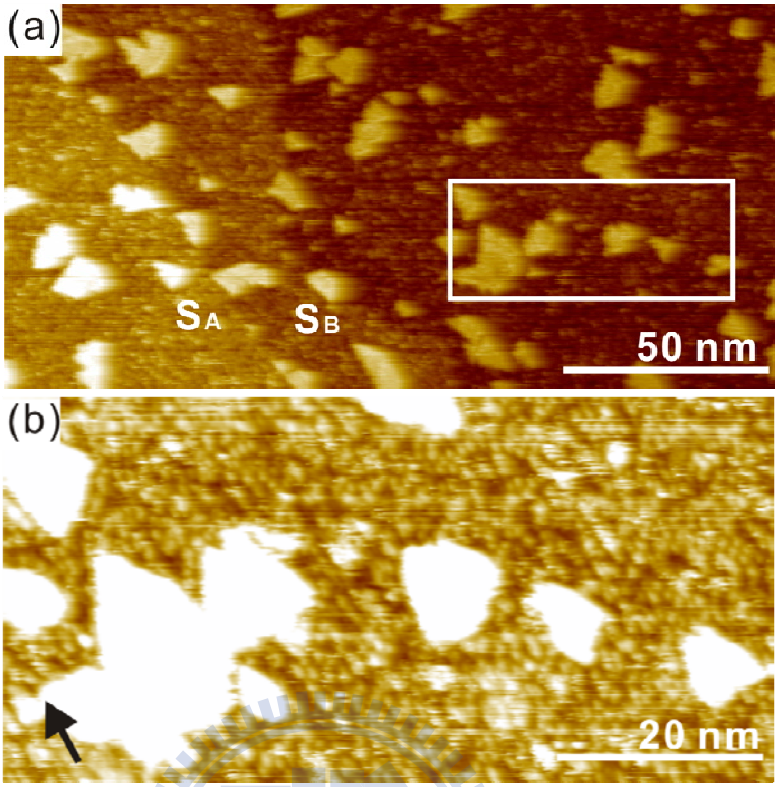

Figure 4. 10 STM images of NaCl deposited on Si(100) surface. (a) The image (200×100 nm^2) was obtained with I_T = 0.23 nA and V_s = -2.3 V at 0.9ML. (b) The zoomed-in image (80×40 nm^2) is obtained from the solid box enclose selected area in (a). In (b) beside the NaCl islands, the atomic pattern as described in Figure 4. 6 was observed.

Chapter 5 ICl and IBr on Si(100) surfaces

5. 1 Introduction

The understanding of iodochloride (ICl) gas is excellent framework for the gas-surface reaction of ICl and semiconductor surface. Adsorption of halogen and heterohalogen molecules on semiconductor surfaces has obtained much attention as model systems for chemisorption dynamic and kinetic processes. Kummel *et al.* chose to study the heterohalogen molecules of iodine monochloride (ICl) and iodine monobromide (IBr) on the Si(111)-7×7 surface and reported very different adsorption processes for the two similar systems[38, 39]. Their study shows that the adsorption of IBr is essential dissociative and that the adsorption of ICl at room temperature proceeds predominantly (I:Cl=3:1) via the least exothermic channel of iodine abstraction [38, 39]. In other words, the iodine atom in an impinging ICl molecule is selectively abstracted by the surface dangling bond to form silicon monoiodide species, Si-I, on the surface. The second atom–chlorine in ICl, is ejected back to the gas phase. The authors attribute this behavior to the fact that the HOMOs of the gas molecule are preferentially concentrated at the iodine atom. The HOMOs of IBr distribute almost evenly on the I and Br atoms and, therefore, the selectivity over I and Br is absence (I:Br = (1:1) in the absorption of IBr on the Si(111)-7 × 7.

In our present research, ICl and IBr gases are exposed on the symmetric dangling bond Si(100)-2×1 to study of the surface-gas reactions and adsorbate-adsorbate interactions. Another interesting study is about the ordering characteristic of the mixed adsorbates. For the adsorption of a similar molecule HCl on the Si(100) surface, we have found that the Cl and H adsorbates together generates many local 2×2 patterns[40]. The ordering of mixed adsorbates has been shown to due to the interaction between a dissociated fragment atom and its surrounding adsorbates.

Comparison with the adsorption of ICl or IBr on the Si(100) has also been made to clarify the role of the asymmetric molecule (ICl and IBr) bonding with the symmetric substrate (Si(100)-2×1) in adsorption dynamics. The coverage of the saturation for ICl on Si(100) only has large area pattern of c(2×2) but for IBr on Si(100) has c(2×2)-m, c(4×2)-m, c(4×2)-p, p(2×1)-m, and p(4×1)-m small areas of the local patterns.

5. 2 Experimental details

The Si(100) samples were sliced from Boron-doped wafers with a dopant concentration of approximately $1.5\times10^{15}cm^{-3}$. After outgassing at ~900 K for ~12 h, a dimerized clean Si(100) surface was obtained by dc Joule heating to ~1450 K for a few seconds.

The vapor of ICl (or IBr) was introduced from neat ICl (or IBr) liquid stored in a glass tube, which is attached to the vacuum chamber by a variable leak valve. ICl (or IBr) was purified by degassing in several freeze-pump-thaw cycles prior to use. The apparent ICl exposure, i.e., $P\times T$, is presumably proportional to the actual dosage of ICl molecules on the surfaces. The molecular ICl flux was not measured directly in the present study. Instead, the apparent exposure in Langmuir (1 L=10^{-6} Torr • s) is used as the relative measurement of ICl (or IBr) dosage on the bare Si(100)-2×1 surface.

The photoemission spectra were observed at the Taiwan Light Source laboratory in Hsinchu, Taiwan. Synchrotron radiation from a 1.5 GeV storage ring was dispersed by a wide-range spherical grating monochromator. The photocurrent from a gold mesh positioned in the synchrotron beam path was monitored to calibrate the incident photon flux. Photoelectrons were collected 15° from the surface normal and analyzed by a 125 mm hemispherical analyzer in a μ-metal shielded UHV system. The overall energy resolution was less than 120 meV. The STM measurement was performed in a separated UHV chamber.

5. 3 Results and discussion

5. 3. 1 Photoemission of ICl / Si(100)

High-resolution core level photoemission spectroscopy can be used to distinguish atoms at nonequivalent sites and in different chemical bonding configurations, according to shifts in their binding energy. Figure 5. 1(a), (b), and (c) show the respective surface-sensitive Si 2*p,* I 4*d* and, Cl 2*p* core level spectra (circles), and their decomposition into constituent components from the ICl–Si(100)-2×1 surface before and after ICl exposed at 325 K for various dosages. All fitting was least-squares fitting. Each component that consists of a pair of spin-orbit split doublets is assumed to have the same Voigt line shape.

Before ICl exposed, the Si 2*p* spectrum Figure 5. 1(a), first from bottom) has a prominent peak S at the lower (-0.52 eV) binding energy side and a visually indiscernible peak S' at the higher (+0.26 eV) binding energy side. These two components are attributed to emissions from the up atoms of asymmetric dimers and atoms in the second layer, respectively. After the ICl exposure, the spectra in Figure 5. 1(a) shows the Si 2*p* core level spectra for the ICl on Si(100) surface. This Si 2*p* spectrum consists of two components, B and C, separated by about 0.80 eV. The B component is responsible for emission from the bulk and the C component from the contribution of the surface Si-I and Si-Cl species together. As the exposure of ICl increases, the intensities of the peak S component spectra drop off.

The I 4*d* spectra in Figure 5. 1 (b) each has only one component, consisting of a pair of 1.70 eV spin-orbit-split peaks. The Cl 2*p* spectra in Figure 5. 1(c) can be analyzed with a component that consists of a pair of split doublets separated by 1.60 eV. The binding energy of these I 4*d* and Cl 2*p* spectra relative to that of the corresponding Si 2*p* remains at 99.5 eV, suggesting that the ICl atoms form similar Si-Cl and Si-I bonds. The 10L (1 L=10^{-6} Torr・s) of the exposure of ICl is saturation on the Si(100) surface.

In Figure 5. 2 X-ray photoemission spectroscopy (XPS) was used to determine the absolute ratio of Cl to I for the Si(100)-2×1 surface. The absolute ratios of Cl to I indicated that the ratio of Cl/I is about 0.95 on the Si(100) surface with various amount exposure of ICl. The I-rich Si(111) surface (Cl/I~0.3) at low coverage but a stoichiometric surface (Cl/I~1) at high coverage that is observed in the ICl/Si(111) system is not observed here. So

the XPS results suggested that the adsorption of ICl on Si(100) is no atomic selectivity and ICl is dissociative adsorption on the Si(100).

5. 3. 2 STM images of ICl on Si(100)-2×1

The initial clean Si(100) surface (not shown) forms a (2×1) reconstruction consisting of parallel rows of dimers. Each surface Si atom has one dangling bond. On the vicinal Si(100) surface, two different types of single-height steps, S_A and S_B, of height 0.15 nm separates perpendicular domains of (2 × 1) reconstruction.

Figure 5. 3 is a high-resolution empty-state STM images (20×10 nm^2) with sample bias V_S = + 2.1 V and tunneling current I_T = 0.2 nA after the ICl exposed on the Si(100)- 2×1 surface. In Figure 5. 3, the saturation of ICl on the Si(100) shows the c(2×2) atomic structure (89.4 %), Si vacancies (labeled defect) (5.4 %), and a few 2×1 atomic structure (5.2 %). Table 5. 2 shows the calculation of the pattern c(2×2), 2×1, and defect.

In Figure 5. 3, the saturation ICl has a well ordered structure c(2×2) on Si(100) surface and the atomic structure is shown in Figure 5. 4. Since the ratio of the Cl to I coverage is roughly 1：1 (Cl/I~0.95 discussed in section 5. 3. 1), in Figure 5. 4(c) on the one dimer raw zigzag structure chain is an ordered array of Cl-Si-Si-I, in which Cl-sites and I-sites in neighboring dimers are anti-phase with each other. The c(2×2) structure can be regarded as a combination of more than two neighboring zigzag Cl-Si-Si-I chains. According the simulated STM images for ICl/Si(100) (discussed in 5. 3. 3), for the empty states of the simulated STM images the protrusions of Si-I is brighter than Si-Cl at V_S > +2.4 V which is corresponded to the empty state STM images. And the XPS (in section 5. 3. 1) results indicated that the ratio of Cl / I is 0.95 which is agreed with the calculation of the ratio of Cl/I~0.9 in STM image (shown in Table 5. 2) at the saturation of the ICl on Si(100). Therefore, in the c(2×2) structure as shown in Figure 5. 4(a), the brighter protrusions can be regarded as Si-I and the darker sites can be regarded as Si-Cl.

The XPS results (in section 5. 3. 1) indicated that the ICl is no atomic selection and Cl/I is about 1, suggesting that ICl is dissociative adsorption (Cl : I~1 : 1) on the Si(100) surface for the various coverage of ICl. And the ab-initio radius difference between I (1.27 Å) of Si-I and Cl (0.89 Å) of Si-Cl is large. Therefore, in order to have the lowest surface energy for ICl/Si(100), the STM results revealed that Si-I and Si-Cl atoms have to alternately arrange to form a large areas c(2×2), suggesting that I-Si-Si-Cl has the lowest electron overlap.

In Figure 5. 3, the 2×1 structure (5.2 %) can be observed. The atoms in the 2×1 structure are the same as bright as the Si-I in the area of c(2×2) and the XPS results(in section 5. 3. 1) indicated that I atoms is more than Cl atoms by 5%., so the atoms in the area of 2×1 is suggested consisting of I-Si-Si-I. In Figure 5. 3, some darkest area also can be observed. Dimer vacancies, where both Si dimer atoms are missing, appear as dark features spanning the full width of the dimer row, and the single Si-atom vacancies are imaged as small dark features half the width of the dimer row. So in Figure 5. 3 the darkest area can be regarded as the dimer vacancies or single Si-atom vacancies.

5. 3. 3 STM simulation of ICl/Si(100)

According to the Tersoff-Hamann approximation, the tunneling current in STM is proportional to the local density of states (LDOS) near the Fermi level at the position of the tip. To account for the STM tunneling current, we integrate the LDOS between the sample bias and the Fermi energy level. The partial density:

$$\rho^{\mathrm{STM}}(r) = \int_{E_F+eV_S}^{E_F} dE \sum_{n\mathbf{k}} \left|\Psi_{n\mathbf{k}}(\mathbf{r})\right|^2 \delta(E-\varepsilon_{n\mathbf{k}})$$

should reflect the STM tunneling currents. Figure 5. 5 shows the simulated empty-state STM images above the top ICl layer by 1.5 Å at various sample voltages for the saturation ICl on Si(100). Figure 5. 5 (a), (b), and (c) display c(2×2) images for V*s* > +2.0 V. The c(2×2) structure is consistent with the experimental STM images as shown in Figure 5. 4 (a). It also reveals that the bright protrusions of the empty-state STM image at the sample bias of V*s* = +2.1 V should be assigned to the I atoms.

5. 3. 4 Photoemission of IBr / Si (100)

High-resolution core level photoemission spectroscopy can be used to distinguish atoms at nonequivalent sites and in different chemical bonding configurations, according to shifts in their binding energy. Figure 5. 6 (a), (b), and (c) show the respective surface-sensitive Si 2*p,* I 4*d* and, Br 3*d* core level spectra (circles), and their decomposition into constituent components from the IBr–Si(100)-2×1 surface before and after IBr exposed at 325 K for various dosages. All fitting was least-squares fitting. Each component that consists of a pair of spin-orbit split doublets is assumed to have the same Voigt line shape.

Before IBr exposed, the Si 2*p* spectrum Figure 5. 6 (a), first from bottom) has a prominent peak S at the lower (-0.52 eV) binding energy side and a visually indiscernible peak S' at the higher (+0.26 eV) binding energy side. These two components are attributed to emissions from the up atoms of asymmetric dimers and atoms in the second layer, respectively. After the IBr exposure, the spectra in Figure 5. 6 (a) shows the Si 2*p* core level spectra for the IBr on Si(100) surface. Upon IBr adsorption the peak S decrease with the various amounts of IBr and a chemically shifted shoulder develops on the high binding energy side. For the fitted Si spectrum from the saturated surface (10 L), this Si 2*p* spectrum consists of two components, B and C, separated by about 0.72 eV. The B component is responsible for emission from the bulk and the C component from the contribution of the surface Si-I and Si-Br species together. As the exposure of IBr increases, the intensities of the peak S component spectra decreased with the amount of the exposure IBr.

The I 4*d* spectra in Figure 5. 6 (b) each has only one component, consisting of a pair of 1.70 eV spin-orbit-split peaks. The Br 3*d* spectra in Figure 5. 6 (c) can be analyzed with a component that consists of a pair of split doublets separated by 1.0 eV. The binding energy of these I 4*d* and Br 3*d* spectra relative to that of the corresponding Si 2*p* remains at 99.5 eV, suggesting that the IBr atoms form similar Si-I and Si-Br bonds. The 10L of the exposure of IBr is saturation on the Si(100) surface.

In Figure 5. 2 the absolute ratios of Br to I indicated that the ratio of Br/I is about 0.85 on the Si(100) surface with various amount exposure of IBr. In contrast to ICl/Si(111)-7×7 and IBr/Si(111)-7×7[38, 39], their study shows that the adsorption of IBr is dissociative and

that the adsorption of ICl at room temperature proceeds predominantly (I:Cl=3:1) at low coverages via the least exothermic channel of iodine abstraction [38, 39]. The I-rich Si(111) surface (Cl/I~0.3) at low coverage but a stoichiometric surface (Cl/I~1) at high coverage that is observed in the ICl/Si(111) system is not observed here. The adsorption of IBr on Si(100) is no apparently atomic selectivity is presented and the IBr dissociative adsorption on the Si(100) surface because the Br/I is about 0.85 which is similar the results of IBr/Si(111) with the various exposure of IBr.

5. 3. 5 STM images of IBr on Si(100)-2×1

The initial clean Si(100) surface (not shown) forms a (2×1) reconstruction consisting of parallel rows of dimers. Each surface Si atom has one dangling bond. On the vicinal Si(100) surface, two different types of single-height steps, S_A and S_B, of height 0.15 nm separates perpendicular domains of (2 × 1) reconstruction.

Figure 5. 7 is a high-resolution empty-state STM images (20×10 nm^2) with sample bias V*s* = + 2.4 V and tunneling current I_T = 0.2 nA after the IBr exposed on the Si(100)- 2×1 surface. In Figure 5. 7 the protrusion spots are presented on the Si(100) surface after the exposure of IBr. The protrusions have local pattern as shown in solid boxes enclose selected areas of Figure 5. 7 (b) p(2×1)-m and p(4×1)-m, Figure 5. 7(c) c(4×2)-p and c(4×2)-m, and Figure 5. 7(d) c(2×2)-m. According to the empty-state of the simulated STM image as shown in Figure 5. 10, the brighter protrusions of Si-I is brighter than Si-Br at V*s* > +2.0 eV which is corresponded to the bias voltage V*s*= + 2.4 V (empty state) of the experimental STM image. Therefore, the brighter protrusions indicated the Si-I and the dimmer sites indicate Si-Br in the empty state of the saturation of IBr/Si(100) STM images. The sphere models of c(2×2)-m and c(4×2)-m are shown in Figure 5. 8 and Figure 5. 9, respectively.

5. 3. 6 STM simulation of IBr/Si(100)

According to the Tersoff-Hamann approximation, the tunneling current in STM is proportional to the local density of states (LDOS) near the Fermi level at the position of the tip. To account for the STM tunneling current, we integrate the LDOS between the sample bias and the Fermi energy level. The partial density:

$$\rho^{\mathrm{STM}}(r) = \int_{E_F+eV_S}^{E_F} dE \sum_{n\mathbf{k}} \left|\Psi_{n\mathbf{k}}(\mathbf{r})\right|^2 \delta(E-\varepsilon_{n\mathbf{k}})$$

should reflect the STM tunneling currents. Figure 5. 10 shows the simulated empty-state STM images above the top IBr layer by 1.5 Å at various sample voltages for the saturation IBr on Si(100). Figure 5. 10 displays c(2×2) images for V*s* > +2.0 V. The c(2×2) structure is consistent with the experimental STM images as shown in Figure 5. 7 (d). It also reveals that the bright protrusions of the empty-state STM image at the sample bias of V*s* = +2.4 V should be assigned to the I atoms.

5. 4 Conclusions

In contract to ICl and IBr on Si(100)-2×1, the XPS results indicated that the majority adsorption of ICl (Cl/I~0.95) and IBr (Br/I~0.85) are both dissociated adsorption on the Si(100) surface and no apparent atomic selection adsorption with the various exposure amount of ICl or IBr. Because for the Si(100)-2×1 the two Si atoms on the same dimer has the nearest dangling bond being 2.40 Å and the bond length of the two dangling bond for Si(100) is close to the bond length of the ICl (2.32 Å) and IBr (2.49 Å), the ICl (or IBr) can adsorbate together easily to form Si-I and Si-Cl (or Si-I and Si-Br) on the Si(100) surface.

For ICl/Si(100) STM images allow to distinguish between I and Cl adsorbates and reveal that the co-adsorbed I and Cl atoms form a large areas of c(2×2) structure on Si(100) surface at room temperature. For IBr/Si(100), STM images reveal that the co-adsorbed I and Br atoms just form a small local areas of c(2×2)-m, c(4×2)-m, c(4×2)-p, p(2×1)-m, and p(4×1)-m structure on Si(100) surface at room temperature.

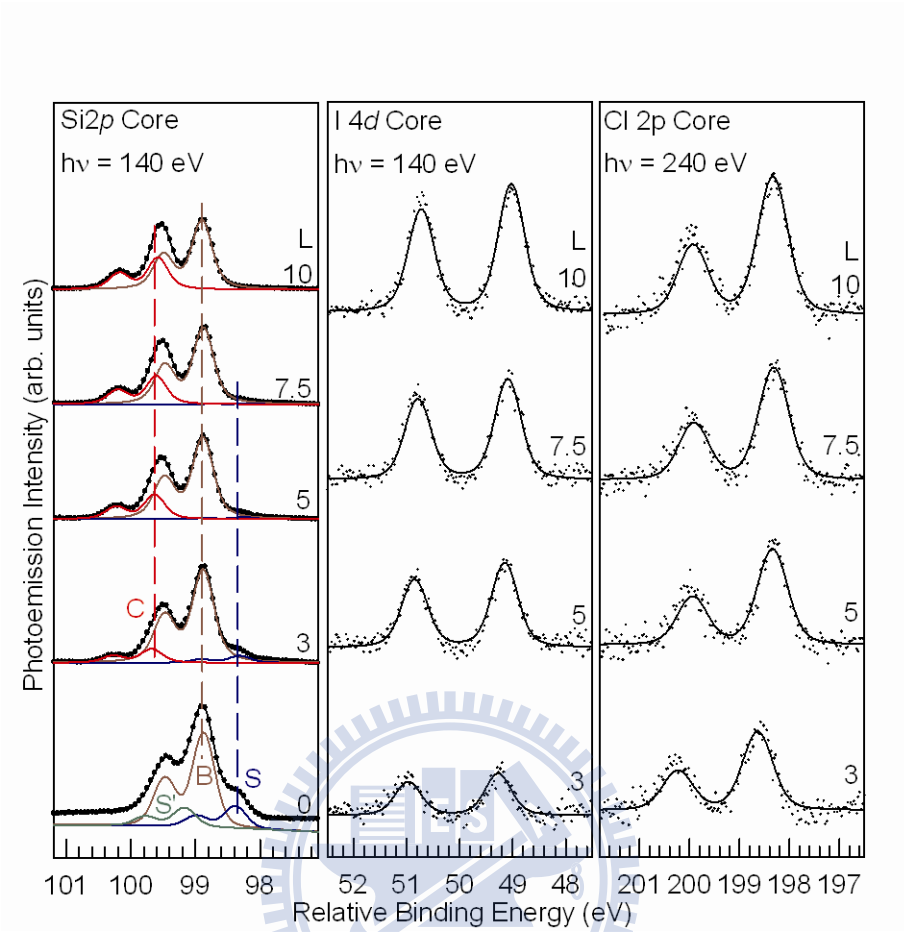

Figure 5. 1 (a) Si 2*p* and (b) I 4*d* (c) Cl 2*p* core level photoemission spectra (circles) of ICl–Si(100)-2×1 surface and Si(100) surface with various amounts of exposed ICl, as labeled. The solid curves are fits to the spectra. The curves labeled B, S, S', and C are the results of decomposition of the Si 2*p* spectra into contributions from the bulk, the clean surface, and the Si–ICl species, respectively. The apparent exposure in Langmuir (1 L=10^{-6} Torr • s) is used as the relative measurement of ICl dosage on the bare Si(100)-2×1 surface.

	$\triangle_{SO}$	W_G (eV)	W_L (eV)	Component	$\triangle E_i$ (eV)
Si 2*p*	0.60	0.38	0.20	S	-0.52
			0.20	C	+0.8
			0.20	S'	+0.26
I 4*d*	1.70	0.46	0.20		
Cl 2*p*	1.60	0.68	0.20		

Table 5. 1 Fitting parameters from the analysis of the Si 2*p*, I 4*d*, and Cl 2*p*. In all spectra we obtained the best fit using a spin-orbit split ($\triangle_{SO}$). W_L is Lorenzian full width at half maximum. $\triangle E_i$ is the shift of the peak with respect to the bulk binding energy, and W_G is the Gaussian width and width.

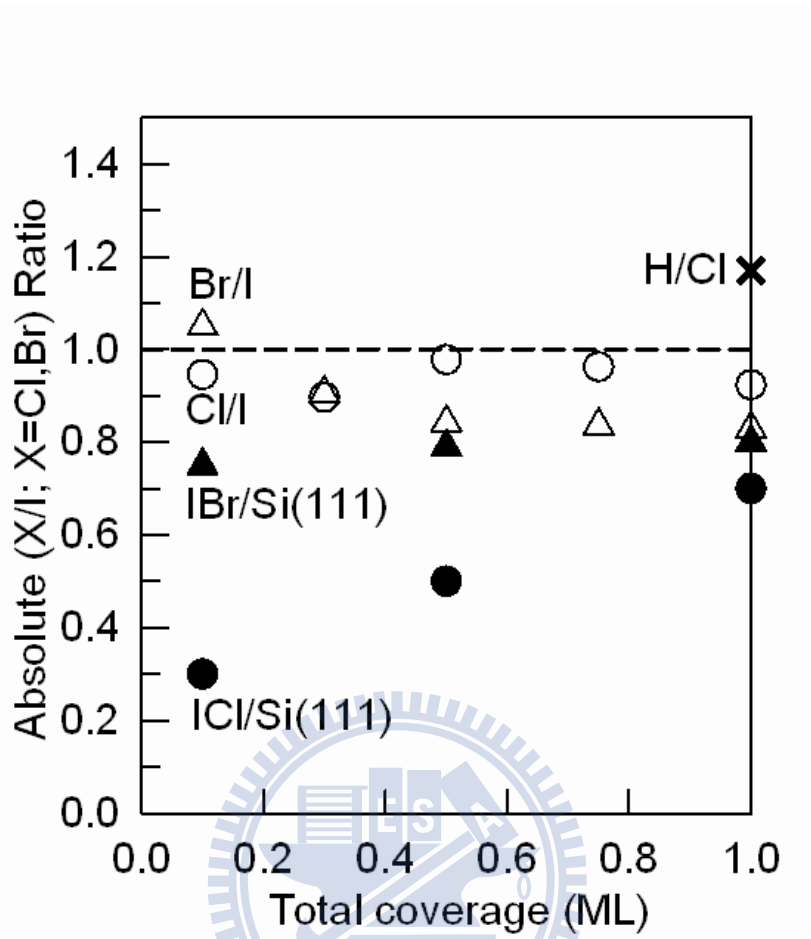

Figure 5. 2 Plot of the ratio between Cl 2*p*, Br 3*d*, and I 4*d* core-level peak intensities as a function of ICl and IBr dose. The dada of ICl/Si(111) is from [39], IBr/Si(111) is from [38], and HCl/Si(100) is from [40].

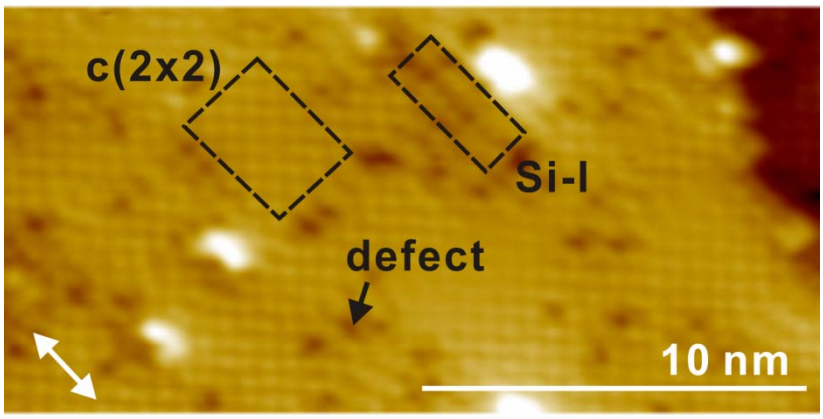

Figure 5. 3 The (20×10 nm^2) STM images of Si(100) after saturation dosage of ICl at room temperature. The image is obtained at room temperature with I_T = 0.2 nA and V_S = +2.1 V. The bright spots are I atoms, dim spots are Cl atoms, and darkest spots are defect. The white arrows indicate the dimer-row directions in the top Si layer.

structure	(%)
C(2×2)	89.4
Si-I (2×1)	5.2
Defect and impurity	5.4
Cl / I	0.9

Table 5. 2 The calculation of Si(100) after saturation dosage of ICl at room temperature from the Figure 5. 3.

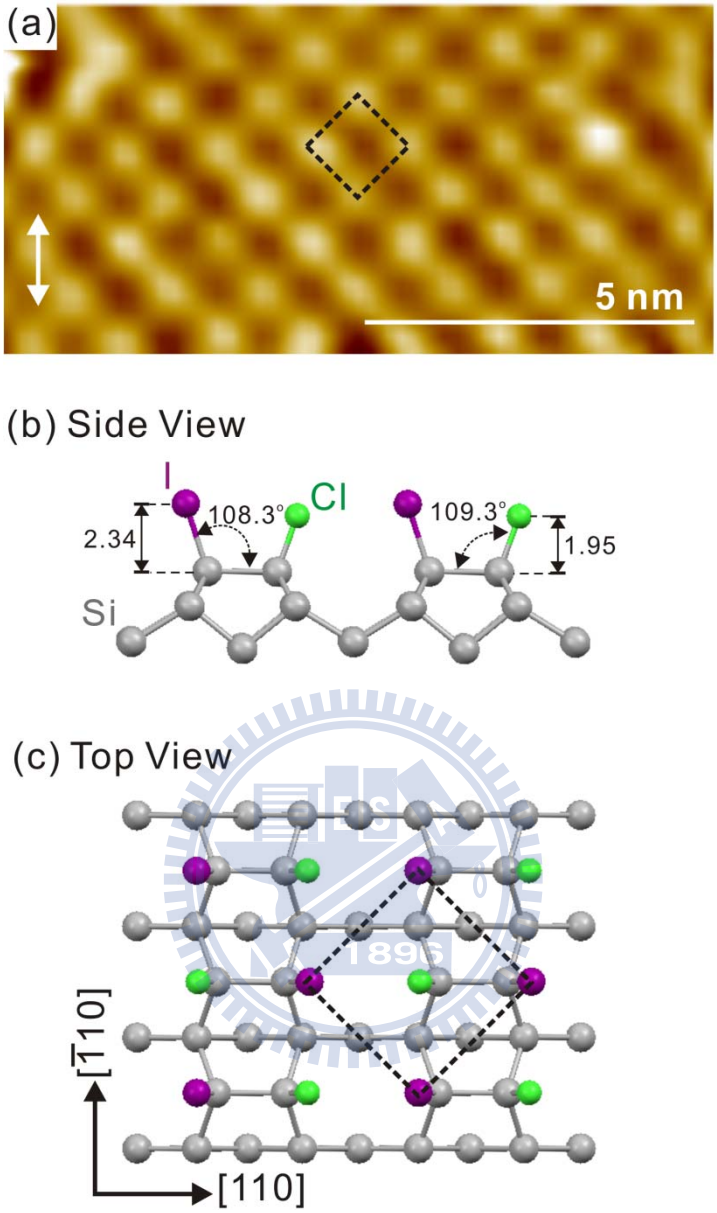

Figure 5. 4 (a) Close-up image of c(2×2) structure extracted from Figure 5. 3 dash square denotes unit cell. (b) (-110) projection of atomic model of c(2×2) structure. (c) Top view. Orange, green, and purple circles represent Si, Cl, and I atoms, respectively. According the ab-initio calculation, the bonding lengths of Si-I, Si-Cl are 2.47 Å and 2.07 Å, respectively. The ab-initio radius of I and Cl are 1.27 Å and 0.89 Å.

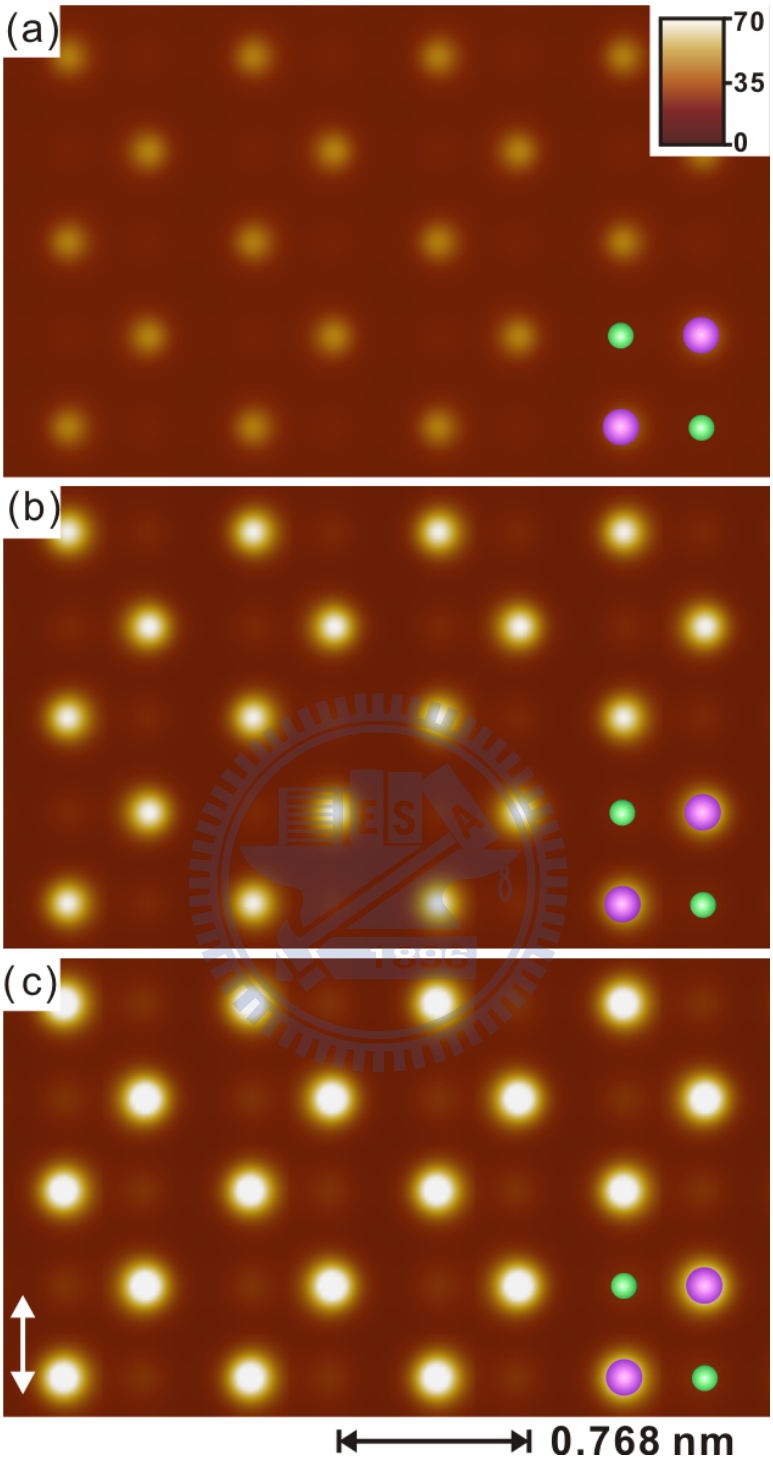

Figure 5. 5 For c(2×2) the empty states of the simulation STM images for the saturation ICl on Si(100) surface above the top ICl overlayer by 1.5 Å with different sample bias at (a) +2.0 V, (b) +2.5 V, and (c) +3.0 V.

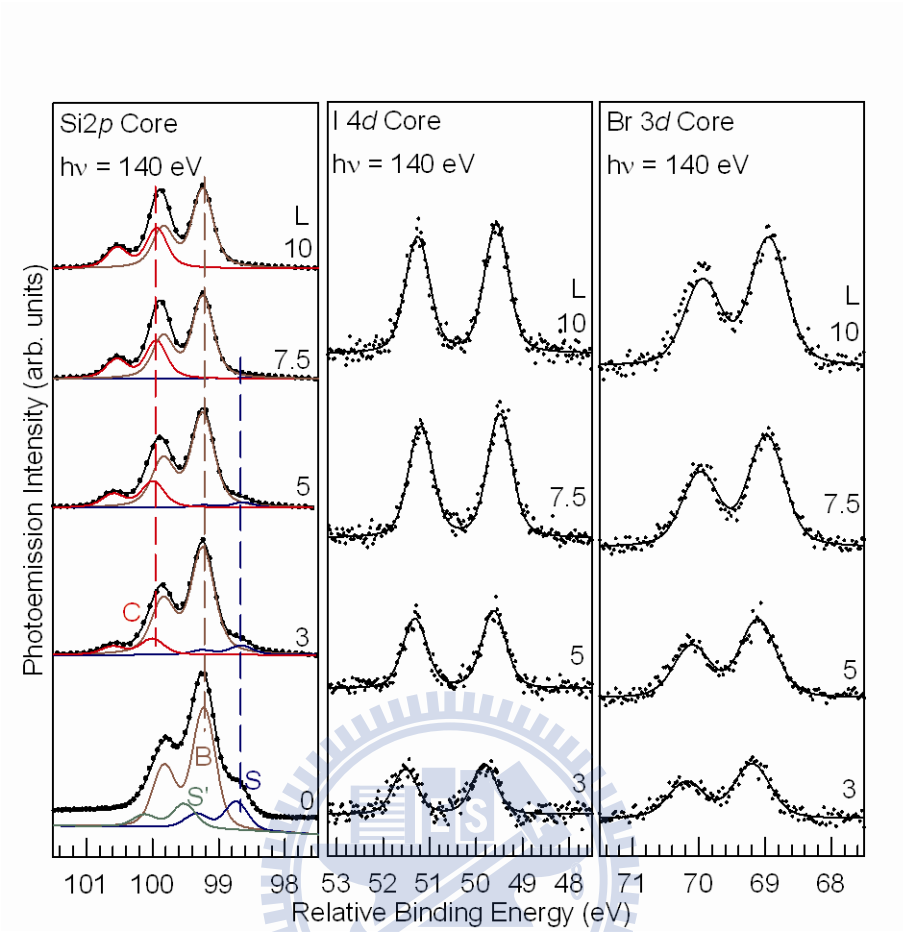

Figure 5. 6 IBr on Si(100) (a) Si 2*p* and (b) I 4*d* (c) Br 3*d* core level photoemission spectra (circles) of IBr–Si(100)-2×1 surface and Si(100) surface with various amounts of exposed IBr, as labeled. The solid curves are fits to the spectra. The curves labeled B, S, S', and C are the results of decomposition of the Si 2*p* spectra into contributions from the bulk, the clean surface, and the Si–IBr species, respectively.

	$\triangle_{SO}$	W_G (eV)	W_L (eV)	Component	$\triangle E_i$ (eV)
Si 2*p*	0.60	0.36	0.20	S	-0.52
				C	0.72
				S'	+0.26
I 4*d*	1.70	0.43	0.20		
Br 3*d*	1.00	0.53	0.20		

Table 5. 3 Fitting parameters from the analysis of the Si 2*p*, I 4*d*, and Br 3*d*. In all spectra we obtained the best fit using a spin-orbit split (Δ_{SO}). W_L is Lorenzian full width at half maximum. ΔE_i is the shift of the peak with respect to the bulk binding energy, and W_G is the Gaussian width and width.

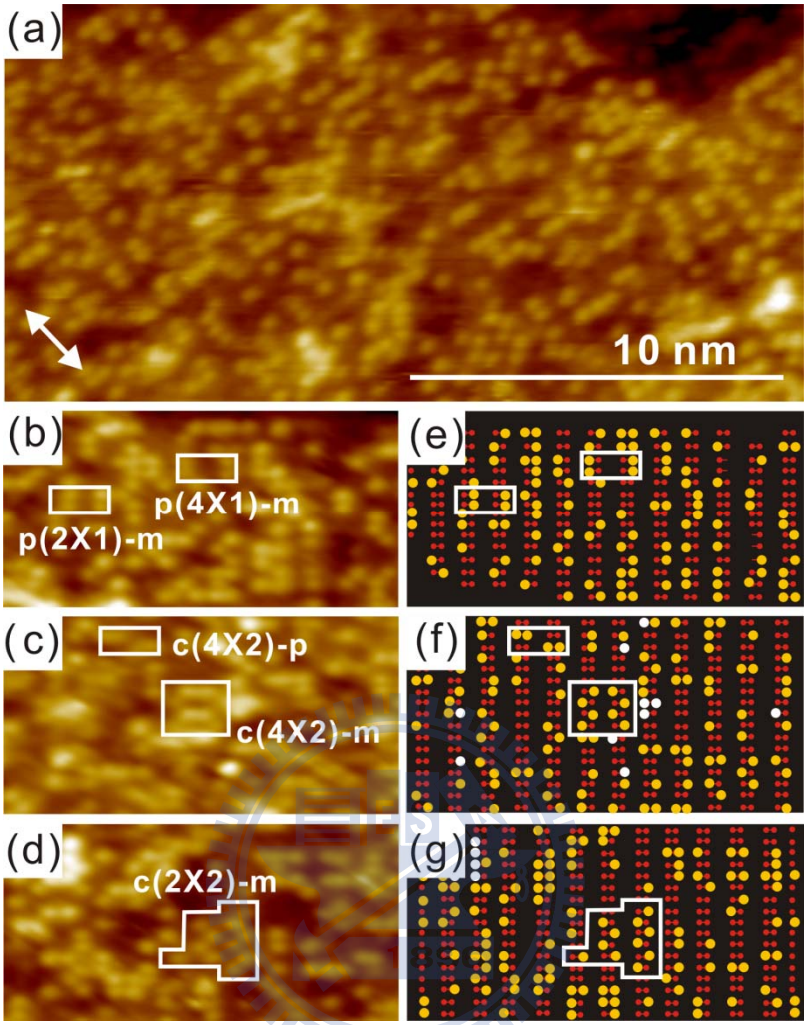

Figure 5. 7 (a) 20.0 × 10.0 nm^2 STM images of Si(100) after saturation dosage of IBr at sample temperatures of 300 K. Solid boxes enclose selected area with (b) p(4 ×1)-m, p(2×1)-m, (c) c(4×2)-p, c(4×2)-m, and (d) c(2×2)-m. (e)-(g) Schematic diagram of the area: Large yellow circles indicated adsorbed Br, small red circles indicated adsorbed I, and white circles indicated dangling bonds. Sample bias voltages used were + 2.4 V (a,b,c,d). The distance between two dimer row is 7.68 Å.

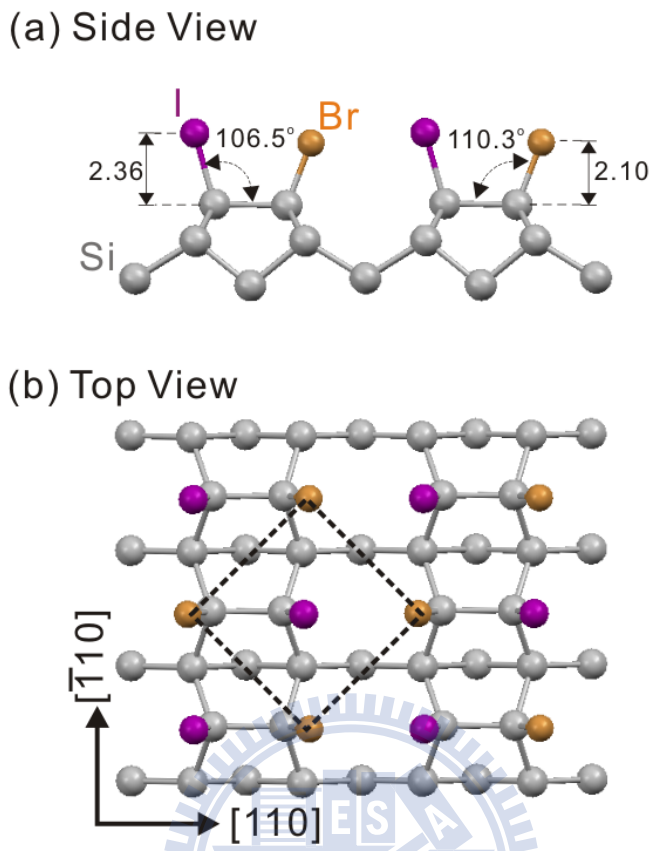

Figure 5. 8 Sphere model for the Figure 5. 7 (d). (a) Side view. (b)Depiction of mixed Iodide- and Bromide-bonded Si(100)-c(2×2) where pairs of IBr alternate along and across the dimer rows. The rhombus shows the periodic boundary of the primitive cell. According the ab-initio calculation, the bonding lengths of Si-I, Si-Br are 2.47 Å and 2.24 Å, respectively. The ab-initio radius of I and Br are 1.27 Å and 1.06 Å.

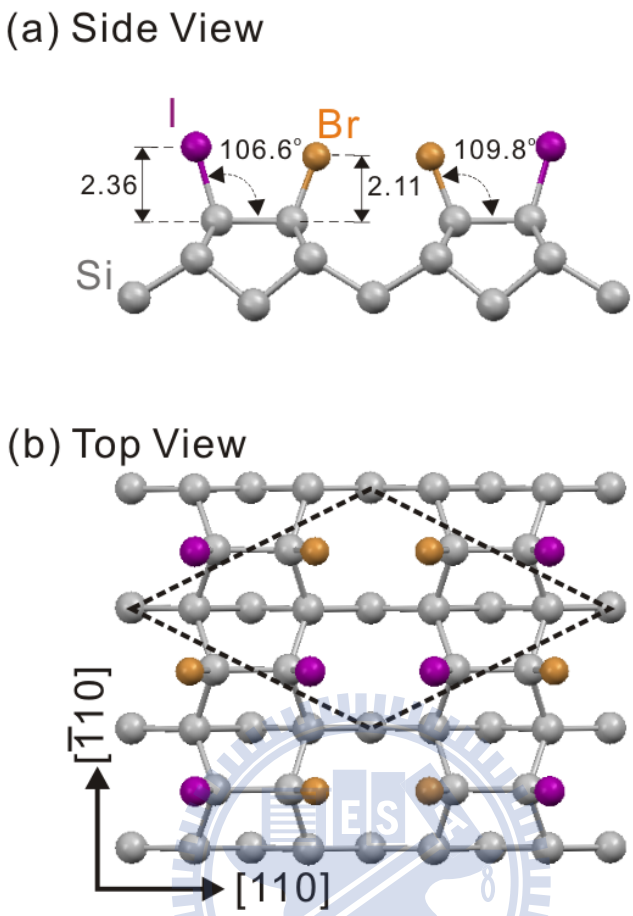

Figure 5. 9 Sphere model for the Figure 5. 7 (c). (a) Side view. (b)Depiction of mixed Iodide- and Bromide-bonded Si(100)-c(4×2) where pairs of IBr alternate along and across the dimer rows. The rhombus shows the periodic boundary of the primitive cell.

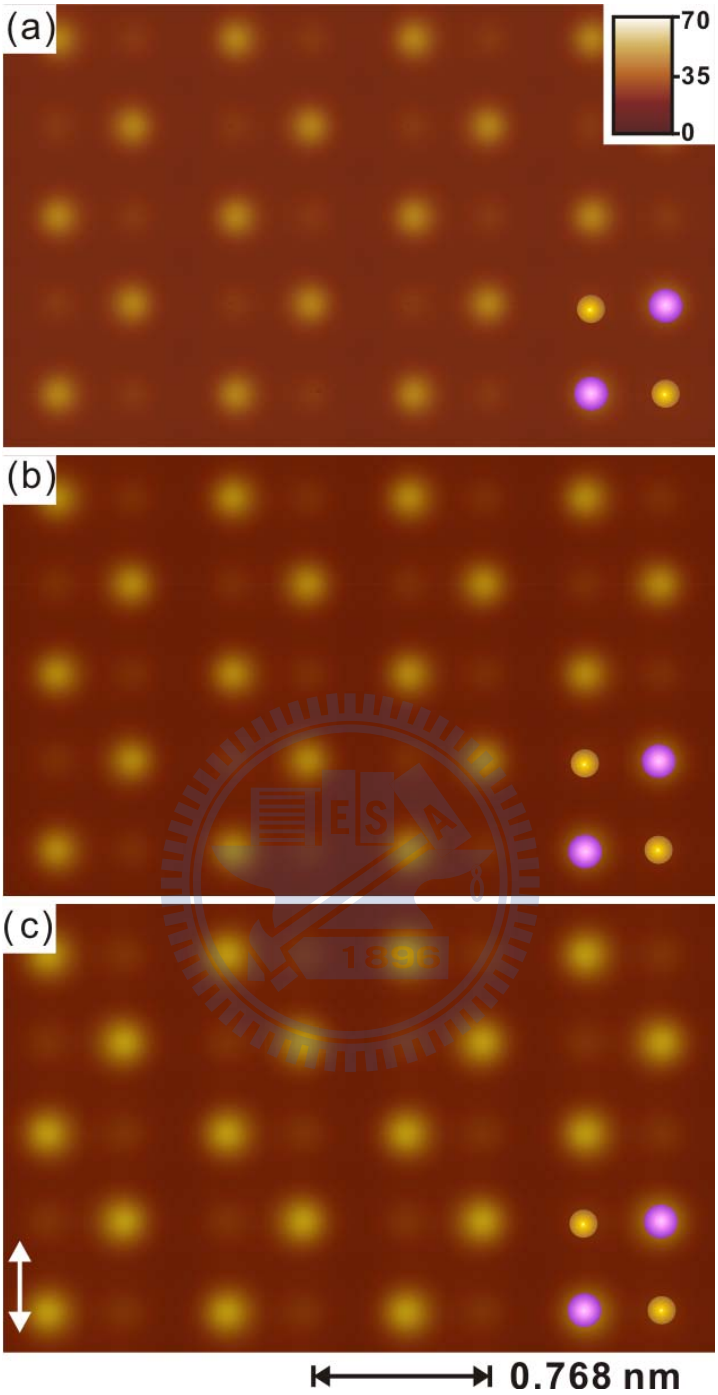

Figure 5. 10 For c(2×2) of the empty states of the simulation STM images for the saturation IBr on Si(100) surface above the top IBr overlayer by 1.5 Å with different sample bias at (a) +2.0 V, (b) +2.5 V, and (c) +3.0 V.

Chapter 6 Conclusions

We have studied the growth of ionic crystal and inter-halogen molecules including NaCl, KCl, ICl, and IBr on the Si(100)-2×1 surface at room temperature by synchrotron x-ray core level photoelectron spectroscopy, scanning tunneling microscopy, and *ab initio* calculations.

In the growth of KCl/Si(100), at low coverage, some KCl molecules dissociate. Above 0.3 ML, adsorbed KCl precipitates in clusters. At about 1 ML coverage, most surface area is covered by regular clusters (Cluster A) that produce a c(4×4) ordered surface structure. *Ab initio* calculations support a novel four-sided pyramidal model for the first KCl monolayer. Between 1 and 2 ML, further adsorbed KCl coalesces into regular clusters of the second kind (Cluster B). The atomic structure of Clusters B was not resolved. Above 2 ML, pseudo-two-dimensional growth occurs, while the monoatomic steps on the Si(100) substrate advance through the growing films.

In the growth of NaCl/Si(100), as $\theta < 0.6$ ML the XPS and STM results together indicated that the partial NaCl dissociated, and the rest adsorbed NaCl bonded with Si atoms to form Si-Cl-Na species. At $\theta = 0.65$ ML, the residual dangling bonds of the Si have c(2×4), c(2×2), and p(2×2) ordered structure due to the arrangement of Si-Cl-Na, dissociated Na and Cl, and dangling bonds. Between 0.65 and 2.25 ML, the double layer islands of NaCl grew on top of the Na,Cl, and NaCl mixed ad-layer. And the XPS results indicated that the residual dangling bonds of the first layer is still under the second NaCl layer and the amounts of the residual dangling bonds are not decreased above $\theta > 0.6$ML. The atomic resolution of STM images revealed that the doubled layer islands of NaCl have the well-defined protrusion which has a lattice constant of the square lattice of 3.82 Å.

In contract to ICl and IBr on Si(100)-2×1, the XPS results indicated that the majority adsorption of ICl (Cl/I~0.95) and IBr (Br/I~0.85) are both dissociated adsorption on the Si(100) surface and no apparent atomic selection adsorption with the various exposure amount of ICl or IBr. Because for the Si(100)-2×1 the two Si atoms on the same dimer has the nearest dangling bond being 2.40 Å and the bond length of the two dangling bond for Si(100) is close to the bond length of the ICl (2.32 Å) and IBr (2.49 Å), the ICl (or IBr) can adsorbate together easily to form Si-I and Si-Cl (or Si-I and Si-Br) on the Si(100) surface.

ICl/Si(100) STM images allowed to distinguish between I and Cl adsorbates, and revealed that the co-adsorbed I and Cl atoms form a large areas of c(2×2) structure on Si(100) surface at room temperature. For IBr/Si(100), STM images revealed that the co-adsorbed I and Br atoms just form a small local areas of c(2×2)-m, c(4×2)-m, c(4×2)-p, p(2×1)-m, and p(4×1)-m structure on Si(100) surface at room temperature.

Appendix A In-situ study of the catalytic oxidation of CO on a Pt(110) surface using ambient pressure X-ray photoelectron spectroscopy

CO and O_2 co-adsorption and the catalytic oxidation of CO on a Pt(110) surface under various pressures of CO and O_2 (up to 250 mTorr) are studied using ambient pressure X-ray photoelectron spectroscopy (APXPS) and mass spectrometry. There is no surface oxide formation on Pt under our reaction conditions. CO oxidation in this pressure (<500 mTorr), O_2 to CO ratio (<10), and temperature (150℃) regime is consistent with the Langmuir-Hinshelwood reaction mechanism. Our findings provide in-situ surface chemical composition data of the catalytic oxidation of CO on Pt(110) at total pressures below 1 Torr.

A. 1 Introduction

The formation of oxides on transition metal surfaces has been actively studied because of its importance in understanding heterogeneous catalytic reactions on metal surfaces [41]. Many high vacuum (<10^{-6} Torr) surface science techniques are used to explore the mechanism and kinetics of oxidation and heterogeneous catalysis on model surfaces. It has been shown that low pressure results can often be extrapolated across a wide pressure range [42]; however, there are also cases in which such an extrapolation is not valid. Recently, the development of in-situ surface science techniques, such as synchrotron based ambient pressure X-ray photoelectron spectroscopy (APXPS) [43-45], high pressure scanning tunneling microscopy (HP-STM) [46, 47], surface X-ray diffraction [48], sum frequency generation spectroscopy [49] and other optical imaging techniques, has rejuvenated research in this field. In particular, the study of surface oxides on Pt(110) [47, 48] has received much attention due to its unique oscillatory behavior of surface morphology under CO oxidation reaction conditions. Hendriksen and Frenken [47], using a combined HP-STM and mass spectrometer, demonstrated the existence of roughening of the Pt(110) surface during CO oxidation at 425 K, pressures near 0.5 bar and an O_2/CO ratio >45. The formation of surface roughening, assumed to be Pt oxide, is observed when the reaction rate is enhanced. Later, Ackermann et al. [48], using high pressure X-ray diffraction and density functional theory (DFT) model calculation, proposed that the surface oxide formed on the

Pt(110) is stabilized by carbonate species. One important conclusion drawn from these studies is that CO oxidation under high pressure (~1 bar) and at a high O_2/CO ratio may follow the Mars-Van Krevelen mechanism rather than the Langmuir-Hinshelwood (L-H) mechanism [50]. Furthermore, the characteristics of Pt oxide were investigated with DFT calculations under elevated pressure. Wang et al. [51] reported the importance of a phase boundary between metal and gas during CO oxidation. It was determined that the surface oxides provide lower activation barriers for the CO redox process, which favors the Mars-Van Krevelen mechanism under highly reactive conditions.

In this letter, we study the catalytic oxidation of CO on a Pt(110) surface under various pressures of CO and O_2 gases (10-250 mTorr) at 150-200 ℃ using APXPS, a technique which is sensitive to the chemical state of platinum surface atoms and surface adsorbates. We find that chemisorbed oxygen is not stable under these reaction conditions and is removed immediately from the surface in the presence of CO. There is no surface oxide formation on Pt under our reaction conditions. CO oxidation in this pressure (<500 mTorr), O_2/CO ratio (<10), and temperature (~150 ℃) regime follows the L-H reaction mechanism. Our findings provide in-situ surface chemical composition data of the catalytic oxidation of CO on Pt(110) at our reaction conditions.

A. 2 Experiment Details

APXPS experiments were performed at Beamline 9.3.2 at the advanced light source. The apparatus [43] consists of two connected vacuum chambers: one for sample preparation and one for analysis. A Pt(110) single crystal from Matek, polished on both sides, was used in this study. After repeated cycles of Ar^+ sputtering and oxygen annealing, and a final annealing above 750 ℃ in vacuum in the sample preparation chamber, the sample was transferred in vacuum to the high pressure cell in the analysis chamber. The sample surface was checked with XPS to confirm the absence of contaminants. The (2×1) reconstruction of the surface was observed with low energy electron diffraction (LEED) and STM in a separate UHV system after identical sample preparation.

The design of the spectrometer consists of a chamber with a differentially pumped electrostatic lens system that focuses the electrons emitted from the sample onto the focal plane of a hemispherical PHI-360 SCA electron energy analyzer [43, 45]. Photoelectron spectra of the C1*s*, O1*s* and Pt4*f* core levels were recorded at photon energies of 540, 800 and 340 eV, respectively, corresponding to approximately the same photoelectron kinetic energy (~270 eV) to ensure the same probe depth.

CO (Air Gas, UHP) and O_2 (Air Gas, UHP) are connected to a gas manifold via UHV leak valves. The gases are premixed in the manifold and delivered to the high pressure cell through a vacuum gate valve. Calibrated Baratron and Convectron gauges are used to monitor the total pressures inside of the high pressure cell and the gas manifold, respectively. During the reaction, we use XPS to determine the chemical composition of the Pt(110) surface. Simultaneously, we monitor the reactivity using an Ametek Dycor LC100 residual gas analyzer (RGA). The RGA is attached to the 2nd differential pumping stage behind the front nozzle [43]. RGA signals are proportional to the gas pressures in the high pressure cell; thus we can calibrate the RGA signals with the Baratron readings in the high pressure cell to obtain the partial pressure of each gas.

A. 3 Results and discussion

Figure A. 1 shows the C1*s*, O1*s* and Pt4*f* spectra of the Pt(110) surface under different CO and O_2 pressures and at different temperatures. We analyze each core level using different photon energies to ensure the same surface sensitivity. When 200 mTorr CO was added to the high pressure cell, a broad peak that can be de-convoluted into two peaks appeared in the C1*s* spectrum (Spectrum A) with binding energies of 286.0±0.1 and 286.7±0.1 eV. And two distinct peaks appeared in the O1*s* spectrum (Spectrum A), with binding energies of 531.0±0.1 and 532.7±0.1 eV. We assigned these peaks to CO molecules adsorbed on bridge sites and on-top sites, respectively. These binding energies are in good agreement with CO adsorption experiments under UHV conditions [52]. The Pt4*f* peak of the CO covered surface is broader compared to the clean Pt surface due to CO adsorption. Upon addition of 200 mTorr O_2, the population of CO on bridge sites decreased (Figure A. 1, Spectra B). The area ratio between on-top and bridge sites changed from 2.5:1 to 3.1:1 without the appearance of additional peaks. This is consistent with asymmetric inhibition of CO and O_2 on Pt(110) [53]. The sample was subsequently heated to 150 ℃ under the same CO and O_2 pressure. Most bridge site CO molecules were removed above 100 ℃ and only ontop CO remained (Spectra c). Upon further heating, CO_2 was first detected at 120℃. At 150 ℃, the surface was still CO covered. However, a new peak at 287.9 eV appeared in the C1*s* spectrum at the high binding energy side of the on-top CO peak. This peak was only observed during CO oxidation (i.e. when CO_2 formation was observed). The origin of such a feature is not completely known, though it may belong to a reaction intermediate [48]. Although it is similar to the CO vibrational fine structure, the intensity is much larger than what has been reported.

The sample temperature was maintained at 150 ℃ during the entire CO oxidation experiment. Figure A. 2 shows the reaction data, i.e., the partial pressures of CO, O_2, and CO_2 gases during CO oxidation. By controlling the CO pressure, we can switch the reaction conditions from a CO rich to an O_2 rich environment and vice versa. In each region, XPS data (Figure A. 3) was collected after the pressure stabilized. First, we introduced 180 mTorr O_2 into the high pressure cell (Region A), creating a Pt surface that is covered with chemisorbed atomic oxygen [54]. Only one O1*s* peak at 529.7 eV, belonging to chemisorbed oxygen, is observed [55]. A corresponding high BE shoulder also appears in

the Pt4*f* spectrum [51, 52].

At t = 4200 s (start of Region B), CO was introduced at 230 mTorr. At the same time, the O_2 partial pressure dropped to 140 mTorr. This drop is partly due to the consumption of O_2 by the reaction, but the major reason is the gas delivery system, i.e., a decrease of the pressure difference between the gas manifold and the high pressure cell. As soon as CO is introduced, a sharp increase in CO_2 production is observed in Region B of Figure A. 2, which is then followed by a decrease to a steady state value of ~14 mTorr. The sudden increase in CO_2 production results from reaction between CO gas and chemisorbed oxygen on the Pt surface. However, this chemisorbed oxygen is not stable under these reaction conditions and disappears immediately. Due to the limited flow rate of the chamber, the CO_2 decreases slowly to the steady state value, 14 mTorr. O1*s* spectra taken after the pressure stabilized clearly show that the chemisorbed oxygen on the surface is completely removed. The main peak at 532.7 eV in the O1*s* spectrum results from on-top site CO molecules on the Pt surface. This is also supported by the corresponding C1*s* peak and Pt4*f* spectrum (Figure A. 3a, c Spectrum B). Furthermore, the new peak observed in Figure A. 1a (Spectrum D) at 287.8±0.1 eV is present in the C1*s* spectrum. The rapid increase and decay of the CO_2 signal in the early stage of Region B demonstrates that the oxygen covered Pt(110) surface has a higher reaction rate than that of the CO covered surface, but this surface is not stable under CO rich conditions.

In Region C, we reduce the CO pressure to achieve an O_2 rich condition. The CO_2 production starts to increase as the CO pressure decreases. The CO_2 production reaches a maximum when the CO pressure reaches a minimum at 14 mTorr. The O1*s*, C1*s* and Pt4*f* core level spectra taken in this region are almost identical to those of Region B, except for a slight decrease of the high BE shoulder of the Pt4*f* peaks. This shows that the Pt surface is still CO covered, but with lower CO coverage. There is no chemisorbed oxygen or oxide formation on the Pt surface. Furthermore, the CO_2 pressure decreases from 50 to 36 mTorr as the CO pressure increases from 14 to 28 mTorr in Region C, a negative order in CO. This result is consistent with the classical L-H mechanism. Because of the asymmetric adsorption of CO and O_2 on the Pt surface, a state with low (high) CO coverage exhibits a high (low) rate of CO_2 production [53]. This high reaction rate region is different from the high reaction rate region observed in Ref. [47], where the Mars-Van Krevelen mechanism

is proposed. In their experiment (performed under higher pressures and higher O_2/CO ratio), the CO_2 pressure increases as the pressure of CO increases in the high reaction rate region.

To complete this study, we then increase the CO pressure back to 200 mTorr to reproduce a CO rich condition similar to Region B. Both reaction data in Figure A. 2 (Region D) and XPS data in Figure A. 3 shows identical results as those obtained in Region B. The production of CO_2 decreases again when the CO pressure increases, which is consistent with the L-H mechanism.

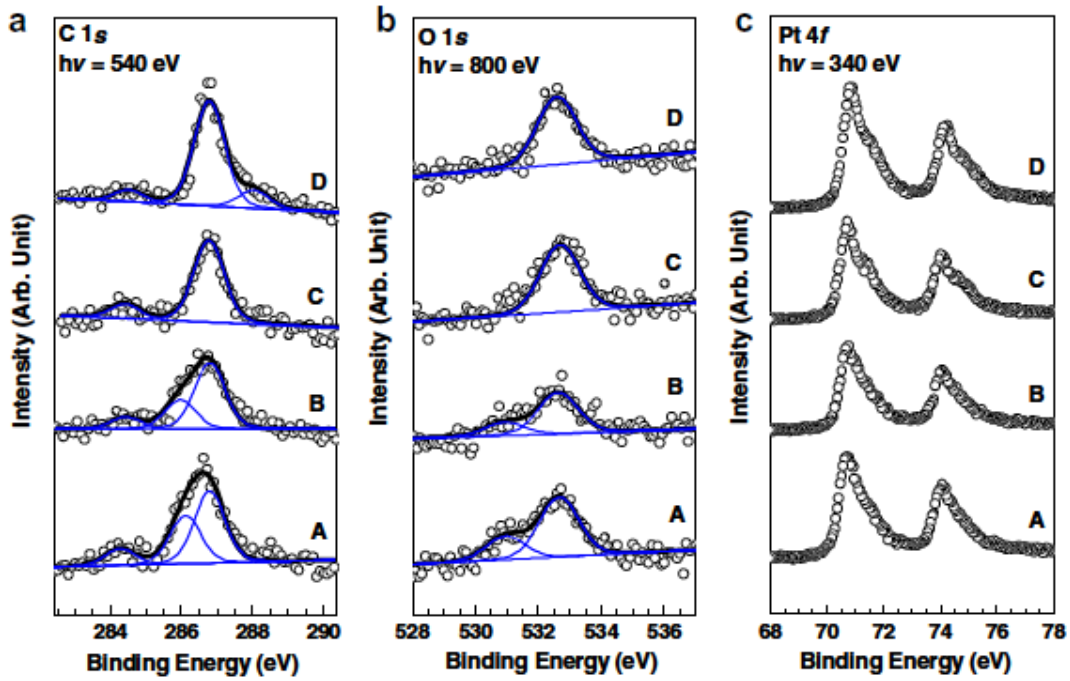

Figure A. 1 The C1*s*, O1*s* and Pt4*f* core level spectra of the Pt(110) surface under different conditions. A: 200 mTorr CO at room temperature; B: 200 mTorr CO+200 mTorr O_2 at room temperature; C: 200 mTorr CO+200 mTorr O_2 at 100 ℃; D: 200 mTorr CO+200 mTorr O_2 at 150 ℃.

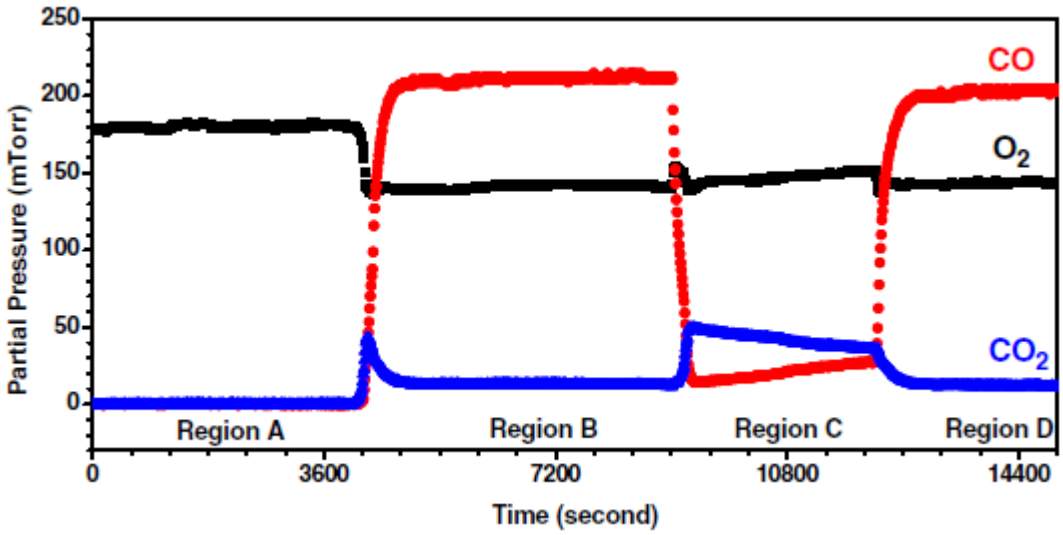

Figure A. 2 Partial pressures of CO, O_2, and CO_2 at a constant temperature of 150 ℃. We controlled the CO pressure to switch the reaction from a CO rich to oxygen rich environment and vise versa. Region A: 180 mTorr O_2; Region B: 140 mTorr O_2+230 mTorr CO; Region C: 150 mTorr O_2+14 mTorr -28 mTorr CO; Region D: 140 mTorr O_2+200 mTorr CO. These regions correspond to XPS spectra in Figure A. 3.

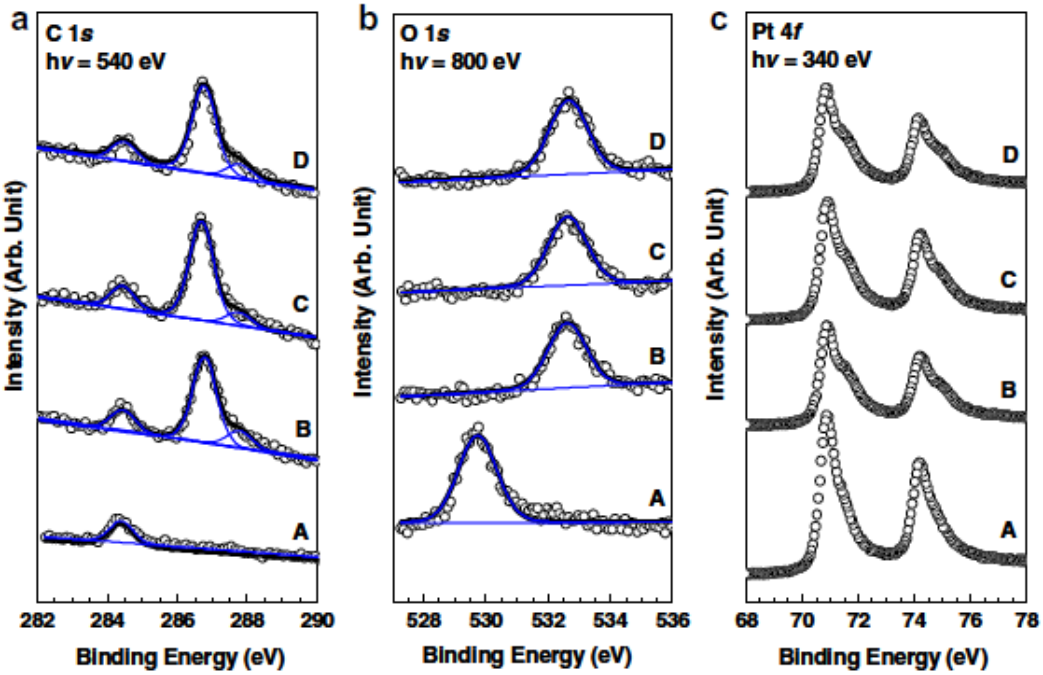

Figure A. 3 XPS spectra at each region in Figure A. 2 (A-D): (a) C1*s* spectra taken at 540 eV; (b) O1*s* spectra taken at 800 eV; (c) Pt4*f* taken at 340 eV.

A. 4 Conclusion

To summarize, we investigated the CO and O_2 co-adsorption and catalytic oxidation of CO on a Pt(110) surface using APXPS at various temperatures and pressures. We found that the CO molecules occupy both bridge and on-top sites at room temperature. As the temperature increases, the number of the bridge site CO molecules is reduced and completely removed above 100 ℃ and only CO molecules absorbed at on-top site remain. We also observe a reaction peak in the C1*s* spectra that is associated with CO oxidation. During CO oxidation, we monitor the surface chemical composition and surface reactivity under both O_2 rich and CO rich environments. No surface oxides were detected under either condition; the chemisorbed oxygen surface formed under 200 mTorr O_2 can lead to a high reaction rate, but it is not stable under the reaction conditions we investigated. The high reaction rate found in Region C (O_2 rich) can be explained by the Langmuir-Hinshelwood mechanism. We also want to emphasize that no direct comparison should be made between this study and that of Ref. [47] due to the difference in CO/O_2 ratio and total pressure. The surface chemical compositions may be different under those conditions.

References

[1] W. Hebenstreit, J. Redinger, Z. Horozova, M. Schmid, R. Podloucky, and P. Varga, Surface Science **424**, L321 (1999).

[2] S. Schintke, S. Messerli, M. Pivetta, F. Patthey, L. Libioulle, M. Stengel, A. De Vita, and W. D. Schneider, Physical Review Letters **87**, 276801/1 (2001).

[3] M. Katayama, K. Ueno, A. Koma, M. Kiguchi, and K. Saiki, Japanese Journal of Applied Physics **43**, L203 (2004).

[4] K. Glökler, M. Sokolowski, A. Soukopp, and E. Umbach, Physical Review B **54**, 7705 (1996).

[5] H. Guo and R. Souda, Journal of Applied Physics **92**, 6621 (2002).

[6] H. Guo, H. Kawanowa, and R. Souda, Applied Surface Science **158**, 159 (2000).

[7] M. Pivetta, F. Patthey, M. Stengel, A. Baldereschi, and W.-D. Schneider, Physical Review B **72**, 115404 (2005).

[8] I. Mauch, G. Kaindl, and A. Bauer, Surface Science **522**, 27 (2003).

[9] J. Repp, S. Folsch, G. Meyer, and K.-H. Rieder, Physical Review Letters **86**, 252 (2001).

[10] W. Hebenstreit, M. Schmid, J. Redinger, R. Podloucky, and P. Varga, Physical Review Letters **85**, 5376 (2000).

[11] R. Bennewitz, A. S. Foster, L. N. Kantorovich, M. Bammerlin, C. Loppacher, S. Schär, M. Guggisberg, E. Meyer, and A. L. Shluger, Physical Review B **62**, 2074 (2000).

[12] R. Bennewitz, V. Barwich, M. Bammerlin, C. Loppacher, M. Guggisberg, A. Baratoff, E. Meyer, and H. J. Gtherodt, Surface Science **438**, 289 (1999).

[13] V. Zielasek, T. Hildebrandt, and M. Henzler, Physical Review B **69**, 205313 (2004).

[14] C. Schwennicke, J. Schimmelpfennig, and H. Pfn, Surface Science **293**, 57 (1993).

[15] S. Folsch, U. Barjenbruch, and M. Henzler, Thin Solid Films **172**, 123 (1989).

[16] G. K. Wertheim, J. E. Rowe, D. N. E. Buchanan, and P. H. Citrin, Physical Review B **51**, 13675 (1995).

[17] T.-C. Chiang, Critical Reviews in Solid State and Materials Sciences **14**, 269 (1988).

[18] H. N. Waltenburg and J. T. Yates Jr, Chemical Reviews **95**, 1589 (1995).

[19] I. Lyubinetsky, Z. Dohnahek, W. J. Choyke, and J. T. Yates, Physical Review B **58**, 7950 (1998).

[20] G. Ketteler, D. F. Ogletree, H. Bluhm, H. Liu, E. L. D. Hebenstreit, and M. Salmeron, Journal of the American Chemical Society **127**, 18269 (2005).

[21] D. S. Lin, J. L. Wu, S. Y. Pan, and T. C. Chiang, Physical Review Letters **90**, 046102 (2003).

[22] E. Landemark, C. J. Karlsson, Y. C. Chao, and R. I. G. Uhrberg, Physical Review

Letters **69**, 1588 (1992).

[23] D. A. Lapiano-Smith, E. A. Eklund, F. J. Himpsel, and L. J. Terminello, Applied Physics Letters **59**, 2174 (1991).

[24] J. J. Boland, Advanced Physics **42**, 129 (1993).

[25] S. F. Tsay and D. S. Lin, Surface Science **603**, 2102 (2009).

[26] S. F. Tsay, unpublished.

[27] S. Sinharoy, Thin Solid Films **187**, 231 (1990).

[28] R. F. C. Farrow, P. W. Sullivan, G. M. Williams, G. R. Jones, and D. C. Cameron, Journal of Vacuum Science and Technology **19**, 415 (1981).

[29] J. J. Kolodziej, B. Such, P. Czuba, F. Krok, P. Piatkowski, and M. Szymonski, Surface Science **506**, 12 (2002).

[30] S. F. Tsay, J. Y. Chung, M. F. Hsieh, S. S. Ferng, C. T. Lou, and D. S. Lin, Surface Science **603**, 419 (2009).

[31] F. J. Himpsel, F. R. McFeely, J. F. Morar, A. Taleb-Ibrahimi, and J. A. Yarmoff, Photoemission and Adsorption Spectroscopy of Solids and Interfaces with Synchrotron Radiation. In: G. Scoles, Editor, Proceedings of the International School of Physics ”Enrico Fermi” Course CVIII, North-Holland, New York,1991.

[32] P. Stoltze and J. K. Norskov, Physical Review Letters **55**, 2502 (1985).

[33] R. Souda, W. Hayami, T. Aizawa, S. Otani, and Y. Ishizawa, Physical Review B **47**, 4092 (1993).

[34] P. Bogusławski, Q. M. Zhang, Z. Zhang, and J. Bernholc, Phys. Rev. Lett. **72**, 3694 (1994).

[35] T. Hashizume, K. Motai, H. Lu, and T. Sakurai, Applied Surface Science **67**, 261 (1993).

[36] A. A. Saranin, et al., Physical Review B **58**, 4972 (1998).

[37] S. Folsch, A. Helms, S. Zöphel, J. Repp, G. Meyer, and K. H. Rieder, Physical Review Letters **84**, 123 (2000).

[38] Y. Liu, A. J. Komrowski, P. R. Taylor, and A. C. Kummel, J. Chem. Phys. **109**, 2467 (1998).

[39] Y. Liu, D. P. Masson, and A. C. Kummel, Science **276**, 1681 (1997).

[40] M. F. Hsieh, J. Y. Cheng, J. C. Yang, D. S. Lin, K. Morgenstern, and W. W. Pai, Physical Review B **81**, 9.

[41] G. Ertl, Surface Science **299-300**, 742 (1994).

[42] P. Stoltze and J. K. Norskov, Physical Review Letters **55**, 2502 (1985).

[43] D. F. Ogletree, H. Bluhm, G. Lebedev, C. S. Fadley, Z. Hussain, and M. Salmeron, Review of Scientific Instruments **73**, 3872 (2002).

[44] G. Ketteler, D. F. Ogletree, H. Bluhm, H. Liu, E. L. D. Hebenstreit, and M. Salmeron, Journal of the American Chemical Society **127**, 18269 (2005).

[45] M. Salmeron and R. Schloegl, Surface Science Reports **63**, 169 (2008).

[46] L. Österlund, P. B. Rasmussen, P. Thostrup, E. Lægsgaard, I. Stensgaard, and F. Besenbacher, Physical Review Letters **86**, 460 (2001).

[47] B. L. M. Hendriksen and J. W. M. Frenken, Physical Review Letters **89**, 046101 (2002).

[48] M. D. Ackermann, et al., Physical Review Letters **95**, 255505 (2005).

[49] X. Su, P. S. Cremer, Y. R. Shen, and G. A. Somorjai, Physical Review Letters **77**, 3858 (1996).

[50] C. T. Campbell, G. Ertl, H. Kuipers, and J. Segner, The Journal of Chemical Physics **73**, 5862 (1980).

[51] J. G. Wang, et al., Physical Review Letters **95**, 256102 (2005).

[52] O. Björneholm, A. Nilsson, H. Tillborg, P. Bennich, A. Sandell, B. Hernnäs, C. Puglia, and N. Mårtensson, Surface Science **315**, L983 (1994).

[53] K. Krischer, M. Eiswirth, and G. Ertl, The Journal of Chemical Physics **96**, 9161 (1992).

[54] W. X. Li, L. Österlund, E. K. Vestergaard, R. T. Vang, J. Matthiesen, T. M. Pedersen, E. Lægsgaard, B. Hammer, and F. Besenbacher, Physical Review Letters **93**, 146104 (2004).

[55] N. Freyer, M. Kiskinova, G. Pirug, and H. P. Bonzel, Surface Science **166**, 206 (1986).

Curriculum vitae

鐘　仁　陽

Jen-Yang Chung

terry06190619@yahoo.com.tw

■ NATIONALITY

- Taiwan (R.O.C.)

■ PERSONAL DETAILS

- Date of Birth: 19 June 1982.

■ SKILLS

- Ultra-High-Vacuum Scanning Tunneling Microscopy (UHV- STM)
- Ultra-High-Vacuum Atomic Force Microscopy (AFM)
- X-ray Photoelectron Spectroscopy (XPS)

■ EXPERIENCE

- Research in surface science and interested in adsorbates/semiconductor system.
- Study synchrotron radiation research at National Synchrotron Radiation Research Center (SRRC).
- Semiconductor processing technology at National Nano Device laboratories (NDL).
- Operate UHV-AFM and UHV-STM
- Exchange student at Advanced Light Source of Lawrence Berkeley National Laboratory, USA (2007/09~2008/08).

■ EDUCATION

Tamkang University (TKU) Taipei City
- undergraduate degree in department of physics
- 2000~2004

National Chiao Tung University (NCTU) Hsinchu City
- Ph. D. degree in institute of physics
- 2004~2010

■ PUBLICATIONS LIST

[1] J. Y. Chung, F. Aksoy, M. E. Grass, H. Kondoh, P. Ross, Z. Liu, and B. S. Mun, Surf. Sci. **603**, L35 (2009).

[2] J. Y. Chung, W. H. Wang, H. D. Li, C. T. Lou, and D. S. Lin, submitted (2009).

[3] S. F. Tsay, J. Y. Chung, M. F. Hsieh, S. S. Ferng, C. T. Lou, and D. S. Lin, Surf. Sci. **603**, 419 (2009).

[4] C. T. Lou, H. D. Li, J. Y. Chung, D. S. Lin, and T. C. Chiang, Phys. Rev. B **80**, 5 (2009).

[5] F. Tao, M. E. Grass, Y. W. Zhang, D. R. Butcher, J. R. Renzas, Z. Liu, J. Y. Chung, B. S. Mun, M. Salmeron, and G. A. Somorjai, Science **322**, 932 (2008).

[6] M. F. Hsieh, J. Y. Chung, D. S. Lin, and S. F. Tsay, J. Chem. Phys. **127**, 6 (2007).

[7] K. M. Yang, J. Y. Chung, M. F. Hsieh, and D. S. Lin, Jpn. J. Appl. Phys. Part 1 - Regul. Pap. Brief Commun. Rev. Pap. **46**, 4395 (2007).

[8] K. M. Yang, J. Y. Chung, M. F. Hsieh, S. S. Ferng, D. S. Lin, and T. C. Chiang, Phys. Rev. B **74**, 4 (2006).